Synaptic Elasticity

Ju Yang

Submitted in partial fulfillment of the
requirements for the degree of
Doctor of Philosophy
in the Graduate School of Arts and Sciences

COLUMBIA UNIVERSITY

2018

Abstract

Synaptic Elasticity

Ju Yang

Synapses play a critical role in neural circuits, and their highly specialized structures and biochemical characteristics have been widely studied in learning and memory. Along with their role in signal transmission, synapses also serve as adhesion structures, yet their mechanical characteristics have not received much attention. Given the important role of mechanics in cell adhesion, mechanical studies of synapses could offer insights into synaptic development, maintenance, and function. Here, I investigated synaptic elasticity in cultured rat hippocampal neurons and suggest that mechanical elasticity may be related to synaptic plasticity. I used torsional harmonic atomic force microscopy (TH-AFM) to measure the nanomechanical properties of functional mature excitatory synapses, whose identity and activity was verified by fluorescence microscopy. I combined TH-AFM with transmission electron microscopy and found that high stiffness of synapses originated from postsynaptic spines, not presynaptic boutons. I observed that spines at functional mature excitatory synapses were on average 10 times stiffer than dendritic shafts and that the distribution of spine stiffness exhibited a lognormal-like pattern. Importantly, I found that spine stiffness was correlated with spine size, and it is well established that spine size is correlated with synaptic strength. Based on the stiffness measurements and theoretical modelling of cell adhesion stability, I suggest that stiffness not only helps maintain spine morphology in the presence of synapse adhesion, but also helps stabilize synaptic adhesion. I propose a mechanical synaptic plasticity model. According to this model, mechanical strength leads to functional strength, which could provide a potential causal link between structural plasticity and functional plasticity of synapses.

Table of contents

List of charts, graphs, illustrations

Acknowledgements

First and foremost, utmost thanks to my academic advisor and mentor, Professor Ozgur Sahin. You are a wonderful advisor in scientific research and a superb mentor in professional and personal development. Your curiosity and enthusiasm in fundamental neuroscience and biophysics problems, positive attitude and patience in mentoring, and careful attention and advice in advancing students' career, have not only motivated me to constantly challenge myself through my doctoral research, but also helped me to build confidence and competency for my post-doctoral career. I am deeply grateful to have you as my advisor and learn from our extensive and invigorating discussions about science and beyond.

To members of my thesis committee, Professor Rafael Yuste, Professor Jian Yang, Professor Roger Lefort, and Professor Ben O'Shaughnessy for sitting through countless hours of committee meetings and providing valuable comments, ideas, and insights to improve my project. To my collaborators, Professor Rafael Yuste and Professor Roger Lefort for the great discussion on dendritic spines, neurodegenerative diseases, and cell imaging experiments.

To my colleague Sahinians in the lab. You all create such a supportive and friendly learning environment, ask insightful questions, and provide valuable suggestions on both my research and my graduate life. To Dr. Duckhoe Kim, Dr. Nicola Mandriota, and Professor Xi Chen for patiently guiding me through the very first step in the lab and bearing with me all my mistakes and endless questions. To John A. Jones Molina and Steven Glenn Harrellson for the great discussion about synapse and physics modeling. To Dr. Ahmet-Hamdi Cavusoglu, Dr. Michael DeLay, Dr. Suleyman Ucuncuoglu, Dr. Onur Cakmak, Dr. Youngkyu Kim, Dr. Krishna Jayant, Zhenghan Gao, and Juan Manuel de Flores Quijano for the generous help on my thesis writing and defense preparation. Also to my collaborators at NYU Microscopy Core, Kristen Dancel-Manning, Chris Petzold, and Alice

Liang, for the assistance in electron microscopy, and Hardik Patel for neuronal cultures.

To the administrative office staff in the Department of Biological Sciences, Sarah Kim Fein, Jayalakshmi Santosh, and Joshua Sakolsky, and Ellie Siddens for making sure my PhD training went on smoothly and rewardingly, and always being there to help me solve sometimes frustrating administrative issues.

To my family. I would not make it this far without your unconditional support. To my father, Xianwei Yang, thank you for encouraging me to explore the world and not to be intimidated by mistakes and failures. It is this very grit and toughness that dragged me through those difficult downtimes in research. To my mother, Guihua Wang, thank you for giving me the ultimate trust and confidence to choose the road I desired and not to be limited by the so-called traditional life path. Your wisdom and attitude towards life has always been the original motivation of all my achievements.

To my friends who made my life in New York full of joy and excitement, and largely broadened my horizon. To Dr. Ming Sun, Yaqiong Chen, Chang Liu, Chen Chen, Rongnan Chen, and Mimo He for the genuine encouragement and great conversations during the peaks and valleys in my graduate life. Also, I'd like to thank Hebe Xu, Igor Elbert, Dr. Rouzbeh Gerami, Dr. Raymond Ko, Dr. Ju Tian, Xing Xing, Dr. Haiyuan Cao, Dr. Jie Zhou, and Cheng Liu, for your tremendous guidance and help in my career exploration and development.

Finally, to my boyfriend Paul Zaldy Tapo. I was lucky to meet you among millions of people in New York three years ago when I was struggling to find out who I could be. You have always encouraged me to be myself and live in the moment, and motivated me to stick to my goals and shrug off failures. You are my most cheerful advocate when I dream big, my best stress reliever when I am frustrated, and a humorous critic when nonsense happens. I could not have completed this without your love and support.

Dedication

To my family.

Chapter 1 Introduction

In our brain, there are 100 billion (10^{11}) neurons, similar to the number of estimated stars in the Milky Way. Each neuron communicates with many other neurons through highly specialized cellular structures called synapses, forming 100 trillion (10^{14}) synapses overall. Synapses not only transmit signals between neurons, but also change their structure and function upon stimulation, referred to as synaptic plasticity, which is believed to play a central role in learning and memory. Along with their role in signal transmission, synapses also serve as adhesion structures, yet their mechanical characteristics have not received much attention.

In this Chapter, I will introduce the mechanics of synapses and provide an overview of this dissertation.

About 130 years ago, a famous Spanish neuroscientist Santiago Ramón y Cajal first demonstrated that the nervous system was not continuous as a whole, but was made up of discrete individual nerve cells, named as "neurons" later by H. Waldeyer-Hartz. This theory, known as the neuron doctrine, is now widely considered as the foundation of modern neuroscience (Figure 1-1 A). Neurons communicate with each other via a microscopic gap named as the "synapse" by Charles Sherrington (Finger, 2000).

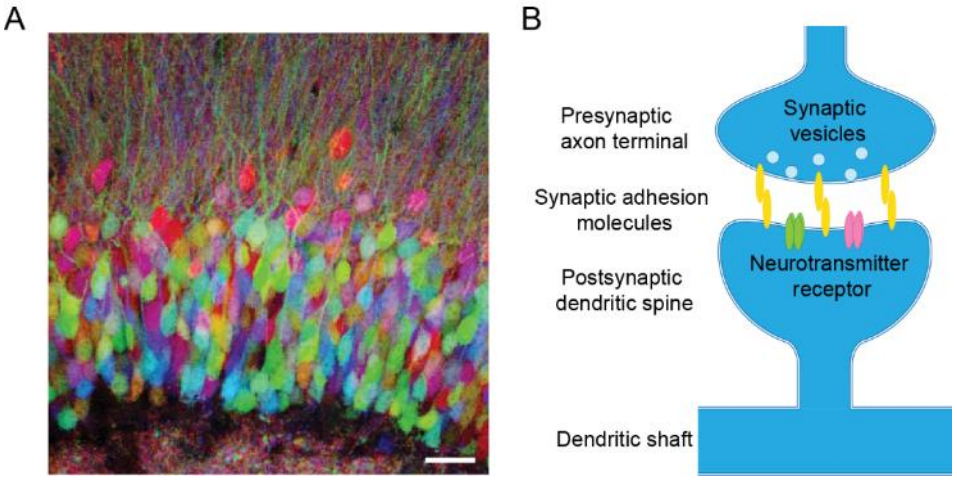

Figure 1-1 Neurons communicate through synapses.
(A) Individual neurons in the mice hippocampus revealed by *Brainbow* with stochastic expression of multiple fluorescent proteins. Scale bar: 20 μm. Reprinted and adapted with permission from (Livet et al., 2007), © 2007 Nature Publishing Group. (B) A schematic diagram of a typical synapse with a presynaptic axon terminal and a postsynaptic dendritic spine connected by synaptic adhesion molecules (yellow). The presynaptic terminal releases synaptic vesicles (light blue) containing neurotransmitters, which bind to receptors (green and magenta) on the postsynaptic membrane.

Modern neuroscience has shown that synapses are highly specialized intercellular junctions comprised of pre- and postsynaptic structures that are tightly connected by synaptic adhesion molecules (Figure 1-1 B). Synapses play a central role in learning and memory through the "Hebbian theory": neurons that fire together wire together (Hebb, 1949). The basic mechanism is called synaptic plasticity in which synapses are strengthened from stimulated synaptic transmission and activity. Because synaptic plasticity is critical for learning and memory, biochemical and morphological characteristics of synapses and electrophysiological properties of neurons have been widely investigated.

Along with their role in biochemical signal transmission, synapses also serve as adhesion structures, yet their mechanical characteristics have not received much attention.

Synapses are indeed mechanically interesting structures (Figure 1-2) (Tyler, 2012). Mechanics could regulate neuronal development and function. Substrate stiffness modulates neuronal growth and network activity (Q. Y. Zhang et al., 2014), likely through integrin-mediated cell adhesion (Chavis & Westbrook, 2001). The specification and function of axons may require cyto-mechanical signals either from interaction with a target postsynaptic structure or an artificial towing force. Pioneering studies by Lamoureux et al. showed the induction and elongation of axons by applying tension to neurites of hippocampal neurons in the early stage using a glass needle (Lamoureux, Ruthel, Buxbaum, & Heidemann, 2002). Studies by Siechen et al. (Siechen, Yang, Chiba, & Saif, 2009) and Ahmed et al. (Ahmed et al., 2012) using embryonic *Drosophila* nervous system showed that axons are under rest tension at nano-Newton scale and that vesicle clustering at the presynaptic terminal depends on mechanical tension within axons. Action potential is accompanied by mechanical changes in axons such as volume change (Chereau, Saraceno, Angibaud, Cattaert, & Nagerl, 2017; El Hady & Machta, 2015; B. C. Hill, Schubert, Nokes, & Michelson, 1977; D. K. Hill, 1950) and shortening of axons (Tasaki & Byrne, 1982). In postsynaptic dendritic spines, three-dimensional actin networks are present and undergo fast dynamic changes (Hotulainen & Hoogenraad, 2010; Korobova & Svitkina, 2010; Nagerl, Willig, Hein, Hell, & Bonhoeffer, 2008), referred to as "spine twitching" by Francis Crick (Crick, 1982). Cross-linked actin networks exhibit unique viscoelasticity and stiffen with increased cross-linking density and tension (Gardel et al., 2004). Synapses exert accurate regulation on actin dynamics through actin binding proteins such as Arp2/3 (Hotulainen & Hoogenraad, 2010) to maintain their plasticity and stability. Several actin binding proteins are mechanosensitive, such as vinculin and talin (Jiang, Giannone, Critchley, Fukumoto, & Sheetz, 2003; Lee, Kamm, & Mofrad, 2007), whose binding affinity and structures can be affected by mechanical load. In addition, the

emerging role of mechanosensitive ion channels in mammalian cells including neurons (Arnadottir & Chalfie, 2010; Ranade et al., 2014) raises the possibility of regulating neuronal activity and plasticity through mechanical force.

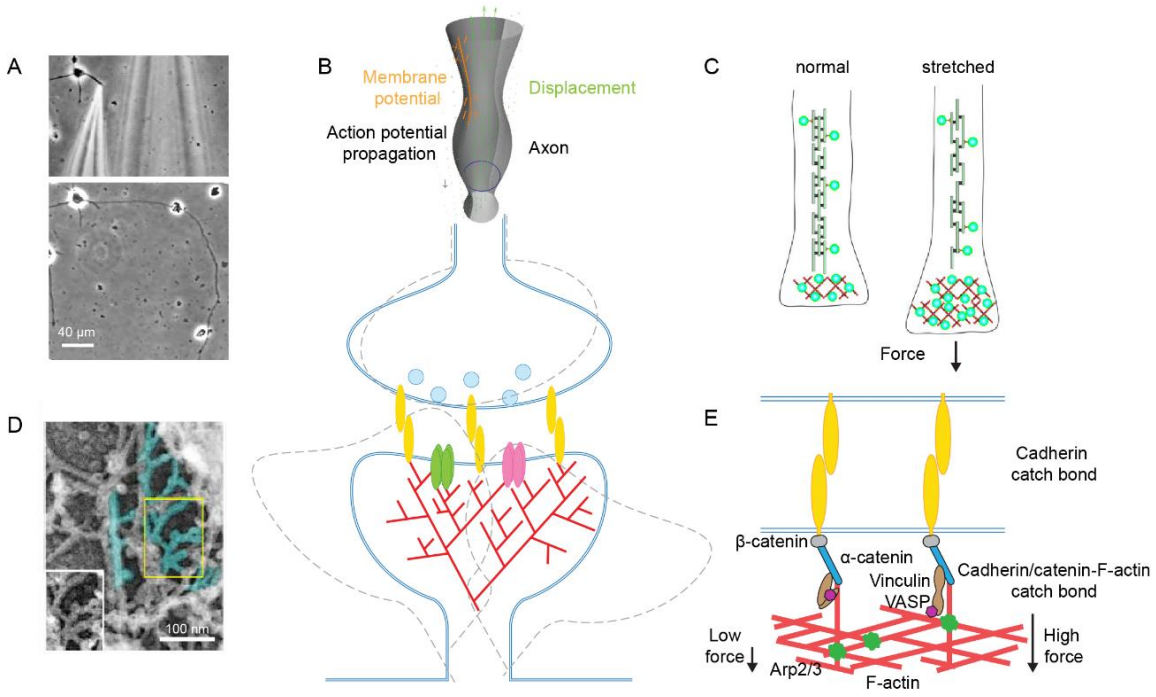

Figure 1-2 Synapses are mechanically interesting structures.
A schematic diagram of a synapse with pre- and postsynaptic structures connected by synaptic adhesion molecules (yellow) is shown in the center. (A) A neurite towed by a glass needle (top) developed into a long axon and continued elongating after needle removal (bottom) in DIV 1-2 neurons. (B) Action potential is accompanied by an electromechanical pulse travelling along the axon and a membrane displacement. Membrane (orange + and -) is depolarized as the action potential passes. This leads to changes in the electrostatic forces acting on the membrane (grey tube), resulting in a membrane displacement (green). (C) An axon at its normal resting state (left) or being stretched under force (right). Microtubules (green) extend along the axon. Vesicles (light green) are transported long the microtubules and some accumulate in the actin scaffolding (red) at the presynaptic termal. Force leads to increased vesicle clustering at the presynaptic termal due to tension induced actin polymerization creating more vesicle binding sites. (D) Branched actin filaments (cyan) in a spine head. The inset shows the nonpseudocolored region outlined by the yellow box. The dynamic changes of actin networks can drive changes in the spine structure such as spine twitching (indicated by the grey dash lines in the center diagram). (E) Mechanosensitivity at cell adhesion. On the extracellular side, cadherin (yellow) dimers form catch bonds which are strengthened in the presence of high force. On the intracellular side, cadherin interacts with F-actin (red) through α-catenin (blue) and β-catenin (grey). The interaction between cadherin/catenin and F-actin is tension sensitive and exhibits catch bond features. Under high force, vinculin (brown) is extended, recruiting actin-modulator VASP (magenta) and regulating actin polymerization. In addition, cadherin also helps recruit Arp2/3 (green) and enhance actin cross-linking. Images are reprinted and adapted with permission from: A, (Lamoureux et al., 2002), © 2002 Lamoureux et al.; B, (El Hady & Machta, 2015), © 2015 El Hady et al.; C, (Ahmed et al., 2012), © 2012 Biomedical Engineering Society; D, (Korobova & Svitkina, 2010), © 2010 Korobova et al.; E, (Han & de Rooij, 2017), © 2017 Macmillan Publishers Limited.

Pre- and postsynaptic compartments are connected physically by synaptic adhesion molecules, and are structurally and functionally coupled with each other (Okabe, Miwa, & Okado, 2001; Umeda, Ebihara, & Okabe, 2005). It is well accepted that mechanics plays an important role in cell adhesion. One type of well-characterized adhesion structures is focal adhesion between cells and extracellular matrix mediated by integrin (Geiger, Bershadsky, Pankov, & Yamada, 2001). Integrin lacks enzymatic activity, and it is now well known that it can trigger downstream signaling cascades via mechanosensation (Geiger, Spatz, & Bershadsky, 2009). At cell-cell interface such as synapses, the classical cadherin family plays an important role (Gumbiner, 2005). Cadherin interacts with actin networks on the intracellular side, recruiting actin binding proteins in a mechanosensitive manner similar to integrin (Maitre & Heisenberg, 2013). Cadherin-catenin complex binds to F-actin in a tension-sensitive process and forms catch bonds (Buckley et al., 2014). Force could induce conformational change of α-catenin and lead to the binding of vinculin to α-catenin through unmasking of the vinculin binding region (Yonemura, Wada, Watanabe, Nagafuchi, & Shibata, 2010). On the extracellular side, cadherin dimers can form catch bonds, which strengthen dimer interaction in the presence of mechanical force and further stabilize cell-cell adhesion (Manibog, Li, Rakshit, & Sivasankar, 2014; Rakshit, Zhang, Manibog, Shafraz, & Sivasankar, 2012). Therefore, mechanics may regulate synaptic adhesion via mechanosensation.

Another aspect where mechanics could potentially be relevant comes from the unique morphological specialization of synapses, in particular the morphology of dendritic spines (*hereafter referred to as spines*). Spines were first described by Santiago Ramón y Cajal, yet it still remains unclear what they do. A spine consists of an enlarged head (1-2 μm in diameter) and is connected by a thin neck (200 nm in diameter, and 0.5 to several μm in length) to the dendritic shaft (Figure 1-1 B). There are many proposals explaining the potential functions of spines (Rafael Yuste, 2010). A well-accepted explanation is that spines are essential for biochemical compartmentalization (Yasuda et al., 2006) and

electrical compartmentalization (Tsay & Yuste, 2004), creating input-specific plasticity and specification of synapses (Hebb, 1949). While spine morphology is functionally critical, generating and maintaining such a highly curved subcellular structure is by nature thermodynamically disfavored. Mechanical features such as membrane tension (Diz-Munoz, Fletcher, & Weiner, 2013; Gauthier, Masters, & Sheetz, 2012) and cell stiffness (Stroka & Aranda-Espinoza, 2011; Tseng et al., 2005) have been shown to help organize specialized cell morphology.

In order to understand how mechanics may play a role in synaptic structure and function, it is important to first characterize and quantify the baseline mechanical properties of synapses, and understand their features. Several experimental approaches have been developed for the study of cell mechanics (Diz-Munoz et al., 2013), including compression of cells with two plates and micropipette aspiration (Cole, 1932; Hochmuth, Mohandas, & Blackshear, 1973), optical tweezers and magnetic tweezers (H. Zhang & Liu, 2008), and atomic force microscopy (Spedden, White, Naumova, Kaplan, & Staii, 2012).

Here, I combined atomic force microscopy (AFM), fluorescence microscopy, and transmission electron microscopy (TEM) to characterize synaptic elasticity. First introduced in 1986 (Binnig, Quate, & Gerber, 1986), AFM has been widely used in material engineering, physics, and nanotechnology to acquire nanoscale topographical images and probe surface elasticity by measuring stiffness. AFM has unique capabilities to provide high resolution topographical images of live cells under physiologically-relevant conditions (Shibata, Uchihashi, Ando, & Yasuda, 2015). However, the application of AFM in neuroscience is still in its infancy (Tyler, 2012). To my knowledge, so far there is only one study related to the mechanical properties of synapses (Smith, Roy, De Koninck, Grutter, & De Koninck, 2007). Smith et al. studied the viscoelasticity of visually-identified spine-like structures using force-volume and indentation-modulation AFM, and found that the stiffness of spine-like structures observed in close proximity to axon-like structures was on average 2 times that of the

dendritic shafts. The authors suggested that mechanics may have a role in spine remodeling, protein trafficking, and structural stability. However, without the aid of additional methods, AFM lacks the capacity to identify synaptic markers, monitor synaptic activity, and visualize intracellular structures such as synaptic vesicles. Compounded with the low throughput of conventional force-volume AFM, these limitations hinder detailed assessment of synaptic mechanics, making it difficult to gain mechanistic insights into the role of mechanics in synaptic function.

In this work, I used torsional harmonic AFM (TH-AFM), which offers high-throughput stiffness mapping of compliant materials (Dong, Husale, & Sahin, 2009; Sahin, Magonov, Su, Quate, & Solgaard, 2007). TH-AFM uses a specially designed T-shaped cantilever which allows a large number of synapses to be imaged and quantified in a short amount of time with small indentation. In Chapter 2, I will describe TH-AFM principles and its application in biological research. In Chapter 3, I measured the nanomechanical properties of live neurons with TH-AFM and observed stiff synapse-like structures.

In order to understand the biological processes related to high stiffness, I combined TH-AFM with fluorescence microscopy in Chapter 4 and with TEM in Chapter 5. Immunofluorescence staining of synaptic markers and functional imaging of activity dyes allow us to identify mature synapses and monitor synaptic activity, and TEM provides reliable assessment of synaptic ultrastructure at high resolution. Combination of AFM and fluorescence microscopy has been used to reveal the mechanical structures of cytoskeleton in cells (Chacko, Zanacchi, & Diaspro, 2013; Curry, Ghezali, Kaminski Schierle, Rouach, & Kaminski, 2017), and combination of TEM and fluorescence microscopy has been used to study the ultrastructure of cellular components such as synaptic vesicles (Darcy, Staras, Collinson, & Goda, 2006). To my knowledge, no correlative AFM stiffness mapping and TEM imaging in neurons has been reported. The combination of multiple independent imaging methods allows us to assess mechanical characteristics of synapses in detail and correlate them with synaptic

structure and synaptic activity. I measured the elastic modulus of hundreds of live mature excitatory synapses whose identity and activity was confirmed by fluorescence microscopy. Correlative TH-AFM/TEM analysis showed that high stiffness originated from postsynaptic spines, but not presynaptic boutons.

In Chapter 6, I performed detailed data analysis and reported that spines were on average 10 times stiffer than dendritic shafts. Observations of such high stiffness localized to a submicron structure indicate that stiffness of spines might have an important role in synaptic function. Interestingly, the distribution of spine stiffness exhibited the characteristics of a lognormal distribution that is also observed in synaptic strength measurements (Buzsaki & Mizuseki, 2014). Importantly, I found that spine stiffness was positively correlated with spine size, and it is well-established that spine size is correlated with synaptic strength (Matsuzaki et al., 2001). In addition, I observed that shaft synapses and immature filopodia did not display high stiffness.

To understand what could be the source of spine stiffness, in Chapter 7, I studied how spine stiffness was related to actin networks. Interestingly, although enriched with F-actin, these stiff spines were not affected by actin polymerization inhibitor Latrunculin A or Myosin II inhibitor Blebbistatin, suggesting that neither high level F-actin elongation nor actomyosin contractility contributes to high spine stiffness. Given the presence of densely branched actin networks in spine heads, spine stiffness may come from cross-linked actin architecture mediated by Arp2/3.

Based on the stiffness measurements and theoretical modelling of cell adhesion stability (Qian & Gao, 2010), I propose a mechanical synaptic plasticity model in Chapter 8. According to this model, mechanical strength leads to functional strength, which could provide a potential causal link between structural plasticity and functional plasticity of synapses.

In Chapter 9, I will draw conclusions from these results and discuss future research directions.

Chapter 2 TH-AFM: a tool to study cell mechanics

In a macroscopic world, we can easily tell the relative stiffness of different materials: diamond is stiff, rubber is soft, and gold is somewhere in between. How do we know this? The simplest way is to place our fingers on a surface and press it. In a microscopic world, if we want to "feel" the stiffness of tiny structures such as cells and synapses, human fingers are clearly out of the scale considering that cells are 10,000 times smaller than human fingers. Fortunately, the basic principles of physics remain the same. All we need is a nanoscale finger that can indent the material and accurately measure interaction forces and indentation distance.

In this Chapter, I will introduce atomic force microscopy (AFM) and its applications in biological samples. I will also discuss current challenges in cell mechanics imaging and introduce our approach.

2.1 AFM principles

Atomic force microscopy (AFM) belongs to a family of techniques called scanning probe microscopy (SPM). SPM in general uses a probe to scan the surface and measures the interaction between the tip and the sample at each interaction position. Prior to AFM, another type of SPM, scanning tunneling microscope (STM) was developed by Binnig and Rohrer in 1981, who later received the Nobel Prize in Physics for this invention. STM, however, can only be used on electrically conductive surfaces (Binnig, Rohrer, Gerber, & Weibel, 1982), limiting its application in other fields. In 1986, Binnig et al. developed AFM, which can be used on any surfaces regardless of their electrical conductivity (Binnig et al., 1986). Such versatility makes AFM a popular tool to profile surface topography and mechanics.

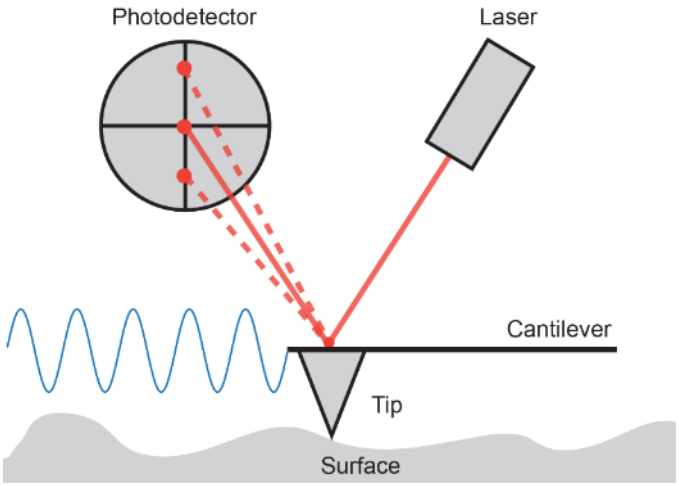

Figure 2-1 AFM principles.
The sharp AFM tip at the end of a cantilever interacts with the sample surface, causing the cantilever to deflect. The cantilever deflection is monitored by the position of a laser spot (solid and dashed red lines) on a photodetector, and is used to track surface topographical and mechanical features. In the contact-mode AFM, the tip stays in contact with the sample surface with a feedback circuit to keep the cantilever deflection constant. In the tapping-mode AFM, the cantilever is oscillated at its resonance frequency (blue sinusoidal curve) with a feedback circuit to keep the oscillation amplitude constant. The sample is mounted on a piezoelectric scanner which provides accurate three-dimensional positioning.

AFM measures ultra-small forces (picoNewton scale) between a sharp AFM tip (less than 100 nm in diameter) and a sample surface (Figure 2-1). The interaction force between the atoms at the end of the tip and the sample surface causes the cantilever deflection, which is monitored by a

photodetector that quantifies the position of a laser spot reflecting from the back side of the cantilever. The deflection signal is used to track surface topographical and mechanical features. The sample is mounted on a piezoelectric scanner which provides accurate three-dimensional positioning. AFM imaging generates very high force sensitivity as small as picoNewton and high spatial resolution at sub-nanometer scale (Bhushan, 2008).

AFM can be operated in either the contact mode or the tapping mode. In the contact-mode AFM, the sharp tip at the end of the cantilever is brought in contact with the sample surface and stays in contact with the surface during imaging. The surface contours are measured by a feedback signal required to keep the cantilever deflection constant (Binnig et al., 1986). In the tapping-mode AFM, also referred to as the dynamic-mode AFM, the cantilever is oscillated at its resonance frequency (shown as the sinusoidal curve in Figure 2-1) by a piezo. The oscillating tip slightly taps the surface at high frequency (kHz) with a feedback circuit to keep the oscillation amplitude constant (Barlow, 1991; Radmacher, Tillamnn, Fritz, & Gaub, 1992). The oscillation amplitude is kept large enough in cell imaging (50-100 nm) to prevent the tip from getting stuck on adhesive surfaces. The tapping-mode AFM have several advantages over the contact-mode AFM (Garcia & Herruzo, 2012). First, it minimizes the effect of friction and other lateral forces during scanning. Second, in the tapping mode, the tip only interacts with the sample surface for a very short period of time compared with the constant interaction in the contact mode, and thus very small forces can be applied to soft samples. Large sample deformation by the tapping force is also minimized. Third, other parameters such as amplitude, phase, and frequency, are also available from the cantilever oscillation in the tapping mode, and can be used to extract mechanical properties.

2.2 AFM applications in biological samples

The invention of AFM is a milestone in the history of nanotechnology and opens the doors to the nanoworld in material engineering, physics, chemistry, and biology (Gerber & Lang, 2006). In

particular, the possibility of operating AFM in buffer solution and at ambient temperature draws a lot of attention and interest in biological samples under physiologically-relevant conditions (Santos & Castanho, 2004). Shortly after AFM was invented, pioneering applications of AFM in biological samples (Figure 2-2) include cell membrane and proteins (Hoh, Lal, John, Revel, & Arnsdorf, 1991; Schabert, Henn, & Engel, 1995), DNA (Hansma et al., 1992), lipid bilayer (Zasadzinski, Viswanathan, Madsen, Garnaes, & Schwartz, 1994), cytoskeleton (Henderson, Haydon, & Sakaguchi, 1992), and live cells (Henderson et al., 1992; Hoh & Schoenenberger, 1994). Recent development of high speed AFM (Ando et al., 2001) provides new opportunities to monitor fast dynamic biological behaviors such as Myosin V walking on actin filament (Kodera, Yamamoto, Ishikawa, & Ando, 2010) and morphogenesis of filopodia in neurons (Shibata et al., 2015).

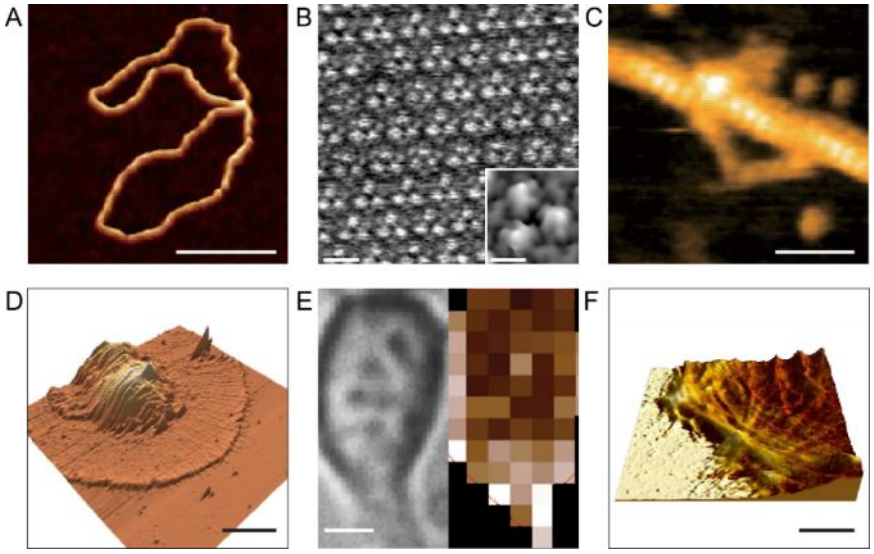

Figure 2-2 AFM applications in biological samples.
(A) Topographical image of DNA. (B) Topographical image of purple membrane. (C) Topographical image of Myosin V bound to adjacent actin filaments. (D) Three-dimensional reconstruction of the topography of live *Aplysia* growth cones. (E) Optical image and corresponding elasticity map of a live cortical neuron. (F) High resolution three-dimensional overlay of topography and elastic modulus of a live mouse fibroblast. Scale bar: A, 100 nm; B, 5 nm, 2 nm; C, 30 nm; D, 15 μm; E, 2 μm ; F, 5 μm. Images are reprinted and adapted with permission from: A, (Ido et al., 2013), © 2013 American Chemical Society; B, (Muller & Engel, 2007), © 2007 Nature Publishing Group; C, (Kodera et al., 2010), © 2010 Macmillan Publishers Limited; D, (Xiong, Lee, Suter, & Lee, 2009), © 2009 the Biophysical Socienty; E, (Spedden & Staii, 2013), © 2013 Spedden et al.; F, (Mandriota, 2016), © 2016 Mandriota.

In addition to topographical imaging, AFM has evolved into a multifunctional imaging toolkit (Muller & Dufrene, 2011). AFM force spectroscopy mode directly measures interaction forces

between the cantilever tip and the sample. The tip is usually functionalized with specific biomolecules or a living cell in order to study interactions between single molecules or between cells. Popular applications in this mode include single-molecule force spectroscopy (Dong & Sahin, 2011; Florin, Moy, & Gaub, 1994), molecular recognition mapping (Gad, Itoh, & Ikai, 1997; Hinterdorfer & Dufrene, 2006) , and single-cell force spectroscopy (Benoit, Gabriel, Gerisch, & Gaub, 2000; Helenius, Heisenberg, Gaub, & Muller, 2008). AFM force spectroscopy mode is also used to measure the mechanical properties of cells at nanometer resolution. Unlike other force spectroscopy applications, in cell mechanical imaging, the AFM tip is usually not specially functionalized. Instead, a cantilever with a large tip diameter or a microbead attached to the end (Lulevich, Zink, Chen, Liu, & Liu, 2006) is used in order to increase the contact area between the tip and the cell surface during indentation, preventing the tip from penetrating and damaging delicate cell surfaces. Therefore, the same cantilever can potentially be used on different types of samples without much modification. The spatial resolution of AFM force spectroscopy on cell surfaces is approximately 50-100 nm due to compliant surface nature of cells. Still, it is well below the resolution limit of conventional optical microscopy (200 nm).

Using AFM force spectroscopy, researchers have investigated cell mechanics in various living cells and reported interesting discoveries (Muller & Dufrene, 2011). First, force spectroscopy can be used to characterize cell stiffness and track dynamic changes of cells. Matzke et al. measured changes in the stiffness of the cortex of adherent cultured cells during M phase, from metaphase to cytokinesis, showing that cortical stiffening occurs before any furrow appears and stiffening increases as the furrow starts (Matzke, Jacobson, & Radmacher, 2001). Smith et al. probed the biomechanics in living neurons and reported the viscoelasticity and soft-glassy nature of spine-like structures (Smith et al., 2007). Spedden et al. characterized how stiffness of somata changes during neurite outgrowth in different types of neurons and showed the increase in local elastic modulus is primarily due to the formation of

microtubules (Spedden et al., 2012). Second, force spectroscopy can be used to study how cell stiffness responds to drugs and other intervention. Rotsch and Radmacher investigated drug-induced changes in elasticity of fibroblasts combining AFM height images, elasticity images, and fluorescence images (Rotsch & Radmacher, 2000). Third, cell mechanics provides potential applications in the study and detection of diseases. For example, Cross et al. measured cell stiffness of cancer cells obtained from patients and reported that metastatic cancer cells are substantially softer than the benign cells (Cross, Jin, Rao, & Gimzewski, 2007).

2.3 AFM in the study of cell mechanics

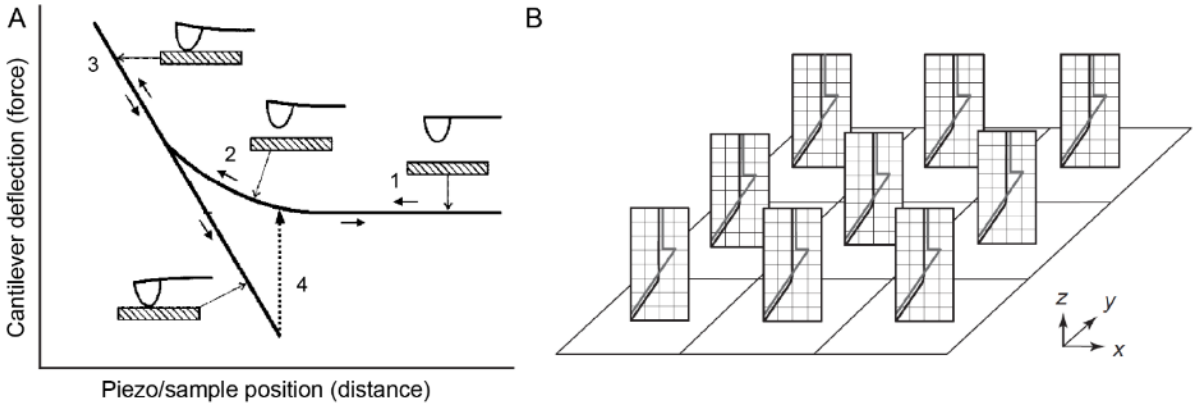

Figure 2-3 Force-distance curves and force-volume imaging with AFM.
(A) A single force distance (FD) curve records the interaction force on the tip as it approaches and retracts from the sample surface. Force on the tip is calculated from the cantilever deflection and the cantilever spring constant using Hooke's law. There are 4 regions of interest in a typical FD curve. In the beginning (1), the tip is far from the sample surface, and thus there is no interaction or cantilever deflection. As the tip approaches the surface (2), tip-sample interaction causes the cantilever to deflect. When the tip contacts and indents the surface, the cantilever continues to deflect until reaching the maximal deflection (3). Then the cantilever starts to retract. Owing to various tip-sample interactions, such as adhesive forces, the retraction curve can display hysteresis (4). At the end of the curve, the tip completely separates from the sample and the cantilever returns to zero deflection. (B) Force-volume imaging collects arrays of FD curves for each coordinate, which are used to map the mechanical features on the sample surface. Images are reprinted and adapted with permission from: A, (Butt, Cappella, & Kappl, 2005), © 2005 Elsevier; B, (Heinz & Hoh, 1999), © 1999 Elsevier Science.

Cell mechanical properties, such as Young's elastic modulus, are traditionally measured using AFM by approaching the tip to and retracting it from the sample surface, generating a single force-distance (FD) curve (Figure 2-3 A)(Butt et al., 2005). Force on the tip is calculated from the cantilever deflection and cantilever spring constant using Hooke's law. FD curves provide information about

sample height, indentation distance, and interaction forces, which can be used to derive the elastic modulus and other mechanical properties (Heinz & Hoh, 1999).

Conventional FD-based AFM uses the contact mode, also referred to as force-volume imaging (Figure 2-3 B), and combines topographical and force data into the same dataset, thus allowing for correlation between topographical and mechanical features. It associates each coordinate with a FD curve. From this array of FD curves, a spatial map of mechanical features on the sample surface can be acquired. The time required for recording a single FD curve is approximately 0.1 to 10 seconds (Heinz & Hoh, 1999). It thus would take minutes to hours to acquire a high resolution stiffness image. Such poor temporal resolution largely limits the application of FD-based AFM force spectroscopy in cell mechanics. In addition, the huge amount of force-volume data is usually processed offline to extract mechanical features, making it difficult to visualize the results during AFM imaging. Most discoveries mentioned in 2.2 used this slow version FD-based AFM, which performs well in measuring whole cell stiffness, but at the sub-cellular level, can be very time-consuming to achieve high resolution images and may not capture fast cellular changes.

Recently, the introduction of faster hardware elements, data acquisition systems, and specially designed cantilevers, allows for simultaneous topographical and mechanical imaging at high speed and high resolution using multi-frequency tapping-mode AFM (Dufrene, Martinez-Martin, Medalsy, Alsteens, & Muller, 2013). Conventional tapping-mode AFM excites and detects a single frequency of the tip motion, providing time-averaged values of the tip-sample interactions. By contrast, multi-frequency AFM takes advantage of the non-linearity of cantilever dynamics, and uses excitation and/or detection of several frequencies during the cantilever oscillation. These frequencies are associated with either higher oscillation harmonics or the eigenmodes of the cantilever (Garcia & Herruzo, 2012). Time-resolved tip-sample interaction forces can then be derived from higher harmonics, allowing for the measurement of forces at microsecond scale (M. Stark, Stark, Heckl, &

Guckenberger, 2002). Several multi-frequency AFM techniques have been developed and used in the high speed mechanical imaging of biological samples, such as the multiharmonic AFM imaging developed by Raman et al. (Raman et al., 2011) and the torsional harmonic AFM developed by Sahin et al. in our lab (Dong et al., 2009; Sahin et al., 2007).

2.4 Torsional harmonic AFM

Multi-frequency AFM using higher harmonics presents several challenges in cell mechanics imaging. First, the amplitudes of higher harmonics components are several orders of magnitude smaller than the fundamental frequency component (Rodriguez & Garcia, 2002). Thus the signal-to-noise ratios of higher harmonics are not sufficient for practical measurements. Second, time-resolved force measurement requires a relatively large number of harmonics (~15) in order to get accurate estimation of the force, which requires special cantilever designs. Third, the frequency spectra of the cantilever used for time-resolved force measurements depend on the shape the cantilever eigenmodes and laser spot position, which are difficult to measure accurately (R. W. Stark, 2004). In addition, in soft biological samples, it is crucial to adjust and monitor the tapping force in real time accurately to prevent cells from large deformation and damage. Therefore, a fast online data processing and time-resolved force measurement is preferred.

To tackle these challenges in the multi-frequency AFM, Sahin et al. introduced a new type of multi-frequency AFM: torsional harmonic AFM (TH-AFM) (Sahin et al., 2007). TH-AFM uses a specially designed T-shaped cantilever where the tip is offset from the long axis of the cantilever, and generates higher harmonics from the torsional signal (Sahin & Erina, 2008; Sahin et al., 2007), as shown in Figure 2-4. During TH-AFM imaging, the interaction forces generate a torque around the long axis of the cantilever and excite the torsional mode. Similar to the conventional tapping-mode AFM, the flexural deflection of the cantilever is monitored by the vertical position of the laser spot on the photodetector, which is used as the amplitude feedback for topographical imaging.

Simultaneously, the torsional deflection is monitored by the horizontal position of the laser spot, which is used to calculate the time-resolved tip-sample interaction forces in real time (Sahin et al., 2007).

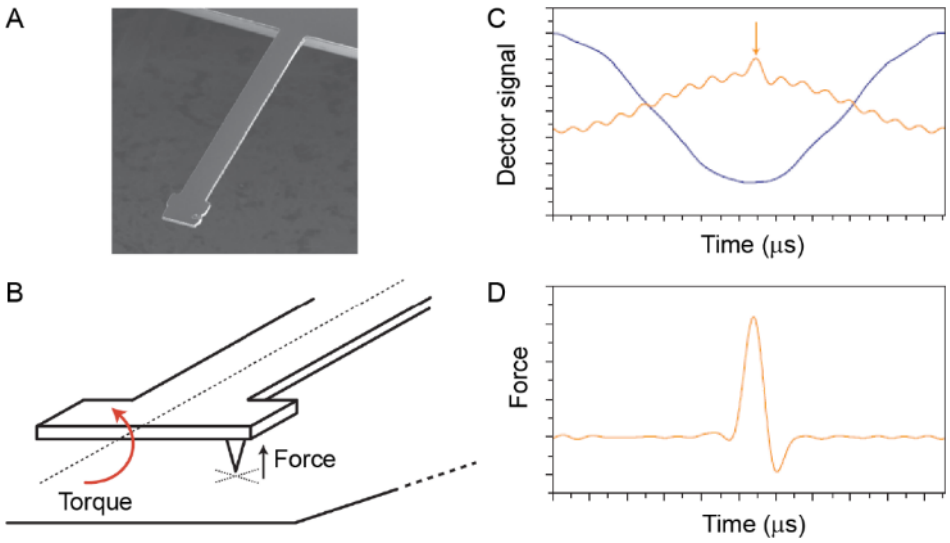

Figure 2-4 Torsional harmonic AFM.
(A) A scanning electron micrograph image of a torsional harmonic T-shaped cantilever. The tip is offset from the center of the cantilever. (B) A schematic diagram of the T-shaped cantilever interacting with the surface. The offset position of the tip results in a torque around the long axis of the cantilever. (C) Periodic flexural (blue) and torsional (orange) vibration signals from a quadrant photodetector when the cantilever is oscillated at its flexural resonance frequency. (D) Time-resolved tip-sample force measurements from the torsional harmonic signals. Images are reprinted and adapted with permission from (Sahin et al., 2007), © 2007 Nature Publishing Group.

Thanks to its high signal-to-noise ratio, high force sensitivity, and high spatiotemporal resolution, TH-AFM has been used to map Young's modulus on purple membranes (Dong et al., 2009) and living fibroblasts (Mandriota, 2016), detect DNA molecules (Husale, Persson, & Sahin, 2009), and recognize single molecule interactions (Dong & Sahin, 2011).

Next in Chapter 3, I will describe how to use TH-AFM to measure the nanomechanical properties of live hippocampal neurons.

Chapter 3 Live nanomechanical imaging with TH-AFM reveals stiff synapse-like structures

Synapses are deeply buried in the brain under a protective skull, whiles AFM is designed specifically for surface profiling. How can we then bring the AFM tip to a single synapse and measure its mechanical properties? To study cells outside their original biological context which is referred to as "in vivo", biologists have long been doing "test-tube experiments" which is referred to as "in vitro". In vitro studies isolate cells from their often inapproachable in vivo environment, and enable a more convenient and detailed analysis. By isolating neurons from the brain and culturing them in a petri dish, we can approach live synapses with AFM.

In this Chapter, I will describe the experimental set up and results from live nanomechanical imaging of in vitro neuron cultures with TH-AFM.

3.1 Materials and Methods

3.1.1 Hippocampal neuron culture preparation

Animal work was approved by the Columbia University Institutional Animal Care and Use Committee. Hippocampal neuron cultures were prepared following a modified version of the previously described Brewer method (Brewer, Torricelli, Evege, & Price, 1993). Fetuses at embryonic day 18 (E18) from timed pregnant Sprague-Dawley rats (Taconic Farms; Hudson, NY) were sacrificed and the hippocampi removed and collected in room temperature Hank's balanced salt solution (HBSS-; Thermo Fisher Scientific 14025076), supplemented with 0.6% (w/v) glucose (HBSS+). The hippocampi were then incubated in 0.05% trypsin (Thermo Fisher Scientific 25300054) for 15 minutes at 37°C and washed with HBSS+ three times for 10 minutes each. Finally, the neurons were dissociated in Neurobasal medium (Thermo Fisher Scientific 21103-049) supplemented with B27 supplements (Thermo Fisher Scientific 17504-044) and 0.5 mM L-Glutamine (Thermo Fisher Scientific 25030). Neurons were plated at a density of 100,000 cell/mL in glass bottom dishes coated with 1 mg/mL poly-L-lysine (Sigma-Aldrich P2636) and 10 μg/mL mouse protein laminin (Thermo Fisher Scientific 23017-015). 50 mm glass bottom dishes (WillCo GWSt-5040) were used in most experiments unless otherwise specified. The resulting neuronal cultures consisted of a population enriched in large pyramidal neurons. Cultures were maintained in 5% CO_2 humidified incubator at 37°C and used after 14-25 days *in vitro* (DIV) to image mature synapses, and DIV 5-7 to image immature protrusions. Before imaging, culture medium was replaced with Tyrode's buffer (125 mM NaCl, 2 mM KCl, 3 mM $CaCl_2$, 1 mM $MgCl_2$-$6H_2O$, 10 mM HEPES, 30 mM D-glucose, adjusted to 300 mOsm with sucrose, pH adjusted to 7.4 with NaOH) (Kralj, Douglass, Hochbaum, Maclaurin, & Cohen, 2012) at room temperature. Neuronal activities were verified with calcium indicator Oregon Green (Thermo Fisher Scientific O6807) showing neuron firing.

3.1.2 Torsional harmonic cantilevers

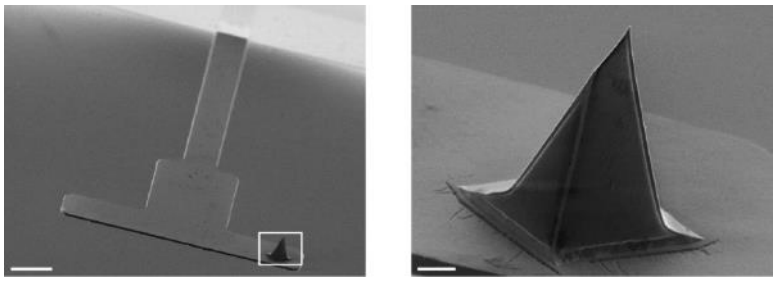

Figure 3-1 T-shaped cantilever.
Scanning electron micrograph images of a T-shaped cantilever with a pyramidal tip. Scale bar: 10 μm, 1 μm.

T-shaped cantilevers were custom made by Bruker-Nano, Inc (Figure 3-1)(Sahin et al., 2007) with the following specifications: the cantilever bodies were made of silicon nitride and the tip was made of silicon. The length, width, and thickness of the cantilevers were nominally 85 μm, 9 μm, and 650 nm. The width at the free end was 60 μm, and the tip offset 25 μm, tip height 5 μm or 6.5 μm. Cantilevers were coated with silicon nitride via plasma-enhanced chemical vapor deposition to a radius of 75nm or 100 nm. Flexural and torsional deflection sensitivities of cantilevers were determined from ramp plots, assuming flexural and torsional motions to be described by springs in series. The spring constants of flexural (approximately 0.2 N/m) and torsional (approximately 1.0 N/m) deflections were determined from the respective thermal noise spectra. The drive frequency (9 - 23 kHz) used during cantilever oscillation was determined from thermal tune.

3.1.3 Atomic force microscopy imaging

Glass bottom dishes were mounted on the stage of an inverted fluorescence microscope Axio Observer Z1 (Zeiss) and neurons were perfused with Tyrode's buffer during imaging (Figure 3-2). TH-AFM experiments were performed with BioScope Catalyst (Bruker) and imaging was carried out in fluid tapping mode. T-shaped cantilevers were analyzed in real time to create topographical and mechanical maps as previously described (Sahin et al., 2007). The set point amplitude was approximately 45 nm and the tip-sample interaction force was approximately 300 pN. Elastic modulus was calculated by fitting the force-distance curves with a Derjaguin-Muller-Toporov (DMT) model

(Derjaguin, Muller, & Toporov, 1994) with a hemispherical indenter (see 6.1.2 and 6.1.3 for additional discussion about elastic modulus calculation). All AFM images were recorded with 512 pixel × 256 pixel, 256 pixel × 256 pixel, or 256 pixel × 128 pixel over areas of 5 μm × 5 μm to 25 μm × 25 μm with a scan rate 0.5 to 1.5 Hz.

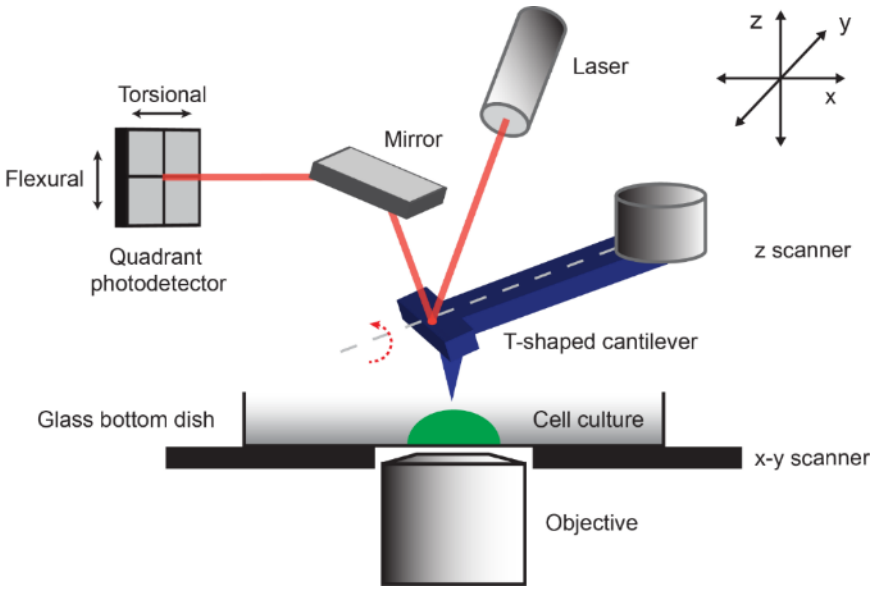

Figure 3-2 Nanomechanical imaging platform.
A schematic diagram illustrating the set-up of the nanomechanical imaging platform. Neurons (green) were cultured in a glass bottom dish. TH-AFM imaging was performed by scanning a sharp tip across the sample surface while the interaction force between the tip and the sample was monitored. A microfabricated T-shaped cantilever was vibrated at its resonance frequency and was able to detect both vertical and torsional deflection signals of the cantilever during scanning of the sample in three dimensions x, y, and z. The vertical signal is used for the height feedback to generate the topographical image and the torsional signal provides instantaneous force to calculate mechanical properties during the imaging process.

3.1.4 Atomic force microscopy data analysis

AFM data were processed and analyzed with NanoScope Analysis 1.70 (Bruker), SPIP 5.0 (Image Metrology), Gwyddion, and ImageJ. For quantitative measurement, in order to reduce noise, a 3×3 median filter was applied to stiffness images. Due to edge effect, AFM measurement is more reliable on top of a structure close to the center, and less so close to the edge. Thus, I selected areas of interest (AOI) of at least 10 pixel × 10 pixel close to the center on a spine structure identified by the topographical image, and used the maximum value in the AOI to represent the elastic modulus of

a spine. I noticed that the stiffness of a dendritic shaft and an immature protrusion did not vary substantially along its length. I thus drew a section line of at least 10 pixels along the length of a shaft structure or an immature protrusion close to its centerline, and used the average value along the section to represent the elastic modulus of a shaft and a filopodium, respectively. For intensity profile in Figure 4-5 B and Figure 6-8 C, raw elastic modulus data were used. For visualization purpose only, a low pass filter was applied to height images; spike removal with vertical interpolation and local mean equalization were applied to stiffness images.

3.2 Results and Discussion

AFM imaging requires a direct contact between the AFM tip and the sample, and relies on piezoelectric elements to control the three-dimensional positioning and force feedback. As a result, AFM is suitable to image a relatively small and flat surface area, and live cell imaging with AFM is mostly done on sparsely cultured cells *in vitro* (Cross et al., 2007; Matzke et al., 2001; Muller & Dufrene, 2011; Rotsch & Radmacher, 2000; Smith et al., 2007; Spedden et al., 2012). In some cases, AFM is used to measure the stiffness of tissue slices which preserve local cellular context. For example, AFM stiffness images showed distinct stiffness profiles of human breast biopsies (Plodinec et al., 2013). AFM indentation on thin slices of brain tissue revealed different stiffness between white and gray matter at micrometer resolution (Christ et al., 2010). However, the resolution of tissue-based AFM is limited to at best single cells (Plodinec et al., 2013), not sufficient for subcellular structures such as synapses. In order to probe synapses which are tiny structures and are usually surrounded by other cellular components *in vivo*, we need to dissect primary neurons from the brain and culture dissociated neurons *in vitro* (Brewer et al., 1993), creating a relatively flat layer of neurons with synapses exposed to the surface and accessible to the AFM tip.

The *in vitro* neuron culture, as an important neuroscience technique, has its pros and cons (Humpel, 2015). On one hand, it allows a single homogeneous cell population to be studied in an

isolated environment, making it convenient to perform well-controlled experiments and studies of cell morphology, function, survival, and toxicity. It also largely reduces the number of experiment animals and their suffering. *In vitro* rat primary hippocampal neuron cultures have been widely used to study spine development (Papa, Bundman, Greenberger, & Segal, 1995), synaptic activity (Kay, Humphreys, Eickholt, & Burrone, 2011), synaptic plasticity (Molnar, 2011), and disease models (Pozueta, Lefort, & Shelanski, 2013). On the other hand, due to a lack of contact with other cells and original local cellular architecture, the reconstructed dissociated cells do not fully represent their *in vivo* nature. For example, neurons in cultures have lower spine density and more shaft synapses than those in the brain (Boyer, Schikorski, & Stevens, 1998). Therefore, it is important to note that the results reported here may not be readily applicable to *in vivo* neurons given the limitations of *in vitro* culture.

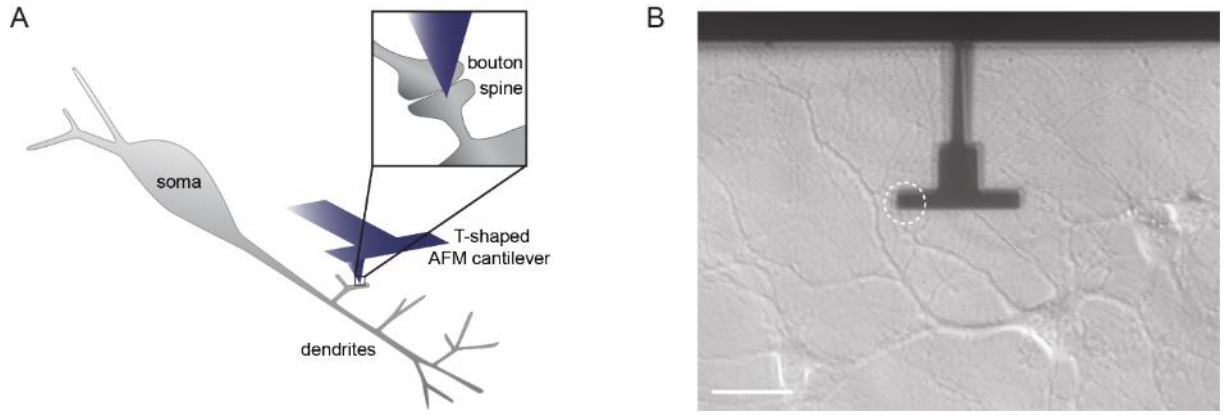

Figure 3-3 Nanomechanical imaging of live cultured neurons.
(A) A schematic diagram illustrating live nanomechanical imaging of cultured neurons. TH-AFM imaging was performed by scanning a T-shaped cantilever with a sharp tip across the sample surface while the interaction force between the tip and the sample was monitored. The zoomed-in inset shows the AFM tip over a synapse. (B) Optical image of a T-shaped cantilever over a neuron culture. The tip was facing towards the culture dish, and was placed on the left side of the cantilever (indicated by the dashed circle). Scale bar: 40 μm.

I characterized the nanomechanical properties of live hippocampal neurons on 14-25 days *in vitro* (DIV) using torsional harmonic atomic force microscopy (TH-AFM) (Figure 3-3 A). TH-AFM uses a T-shaped cantilever with an offset tip and detects both vertical and torsional deflection signals of the cantilever during scanning of the sample. The vertical signal is used for the height feedback to generate the topographical image and the torsional signal provides instantaneous force to calculate

mechanical properties during the imaging process with a customized LabView program (Sahin et al., 2007).

Rat hippocampal neurons were cultured in glass bottom dishes and live neurons were imaged in Tyrode's buffer at room temperature. To capture the corresponding optical images, the TH-AFM apparatus was placed above an inverted optical microscope (see 3.1.2, 3.1.3, Figure 3-2 for experiment set-up). Hippocampal neurons were characterized as large pyramidal cell bodies with long axons and branched dendritic shafts, forming complex neurite networks (Figure 3-3 B).

Neuron density in the culture is critical because AFM imaging requires a direct contact between the tip and the sample, thus low-density neuron cultures with synapses exposed to the surface are preferred. Meanwhile, neuron density largely affects neuron viability(Brewer et al., 1993), dendrite morphology, synaptic density, and neuron network activity (Biffi, Regalia, Menegon, Ferrigno, & Pedrocchi, 2013; Cullen, Gilroy, Irons, & LaPlaca, 2010; Ivenshitz & Segal, 2010; Previtera, Langhammer, & Firestein, 2010). Thus, high-density neuron cultures with complex neurite networks are preferred in the long-term culture. I optimized neuron density with a tradeoff between AFM accessibility and neuron activity, and used a density of 100,000 neurons/mL, resulting in a surface density of approximately 240 neurons/mm^2 in the glass bottom dish. I verified the activity of the cultured neuron with calcium indicator Oregon Green (Grienberger & Konnerth, 2012) and observed neuron firing. In this work, hippocampal neuron cultures were prepared following a modified version of the previously described Brewer method (see 3.1.1 for the culture preparation method). An alternative method for neuron cultures is to add a glial feeder layer, which could help neuron survival at even lower density (Banker, 1980; Ivenshitz & Segal, 2010). However, the existence of the glial cells may complicate AFM imaging and increase background noise. Therefore, I did not use the glial feeder layer in neuron cultures.

To minimize forces acting on delicate neuronal structures, I used low peak tapping forces

(around 300 pN) and small indentation depth (around 30 nm) during scanning (Figure 3-4 A).

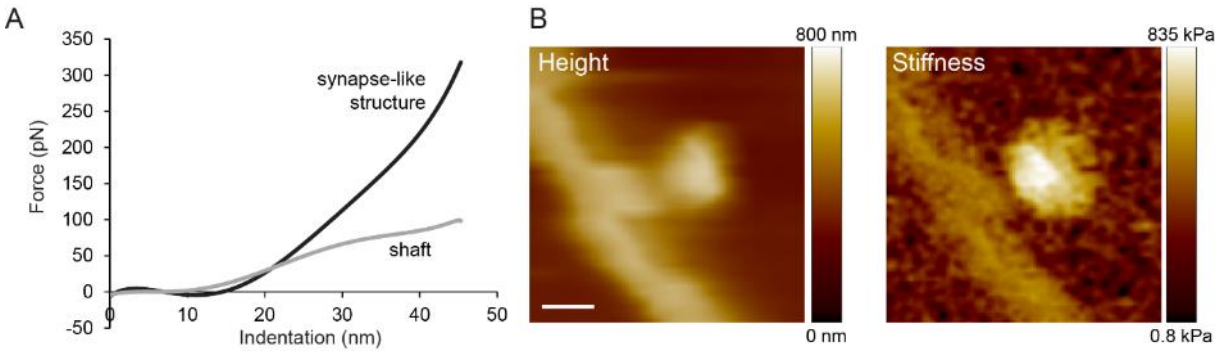

Figure 3-4 Force-distance curves during TH-AFM imaging.
(A) Representative force-distance curves on a synapse-like structure (black) and a dendritic shaft (grey) during tip approach. (B) TH-AFM height and stiffness images of the stiff synapse-like structure in A. The color in AFM images represents height (linear scale) and elastic modulus (log scale) respectively. The elastic modulus values of the stiff structure and the shaft are 509.0 kPa and 42.9 kPa, respectively. Scale bar: 1 μm.

Our imaging technique generates topographical and mechanical images of neuronal structures simultaneously during live imaging at nanometer resolution as shown in Figure 3-4 B. See 3.1.4 for quantitative stiffness measurement of areas of interest such as synapse-like structures and shafts. In short, after reducing the noise in AFM raw images, I used the maximum value to represent the elastic modulus of a synapse-like structure and the average value along the centerline to represent the elastic modulus of a shaft.

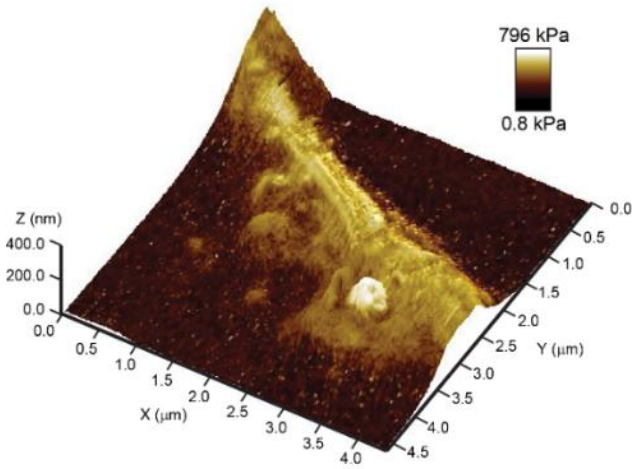

Figure 3-5 Three-dimensional AFM image of a stiff synapse-like structure in live neurons.
Three-dimensional topographical rendering of a synapse-like structure with the color indicating elastic modulus in log scale. The elastic modulus values of the stiff structure and the shaft are 626.8 kPa and 38.6 kPa, respectively.

A three-dimensional topographical rendering of a synapse-like structure with the color

indicating elastic modulus is shown in Figure 3-5. Within the network of processes, I observed surprisingly stiff synapse-like structures near compliant neurites. I used the following criteria for visually-identified synapse-like structures under TH-AFM: (i) distinct structures with stiffness over 20 kPa in the mechanical image, (ii) height below 1.5 μm and (iii) in close proximity (within 2 μm) to a nearby neurite in the topographical image. Based on these criteria, I acquired AFM images of hundreds of synapse-like structures and nearby shafts (see 3.1.4 for quantitative stiffness measurement of areas of interest), and found that 77.8% of synapse-like structures had a stiffness over 100 kPa (see Chapter 6 for detailed quantitative analysis). Based on their morphology and proximity to neurites, I hypothesized that these stiff structures could be synapses.

Interestingly, time-lapse TH-AFM imaging showed that these stiff synapse-like structures revealed by TH-AFM were very stable. Their stiffness did not vary significantly during imaging (Figure 3-6). This observation of stable synapse-like structures is consistent with previous reports that spine morphology is largely stable over periods of an hour (Tonnesen, Katona, Rozsa, & Nagerl, 2014).

In AFM imaging, the tapping force was kept at around 300 pN and indentation depth was around 30 nm to prevent the sample from being irreversibly deformed and damaged. Compared with the typical spine diameter of 1 μm, the AFM indentation depth is relatively small and thus would not disrupt spine structures. It is worth mentioning that applying force during measurement may activate mechanosensitive ion channels in neurons, thus affecting neuron function and synaptic activity. Although I did not study how mechanical stimulation changes neuron function, it would be interesting in the future to use different force values and indentation depths and understand whether and how neurons can be activated mechanically.

It has been shown that the elastic moduli of hydrogels and spine-like structures in neurons display a frequency dependence at low frequency (Smith et al., 2007; Yang, Wong, de Bruyn, & Hutter, 2009). In my measurement, I used a fixed drive frequency as described in 3.1.2 with the resonance

frequency at the kHz level. The resonance frequency of cantilevers is influenced by many factors, such as the geometry of the cantilever and the thickness of the silicon nitride coating. I used cantilevers with slightly different frequencies assuming the measurement of elastic moduli was not significantly affected by such difference.

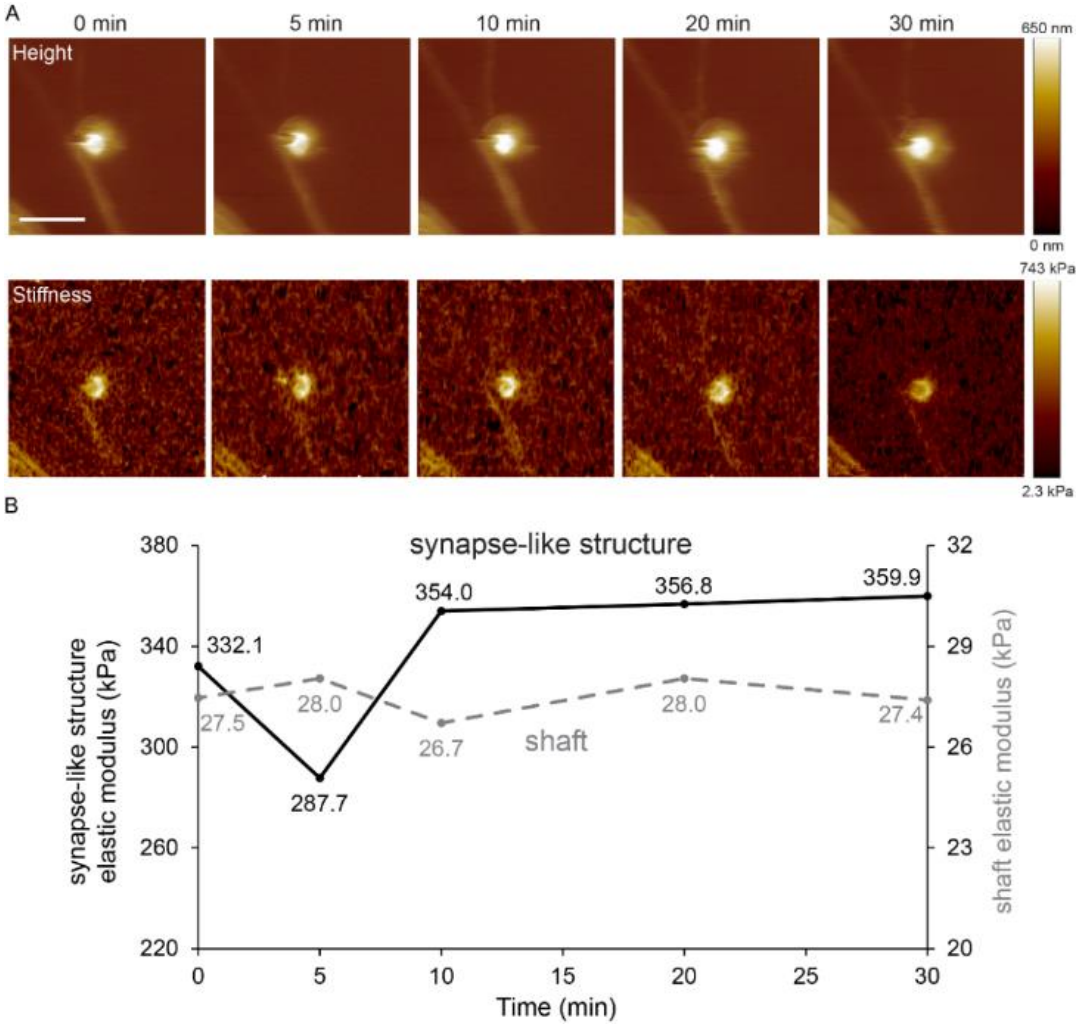

Figure 3-6 Stiffness of a synapse-like structure does not vary significantly during imaging.
(A) Time-lapse TH-AFM height and stiffness images of a synapse-like structure. The same area was scanned with TH-AFM at 0, 5, 10, 20, 30 min. Scale bar: 2 μm. (B) Stiffness of the synapse-like structure (black solid line) and shaft (grey dashed line) did not change drastically over 30 minutes. The stiffness of the synapse-like structure dropped to 287.7 kPa from 332.1 kPa at 5 min (13.4% decrease compared to 0 min) and increased to 354.0 kPa at 10 min (6.6% increase compared to 0 min). These variations were small and could probably be due to measurement uncertainty.

Next in Chapter 4, I will combine TH-AFM with fluorescence microscopy and verify the identity and activity of synapse-like structures.

Chapter 4 Correlative TH-AFM/fluorescence imaging reveals stiff and functional mature excitatory synapses

AFM is a label-free imaging technique. Think of it as X-ray imaging: while the same X-ray can be used on different people, it cannot identify who a person really is. That's why you may not want to use your recent X-ray photo taken from a radiologist's office on a passport. Instead, a portrait photo is probably a better idea. Similarly, the label-free property of AFM provides versatility. The same AFM cantilever can potentially be used for different samples without much modification. However, this also brings in ambiguity, because topographical and mechanical features do not well specify cellular identity. In order to take a portrait photo of cells, we could label them with special biochemical markers and rely on fluorescence imaging.

In this Chapter, I will describe correlative TH-AFM/fluorescence imaging to verify the identity and activity of stiff synapse-like structures.

4.1 Materials and Methods

4.1.1 Immunocytochemistry

The primary antibodies used were PSD-95 (1:1,000, mouse; Abcam ab99009) and Synapsin-1 (1:1,000, rabbit; Cell Signaling 5297). The secondary antibodies used were Alexa Fluor® 488 Goat Anti-Mouse (1:5000, Thermo Fisher Scientific A-11029), Alexa Fluor® 488 Goat Anti-Rabbit (1:5000, Thermo Fisher Scientific A-11034), Alexa Fluor® 546 Goat Anti-Mouse (1:5000, Thermo Fisher Scientific A-11030), Alexa Fluor® 546 Goat Anti-Rabbit (1:5000, Thermo Fisher Scientific A-11035), Cy5® Goat Anti-Mouse (1:5000, Thermo Fisher Scientific A10524), Cy5® Goat Anti-Mouse (1:5000, Thermo Fisher Scientific A10523). After TH-AFM imaging, neurons were fixed with 4% (w/v) paraformaldehyde (Thermo Fisher Scientific 28908), permeabilized with 0.3% (v/v) Triton X-100 (Sigma-Aldrich 93443) in phosphate-buffered saline (PBS), and incubated with primary antibodies diluted in SuperBlock Blocking Buffer (Thermo Fisher Scientific 37515) overnight at 4°C. Neurons were then incubated with secondary antibodies at room temperature for 30 minutes to 2 hours.

4.1.2 Epifluorescence microscopy

Optical images were taken before and after TH-AFM imaging using an inverted microscope (Axio Observer Z1; Zeiss) at different magnifications (10X, 20X, 100X EC Plan-Neofluar, Zeiss). I used phase contrast at 10X and 20X and brightfield at 100X in optical imaging. After live imaging, the location of neurons of interest was marked by labeling the relative position of the perfusor (Bruker) to the dish, and the relative position of perfusor to the objective to ensure the same regions could be captured after immunocytochemistry. Fluorescence images were taken using the same epifluorescence microscope (Axio Observer Z1; Zeiss) with proper filter sets (Zeiss and Chrome) at 100X magnification (1.3 NA). All images were captured with a standard CCD camera (Hamamatsu) at 1344 pixel × 1024 pixel resolution. For F-actin imaging in Figure 7-4, same settings such as light power and exposure time were used in both DMSO and drug treated neuron cultures.

4.1.3 Functional labeling of presynaptic boutons with FM 4–64

At the end of the AFM experiment, neurons were incubated in high KCl Tyrode's buffer (77 mM NaCl, KCl 50 mM, 3 mM $CaCl_2$, 1 mM $MgCl_2$-$6H_2O$, 10 mM HEPES, 30 mM D-glucose, adjusted to 300 mOsm with sucrose, pH adjusted to 7.4 with NaOH) with 10 μM FM 4-64 for 45 seconds (Gaffield & Betz, 2006; Kay et al., 2011) and then washed with calcium-free Tyrode's buffer (125 mM NaCl, 2 Mm KCl, 1 mM $MgCl_2$-$6H_2O$, 10 Mm HEPES, 30 mM D-glucose, adjusted to 300 mOsm with sucrose, pH adjusted to 7.4 with NaOH) for 15 minutes to remove non-specific membrane bound FM 4-64. After FM 4-64 imaging, cells were washed with normal Tyrode's buffer for 30 minutes to remove trapped FM dyes, before being proceeded to immunocytochemistry.

4.1.4 Image processing

Optical images were processed and quantified with ImageJ and Caltracer 2 (available through: http://blogs.cuit.columbia.edu/rmy5/methods/). Background signal was measured by selecting dark regions in an image and plotting a Gaussian distribution histogram showing mean μ and standard deviation σ. The intensity of the whole image was then subtracted by $\mu + 3\sigma$ to remove noise. Subtraction processed images were then analyzed using Caltracer to identify colocalization. Puncta contours of each marker were detected using an automated algorithm based on fluorescence intensity, puncta size, and shape, and were adjusted by visual inspection. Contours of different markers (PSD-95 and Synapsin-1) were overlaid and a threshold of 5% overlap was used for all potential colocalization detection. Colocalized contours were counted and overlaid with stiffness images. Optical images and AFM images of the same area were aligned in Adobe Photoshop and visually inspected. For visualization purpose only, brightness and contrast was adjusted, median filter was applied, and pixel number was increased to smoothen the pixelated images in Adobe Photoshop. For quantitative analysis including fluorescence intensity profiles in Figure 4-5 B and Figure 6-6 C, raw fluorescence data were used unless otherwise specified.

4.2 Results and Discussion

In Chapter 3, I performed nanomechanical imaging of synapse-like structures with TH-AFM in live neurons. Aligned optical and AFM images of a large area (Figure 4-1) showed several highly stiff synapse-like structures (yellow arrows). These structures also displayed dark contrast in the optical image. Based on their morphology and proximity to neurites, I hypothesized they could be synapses.

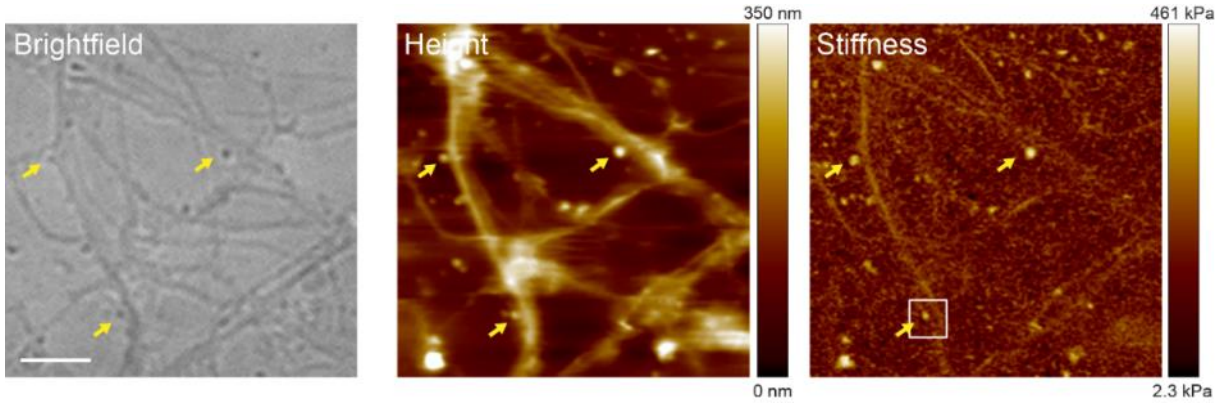

Figure 4-1 Optical and TH-AFM imaging reveals stiff synapse-like structures.
Aligned brightfield, AFM height, and AFM stiffness images of the same area in live neuron cultures. The color in AFM images represents height (linear scale) and elastic modulus (log scale) respectively. Scale bar: 3 μm. Yellow arrows point to representative stiff synapse-like structures. White boxed area in the stiffness image is highlighted in Figure 4-5.

To verify the identity of stiff structures revealed by TH-AFM, I performed immunostaining against various synaptic markers after TH-AFM imaging and correlated immunofluorescence images with AFM images**.** Combination of AFM and fluorescence microscopy has been used to reveal the mechanical structures of cytoskeleton in cells (Chacko et al., 2013; Curry et al., 2017). So far, to my knowledge, no correlative AFM stiffness mapping and fluorescence imaging of synapses has been reported. I used antibodies against presynaptic marker Synapsin-1 and postsynaptic marker PSD-95 to identify mature excitatory synapses.

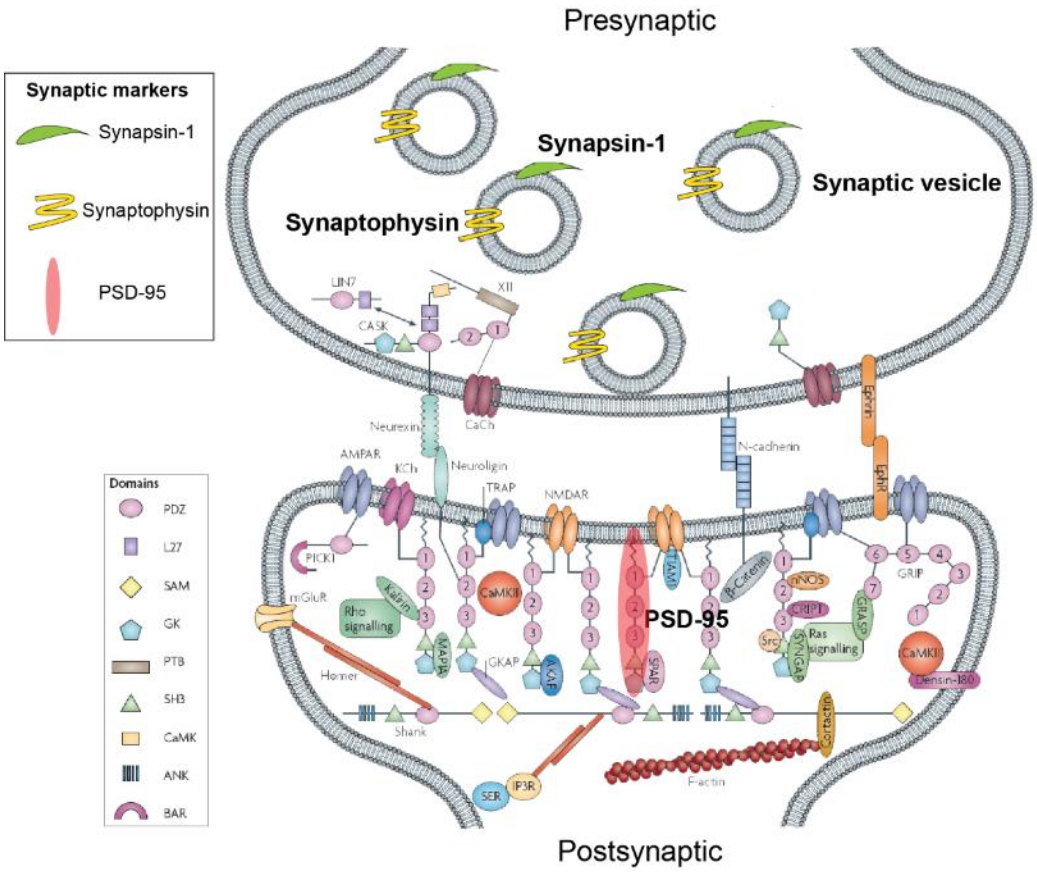

Figure 4-2 Molecular organization at synapse.
Synapsin-1 (green) and Synaptophysin (yellow) bind to synaptic vesicles at the presynaptic terminal and can be used as presynaptic markers. PSD-95 (red) is the major scaffolding protein in the postsynaptic density and can be used as a postsynaptic marker. It has multiple PDZ domains that bind to various synaptic proteins including α-amino-3-hydroxy-5-methyl-4-isoxazolepropionic acid receptors (AMPAR) and N-methyl-D-aspartate receptors (NMDAR). The postsynaptic density is comprised of membrane receptors and ion channels, scaffolding and adaptor proteins, signaling proteins, synaptic adhesion molecules, and cytoskeleton (predominately F-actin). The pre- and postsynaptic terminals are connected by synaptic adhesion molecules. The image is reprinted and adapted with permission from (Feng & Zhang, 2009), © 2009 Macmillan Publishers Limited.

Synapsin-1 (Figure 4-2, green) is a protein that reversibly binds to the cytoplasmic side of synaptic vesicles with high affinity and is enriched in presynaptic axon terminals at mature synapses (De Camilli, Harris, Huttner, & Greengard, 1983; T. L. Fletcher, Cameron, De Camilli, & Banker, 1991). Synapsin-1 also binds to cytoskeleton such as microtubule (Baines & Bennett, 1986) and F-actin (Bahler & Greengard, 1987). The phosphorylation state of Synapsin-1 regulates the clustering and release of synaptic vesicles and synaptic function (Greengard, Valtorta, Czernik, & Benfenati, 1993). PSD-95 (postsynaptic density protein 95, Figure 4-2, red), a membrane-associated guanylate

kinase, is the major scaffolding protein in the postsynaptic density at glutamatergic excitatory synapses (Cheng et al., 2006; Cho, Hunt, & Kennedy, 1992; Rao, Kim, Sheng, & Craig, 1998). It contains multiple PDZ domains (Feng & Zhang, 2009) that have been reported to bind to various postsynaptic proteins such as N-methyl-D-aspartate receptors (NMDAR) (Kornau, Schenker, Kennedy, & Seeburg, 1995) and α-amino-3-hydroxy-5-methyl-4-isoxazolepropionic acid receptors (AMPAR) (Nicoll, Tomita, & Bredt, 2006), and adhesion molecules (Irie et al., 1997)(Figure 4-2). PSD-95 provides a structural basis in the molecular organization of postsynaptic density (X. B. Chen et al., 2011) and plays a critical role in synaptic development and function (El-Husseini, Schnell, Chetkovich, Nicoll, & Bredt, 2000; Keith & El-Husseini, 2008). Given the characteristic sub-cellular localization of Synapsin-1 and PSD-95, antibodies against these two proteins have been widely used to label presynaptic vesicles and postsynaptic density in hippocampal neurons. Colocalization of these two synaptic markers thus provides highly reliable identification of mature excitatory synapses (see 4.1.4 for methods used to quantify colocalized puncta).

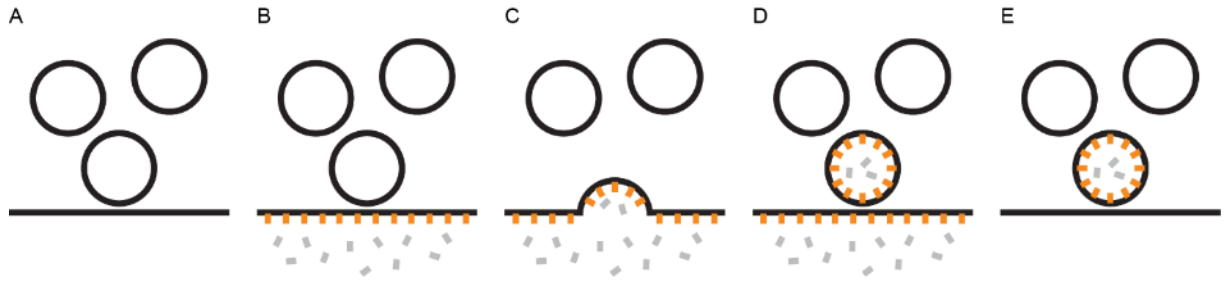

Figure 4-3 Functional labeling of synaptic terminals with FM dyes.
(A) Synaptic vesicles reside near the plasma membrane in the presynaptic terminal. (B) FM dyes are added, inserts into the plasma membrane and become fluorescent (orange), while they are virtually nonfluorescent (grey) in the aqueous solution. (C) After stimulation, a synaptic vesicle fuses with the plasma membrane to release neurotransmitter through exocytosis, exposing the luminal side to FM dyes. (D) The vesicle is endocytosed with FM dyes loaded on the inner leaflet of the vesicle membrane. (E) Washing out FM dyes in the extracellular solution allows only the stained vesicles inside neurons to be labeled and visualized under fluorescence microscopy.

To further characterize these stiff synapses and monitor their activity, I incubated live neurons with FM 4-64 dyes after TH-AFM imaging (see 4.1.3 for the functional labeling method). FM dyes were originally synthesized by Fei Mao (therefore the name, FM) to image synaptic vesicles in living

preparations (Betz, Mao, & Bewick, 1992) and have been used to study the kinetics of synaptic vesicle recycling and synaptic activity in cultured hippocampal neurons (Gaffield & Betz, 2006; Ryan et al., 1993). FM dyes are water-soluble and non-toxic to cells. The excited-state charge transfer of FM dyes is solvent polarity-dependent. In polar aqueous solvents such as culture medium and imaging buffer, FM dyes are virtually nonfluorescent, while in hydrophobic environments such as membranes they become intensely fluorescent (Gaffield & Betz, 2006). This unique property of FM dyes creates a high contrast membrane labeling that can be visualized by fluorescence microscopy. As shown in Figure 4-3, FM dyes insert into the outer leaflet of the plasma membrane and become intensely fluorescent. In neurons, stimulation evokes exocytosis and the release of neurotransmitters at the presynaptic terminal, followed by a compensatory endocytosis to retrieve synaptic vesicle membranes (Heuser & Reese, 1973). FM dyes get internalized within the recycled synaptic vesicles and thus only label functional presynaptic terminals with neurotransmitter release (Gaffield & Betz, 2006; Kay et al., 2011). Presence of synaptic vesicles at presynaptic terminals does not guarantee that synapses are functional. Approximately half of synaptophysin (a synaptic vesicle protein, marked in yellow in Figure 4-2)-labeled presynaptic terminals have FM puncta (Korkotian & Segal, 2001), suggesting that a substantial proportion of synapses are not functional. Therefore, functional labeling with FM dyes provides information about synaptic activity complementary to synaptic marker antibodies.

Figure 4-4 shows the fluorescence images of the same area as in Figure 4-1 after TH-AFM imaging. Images from different imaging methods were aligned based on neurite morphology using Adobe Photoshop. TH-AFM imaging, FM labeling, and immunocytochemistry preparation did not perturb the structures of neurites and synapses.

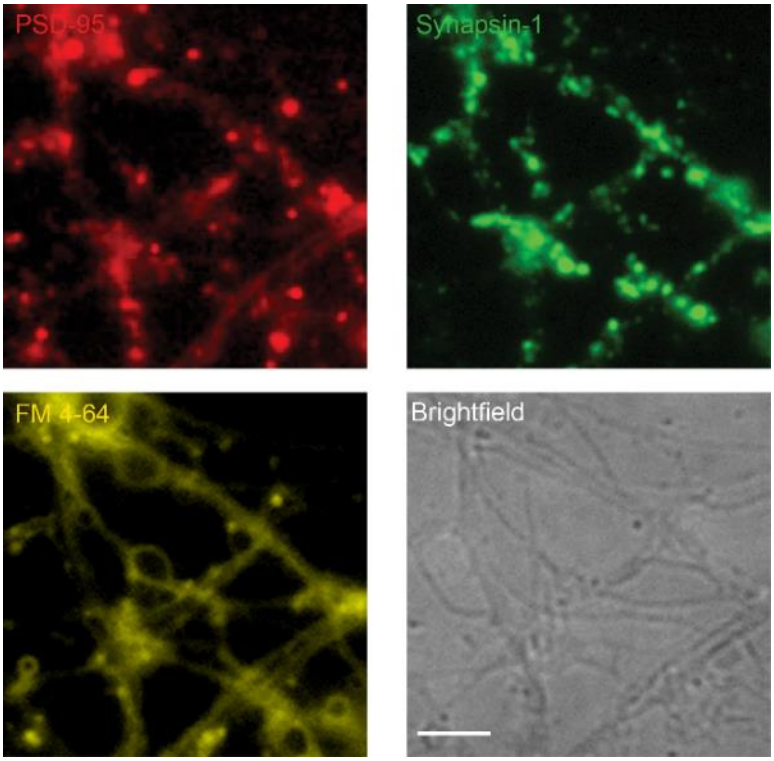

Figure 4-4 Fluorescence imaging of neurons after TH-AFM.
Fluorescence imaging of synaptic markers PSD-95 (red), Synapsin-1(green), and FM 4-64 (yellow) of the same area in Figure 4-1 after TH-AFM imaging. Scale bar: 3 μm.

Figure 4-5 A shows representative AFM height and stiffness images and the corresponding fluorescence imaging results of a synapse from the boxed area in the stiffness image in Figure 4-1. For visualization, a threshold was applied to the stiffness image and recolored the stiffness image in blue. Overlaid stiffness and fluorescence images showed that stiff structures were co-labeled with both PSD-95 and Synapsin-1. I acquired aligned AFM/immunofluorescence images of 263 synapse-like structures and found that all these stiff structures were co-labeled with both Synapsin-1 and PSD-95 (Figure 4-6 A1, A2), suggesting that stiff synapse-like structures were indeed mature excitatory synapses. Aligned AFM/FM images showed that stiff structures were colocalized with FM puncta as well (Figure 4-5 A and Figure 4-6 B1, B2), indicating that these synapses were also functional. Fluorescence intensity and elastic modulus profiles showed that high stiffness overlapped with synaptic markers and the FM dye (Figure 4-5 B).

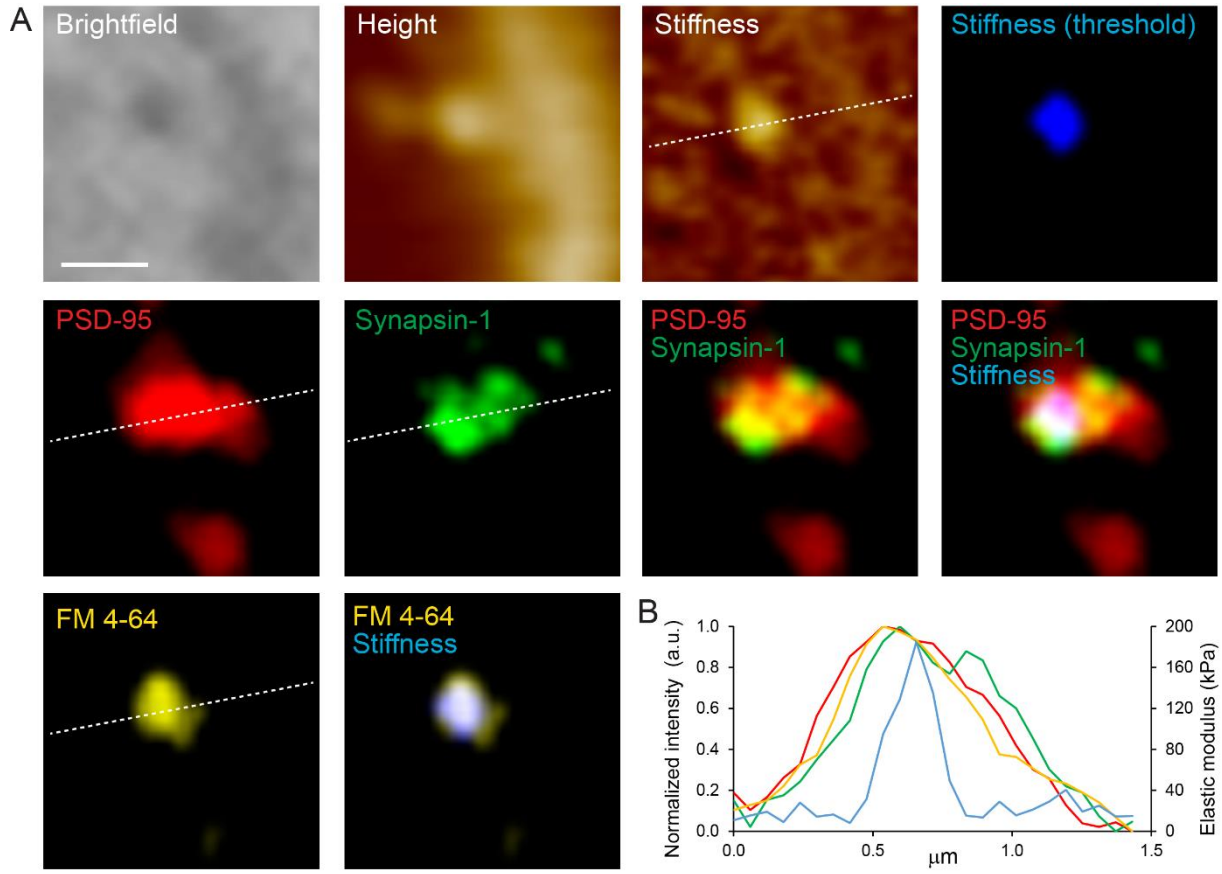

Figure 4-5 Correlative TH-AFM/fluorescence imaging shows stiff synapse-like structures are functional mature excitatory synapses.
(A) Aligned brightfield, AFM height, AFM stiffness and fluorescence images of a representative stiff synapse from the boxed area shown in the stiffness image in Figure 4-1. After TH-AFM imaging, neurons were fixed and stained with postsynaptic marker PSD-95 (red) and presynaptic marker Synapsin-1 (green). Colocalization of these two markers identified mature synapses. Threshold was applied to the stiffness image colored in blue. An overlay image of stiffness, PSD-95 and Synapsin-1 showed the stiff structure was a mature synapse. In addition, neurons were stained with FM 4-64 (yellow) after TH-AFM imaging to label functional synapses. Scale bar: 500 nm. (B) Fluorescence intensity and elastic modulus profiles along the dashed lines over the synapse in (A) showed that high stiffness (blue) overlaps with synaptic markers, PSD-95 (red), Synapsin-1 (green), and FM 4-64 (yellow). Note elastic modulus has a narrower peak than fluorescence signals.

Although fluorescence imaging with synaptic markers allows us to identify mature synapses, conventional optical microscopy has a resolution limit of 200 nm due to diffraction, making it difficult to localize target proteins and cellular structures with high resolution, or to distinguish pre- and postsynaptic components. Indeed, as shown in Figure 4-5 B, fluorescence signals have wider peaks than AFM measurements. Recently, the development of super-resolution fluorescence microscopy surpasses the resolution limit and provides more accurate localization of synaptic proteins (Dani,

Huang, Bergan, Dulac, & Zhuang, 2010). It is interesting to combine AFM with super-resolution microscopy in the future to investigate how spine stiffness correlates with different synaptic proteins both qualitatively and quantitatively.

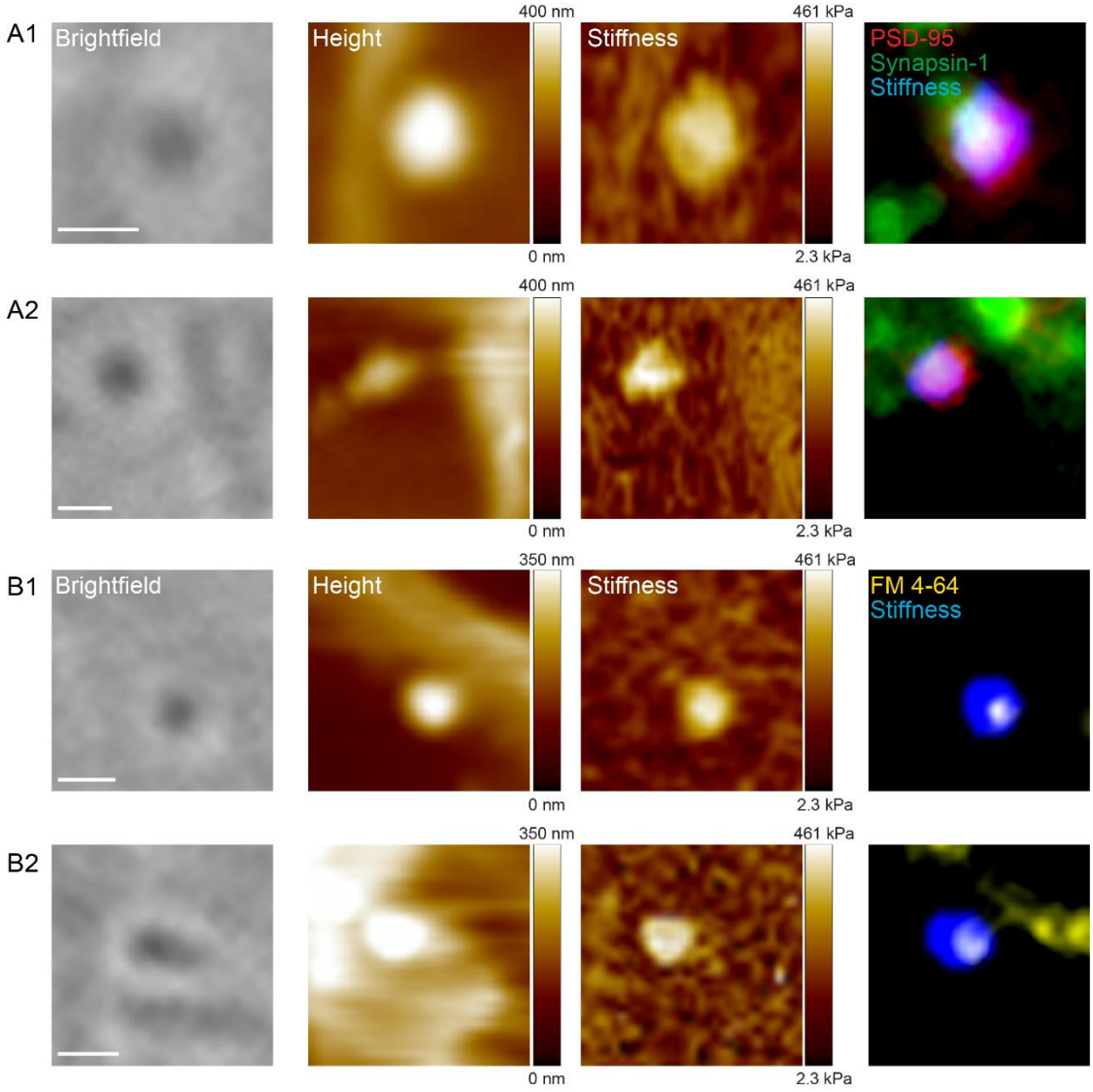

Figure 4-6 Stiff synapse-like structures are labeled with synaptic markers.
(A1)(A2) Aligned brightfield, AFM height, AFM stiffness, and immunofluorescence images of two representative stiff synapses labeled with both synaptic markers. 263 synapses from 20 neuron cultures were imaged with TH-AFM and aligned with immunofluorescence images. Threshold was applied to the stiffness image colored in blue. The elastic modulus values of 2 synapses are 271.3 kPa and 363.5 kPa, and the elastic modulus values of shafts are 37.3 kPa and 30.9 kPa. (B1)(B2) Aligned brightfield, AFM height, AFM stiffness, and fluorescence images of two representative stiff synapses labeled with FM 4-64. 97 synapses from 7 neuron cultures were imaged with TH-AFM and aligned with FM images. The elastic modulus values of 2 synapses are 310.8 kPa and 190.7 kPa, and the elastic modulus values of shafts are 24.6 kPa and 26.6 kPa. Scale bar: 500 nm.

Taken together, the data confirm that stiff structures identified under TH-AFM in cultured neurons were functional and mature excitatory synapses.

Next in Chapter 5, in order to further understand the characteristics of stiff synapses, I will combine TH-AFM with another nanoresolution imaging technique: transmission electron microcopy.

Chapter 5 Correlative TH-AFM/TEM imaging reveals ultrastructure of stiff synapses

Resolution describes the ability of an imaging system to resolve details in the object being imaged. Higher resolution means more image detail. Due to diffraction, optical microscopy has a resolution limit of 200 nm, which is not sufficient to visualize complex synaptic nanostructures such as synaptic cleft (20 nm in width), synaptic vesicles (40 nm in diameter), and postsynaptic density (40 nm in thickness). In contrast, electron microscopy uses a beam of electrons instead of photons and achieves a much higher resolution, allowing for the high resolution imaging of synaptic ultrastructure.

In order to understand how surface mechanics is related to synaptic ultrastructure, in this Chapter, I will combine TH-AFM with transmission electron microscopy.

5.1 Materials and Methods

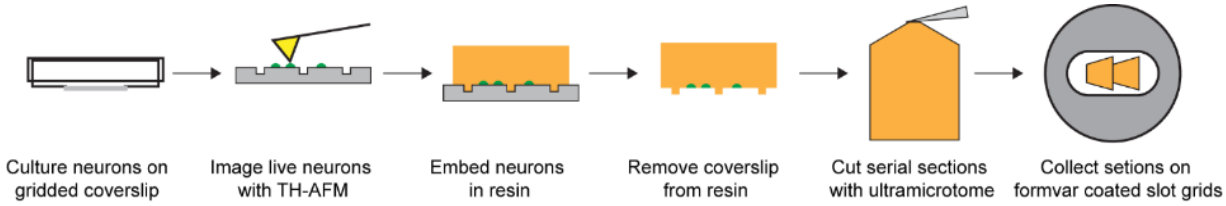

Figure 5-1 Workflow of correlative TH-AFM/TEM imaging.
To correlate TH-AFM, TEM, and optical images of the same synapses, neurons (green) were cultured in a homemade glass bottom dish with a gridded coverslip. After TH-AFM imaging, neurons were fixed, stained, and embedded in resin (orange). The sample block was detached from the coverslip, trimmed to 70 nm serial ultrathin sections, and collected on formvar coated slot grids.

5.1.1 Sample preparation for TEM

To acquire the ultrastructure of synapses, neurons were cultured in homemade glass bottom dishes (Corning® 60mm TC-Treated Culture Dish 430166) on gridded coverslips (Electron Microscopy Sciences 72264-18 and 72265-50) (Figure 5-1). A coverslip was glued to the bottom of a petri dish with a hole of 1 cm in diameter using Dow Corning Sylgard 184 Silicone Elastomer Clear (Ellsworth Adhesives 4019862). After live optical and TH-AFM imaging, neurons were fixed in the dish with 2.5% (w/v) glutaraldehyde in 0.15 M sodium cacodylate buffer (pH 7.4) at room temperature for 1 hour and then at 4°C overnight. Neurons were then rinsed 3 times in 0.1 M cacodylate buffer at 4°C and post-fixed with 1% OsO_4 in 0.1 M cacodylate buffer at 4°C for 1 hour. After block staining with 1% uranyl acetate at 4°C for 1 hour, neurons were rinsed 3 times with ddH_2O at 4°C and dehydrated in a gradient of ethanol: 30%, 50%, 70% at 4°C for 5 minutes each, 85%, 95% at room temperature for 5 minutes each, and 100% four times for 5 minutes each. Neurons were infiltrated in 100% ethanol/Araldite 502 (Electron Microscopy Sciences 13900) at room temperature: 1:1 twice for 10 minutes each, 1:2 for 10 minutes, and 100% Araldite three times for 10 minutes each, then 100% Araldite overnight. The sample was flat embedded and polymerized at 60°C for 48 hours.

5.1.2 Serial section TEM

The sample block was detached from the coverslip by immersing the whole dish in liquid nitrogen, and then trimmed under stereoscope. The grid pattern imprinted in the resin served as landmarks. 70 nm serial ultrathin sections were cut using Leica UC6 ultramicrotome (Leica Microsystems Inc., Buffalo Grove, IL), collected on formvar coated slot grids, and stained with uranyl acetate and lead citrate. The top few sections containing the marker grid pattern were recognized under transmission electron microscope (Philips CM-12, FEI, Eindhoven, The Netherland) at lower magnification (170X), and were used to locate the regions of interest based on the comparison of neurites morphology from optical images. To identify regions of interest in deeper sections, the relative location of regions of interest on TEM sections was marked on the captured images (Gatan 4k×2.7k digital camera, Gatan Inc., Pleasanton, CA) and used as reference. Serial sections of neurites and synapses were then imaged at 170X - 66000X magnification.

5.1.3 Image processing

TEM images were processed with the FIJI plugin Enhance Local Contrast (CLAHE) (available through: http://imagej.net/Enhance_Local_Contrast_(CLAHE)) to enhance local contrast for visualization, with histogram bins 50. Optical images, AFM images, and TEM images of different magnifications and sections of the same area were aligned in Adobe Photoshop and visually inspected. In particular, due to the non-linear lens distortions induced by the electromagnetic lenses of TEM, serial section TEM images were usually distorted. In order to align TEM images with optical images and AFM images, I skewed the TEM images with shear transformation in Adobe Photoshop. For visualization purpose only, brightness and contrast was adjusted, median filter was applied, and pixel number was increased to smoothen the pixelated images in Adobe Photoshop.

5.2 Results and Discussion

In Chapter 4, I used fluorescence microscopy and synaptic markers to identify synapses. In particular, Synapsin-1 labels presynaptic vesicles, FM 4-64 labels endocytosed vesicles at functional axon terminals, and PSD-95 labels postsynaptic density. However, conventional optical microscopy does not provide high resolution imaging of complex synaptic structure or the localization of target proteins, making it difficult to distinguish between pre- and postsynaptic terminals.

In order to distinguish between pre- and postsynapses at high resolution and to investigate whether they are mechanically distinct, I performed transmission electron microscopy (TEM) imaging after TH-AFM.

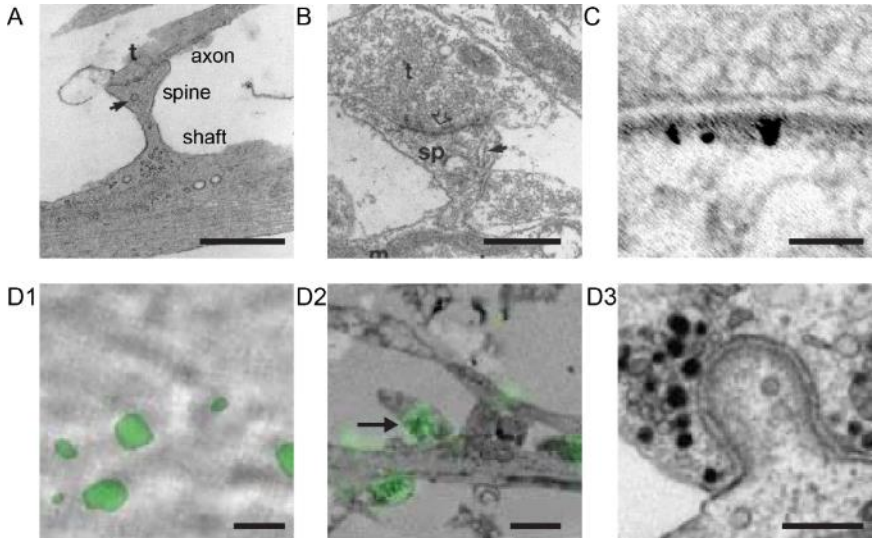

Figure 5-2 Applications of TEM in the study of synaptic ultrastructure.
TEM images in primary hippocampal neuron cultures. (A) A TEM image of 3-4-week-old neurons. The dendritic shafts are filled with microtubules, while the spines contain no microtubules and are filled with a fluffy and flocculent material. A mushroom-shaped spine with a thin neck forms a synapse with an axon terminal (t). (B) High magnification TEM image shows a large asymmetric synapse (open arrow) with a mushroom-shaped spine (sp). (C) Distribution of immuno-golds against PDZ1 domain of PSD-95 in 3-week hippocampal culture. (D1) Brightfield and FM dye fluorescence (green) overlay and (D2) TEM and FM dye fluorescence (green) overlay of the same region. (D3) High magnification TEM image of the synapse pointed by the arrow in D2. FM dye labeled vesicles appear with a dark lumen arising from photoconversion. Scale bar: A, 1 μm; B, 0.5 μm; C, 0.1 μm; D, E, 1 μm; F, 0.2 μm. Images are reprinted and adapted with permission from: A, B, (Papa et al., 1995), © 1995 Society for Neuroscience; C, (X. B. Chen et al., 2011), © 2011 Society for Neuroscience; D1, D2, D3, (Darcy et al., 2006), © 2006 Nature Publishing Group.

TEM was invented in 1931 by Max Knoll and Ernst Ruska who was awarded the Nobel Prize in physics in 1986 for this development (Ruska, 1987). TEM uses a beam of electrons transmitted

through a specimen which is usually an ultrathin (50 - 100 nm) cross-section of samples on a grid. An image is formed from the interaction between the electron and the sample. TEM is capable of visualizing samples at much higher resolution (at Angstrom level) than optical microscopy thanks to the smaller wavelength of electrons.

Such high resolution enables TEM to be used in the detailed characterization of synaptic ultrastructure (Bartlett & Banker, 1984; Boyer et al., 1998; Papa et al., 1995). To visualize cellular structures, in TEM sample preparation (see 5.1.1 for the sample preparation method), osmium is used to stain membranes by embedding its heavy metal directly into cell membranes and creating a high electron scattering rate. Membranes are thus sharply revealed in negative contrast and protein-rich compartments are densely stained. Glutamatergic excitatory synapses with their highly specialized synaptic membranes are clearly recognizable with their asymmetric structures (Figure 5-2 A, B). The postsynaptic membrane with postsynaptic density is thickening and appears denser than the presynaptic side. The presynaptic terminal contains round and electron-lucent synaptic vesicles. Dendrites are usually thicker and have a more electron-lucent cytoplasm, while axons are long and thin structures with microtubules as their principal constituent. Some synapses consist of spine heads that receive from one or more presynaptic terminals, while others are formed between presynaptic terminals and dendritic shafts without spine structures.

Combination of fluorescence imaging and TEM has been used to understand the complex neuronal and synaptic structure and function (Figure 5-2 D1, D2, D3) (Begemann & Galic, 2016). Darcy et al. combined FM dye labeling and TEM to study vesicle release at synapse in cultured neurons (Darcy et al., 2006). Bock et al. combined *in vivo* fluorescence imaging and TEM to study the network anatomy and physiology in the visual cortex (Bock et al., 2011). To my knowledge, no correlative AFM stiffness mapping and TEM imaging in neurons has been reported.

To locate the same synapses under TEM after TH-AFM imaging, neurons were cultured in

homemade glass bottom dishes with photoetched gridded coverslips (Figure 5-3). The pattern was recognizable under optical microscope (Figure 5-4 A) and was imprinted in the resin block during TEM sample preparation. The imprinted pattern was recognizable under stereoscope and low magnification TEM, and was used to find the grid of interest.

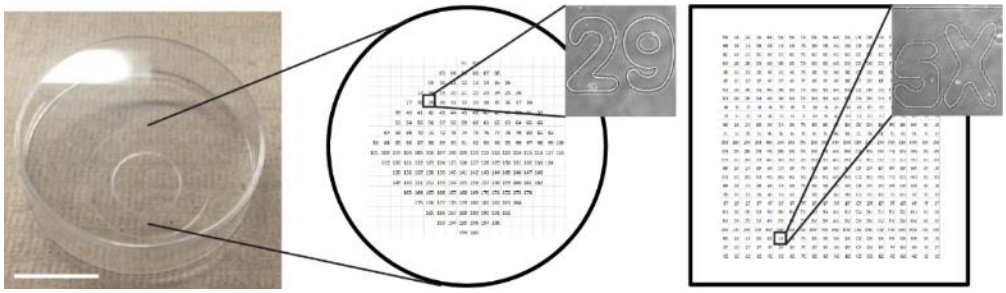

Figure 5-3 A homemade glass bottom dish with a gridded coverslip.
A 60 mm petri dish with a gridded coverslip attached to the bottom was used for neuron cultures. Schematic diagrams of two types of gridded coverslips used in the experiment: numeric and alphanumeric pattern. Phase contrast images of pattern "29" and "5X" are shown here as examples. Scale bar: 2 cm.

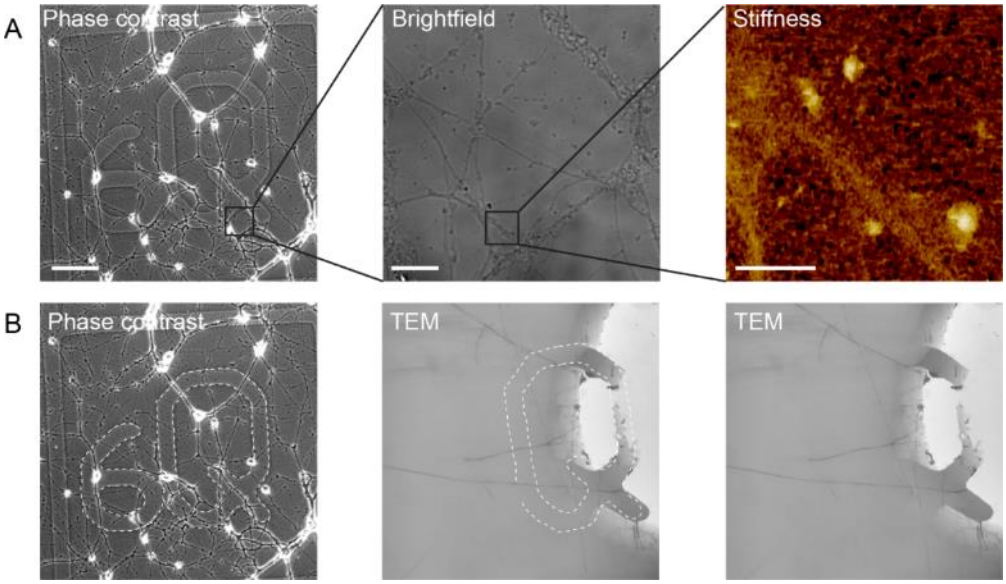

Figure 5-4 Correlative TH-AFM/TEM imaging.
(A) Alphanumeric pattern "6Q" was recognized under optical microscope in neuron cultures. TH-AFM stiffness image of the boxed area in the high magnification optical image is shown. Scale bar: phase contrast 100 μm, brightfield 10 μm, AFM stiffness 2 μm. (B) The grid pattern observed in the phase contrast image and later imprinted in the resin served as landmarks. Marked dashed lines show the pattern "6Q". The marker grid pattern was recognized in the top TEM section at lower magnification, and was used to locate the regions of interest based on the comparison of neurites morphology from optical images. Note that only part of "Q" was visible in the TEM image possibly due to the cutting angle in serial section TEM sample preparation.

Sections were collected on formvar coated slot grids. The top few sections usually contained the numeric pattern (Figure 5-4 B). I used the pattern as landmarks to locate areas of interest and relied on neurites morphology to align TEM images with optical and AFM images (Reddick & Alto, 2012).

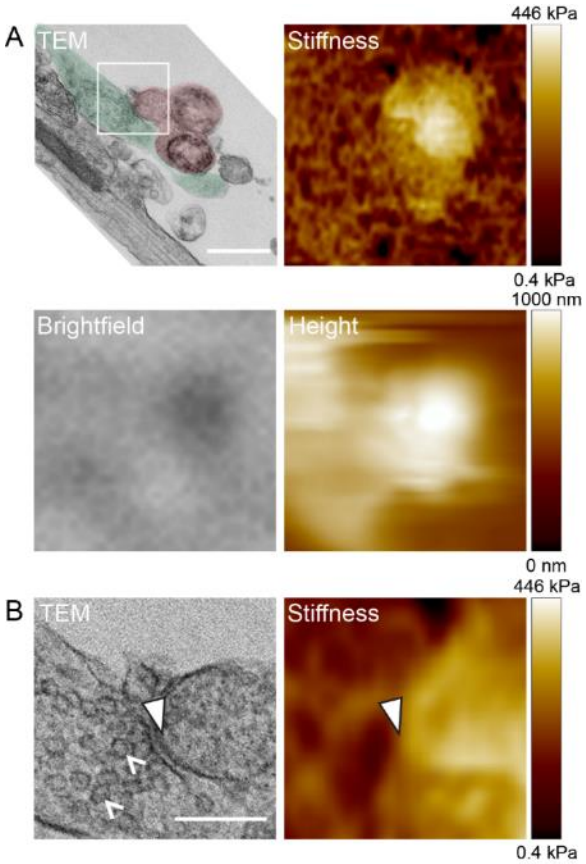

Figure 5-5 Correlative TH-AFM/TEM imaging of stiff synapses.
(A) Aligned TEM, AFM stiffness, brightfield, and AFM height images of the same synapse. I used the numeric pattern on photoetched coverslips as landmarks to align TEM images with optical and AFM images. In the TEM image, the bouton is shaded in green and the spine is shaded in red. High stiffness in the AFM stiffness image overlapped mostly with the spine head (209 kPa), while the bouton and dendritic shaft showed lower stiffness. The stiff spine displayed distinct contrast in the brightfield image and topographical feature in the AFM height image. Scale bar: 500 nm. (B) Zoomed-in TEM and AFM stiffness image of the boxed area shown in the TEM image in (A) illustrates the synaptic cleft. Scale bar: 200 nm. White arrowheads point to the postsynaptic density. White carets point to presynaptic vesicles.

Aligned TEM/AFM images showed that stiff structures were featured with presynaptic vesicles, postsynaptic density, and synaptic cleft (Figure 5-5 and Figure 5-6). In particular, spines, rather than boutons, overlapped with high stiffness pixels. These results conclude that the high stiffness observed under TH-AFM originated from postsynaptic spines and that postsynaptic spines

were mechanically different from presynaptic boutons.

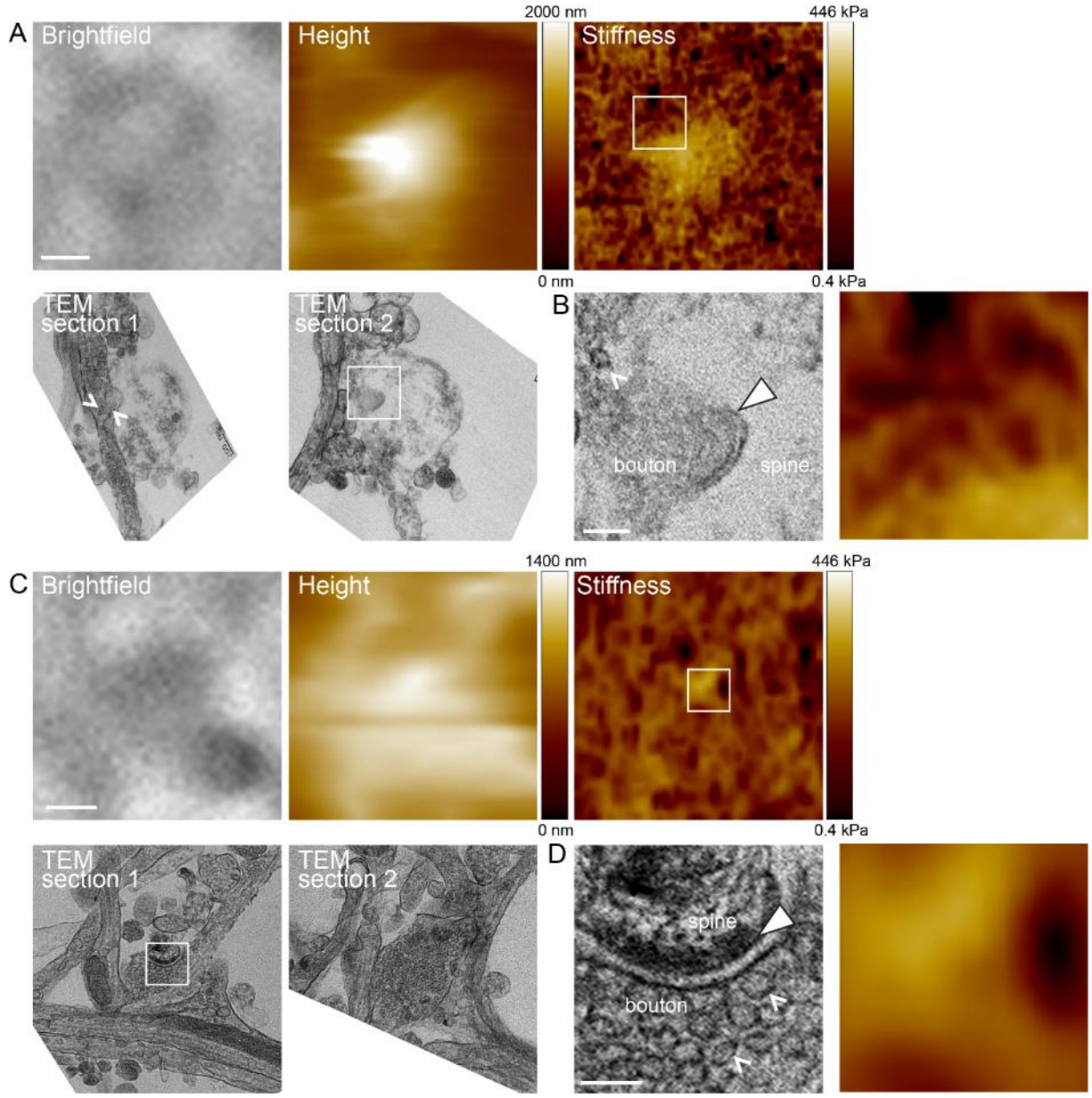

Figure 5-6 Examples of correlative TH-AFM/TEM images of synapses.
(A) Aligned brightfield, AFM height, AFM stiffness, and serial section TEM images of the same synapse. The bouton containing vesicles appeared in TEM section 1, and the spine head with postsynaptic density appeared in TEM section 2. (B) Zoomed-in TEM image and stiffness image from the boxed areas in the TEM section 2 and AFM stiffness images in (A). Elastic modulus values of the spine and shaft are 53 kPa and 11 kPa, respectively. Note high stiffness overlaid with the bottom half of the spine head, while the top half of the spine head did not show topographical features and was likely covered by compliant structures. (C) A bouton containing vesicles formed a synapse with a spine head. Elastic modulus values of the spine and shaft are 26 kPa and 8 kPa, respectively. (D) Zoomed-in TEM image and stiffness image from the boxed areas in the TEM section 1 and AFM stiffness images in (C). White arrowheads point to the postsynaptic density. White carets point to presynaptic vesicles. Scale bar A, C: 500 nm, B, D: 100 nm.

So far, I have used correlative TH-AFM/fluorescence imaging and correlative TH-AFM/TEM imaging to characterize stiff synapses in cultured hippocampal neurons. It would be ideal if we can combine all three imaging methods (AFM-fluorescence-TEM) to visualize the same synapse. However, it is technically difficult to combine immunofluorescence with TEM. During immunocytochemistry, cells are fixed and permeabilized so that antibodies can get into cells and bind to intracellular target proteins (4.1.1). To recognize synapses under TEM, we need to rely on presynaptic membranous vesicles and postsynaptic density. Fixation via protein cross-linking and membrane permeabilization during immunocytochemistry could cause structural artifacts and sample disruption (A. Burette, Collman, Micheva, Smith, & Weinberg, 2015; A. C. Burette et al., 2012), making it difficult to visualize synapses under TEM.

Other approaches might provide a potential combination of all three imaging methods. First, alternative fluorescence approach using genetically encoded fluorescence tags such as GFP labeled PSD-95 allows the visualization of synaptic markers directly without immunocytochemistry. However, overexpression of exogenous synaptic proteins such as PSD-95 could affect synaptic development and function (El-Husseini et al., 2000), making the observed results hard to interpret. Compounded with the difficulty and low efficiency in transfecting primary neuron cultures (Karra & Dahm, 2010), I did not use this approach. Second, alternative TEM approach using immuno-gold labeling to recognize target proteins allows direct identification of synaptic markers without fluorescence imaging. Chen et al. used immuno-gold labeling to visualize the location of PSD-95 (Figure 5-2 C)(X. B. Chen et al., 2011). However, the resolution is affected by the size the gold particles in the range of 10 - 20 nm (Griffiths et al., 1993), which may mask the ultrastructure environment of the target. In addition, immuno-gold also requires membrane permeabilization similar to immunofluorescence imaging, which could affect the image quality of membrane ultrastructure. Since the current approach already confirmed that high stiffness came from spines, I did not use immuno-gold TEM. Third, although

serial section TEM reveals ultrastructure of synapses, the aligning and reconstruction is extremely time-consuming and technically demanding. Another electron microscopy technique, focused ion beam/scanning electron microscopy (FIB-SEM), allows efficient and automatic 3D reconstruction of identified dendrites and synapses in hippocampal slices (C. Bosch et al., 2015). I have tried to image the samples with FIB-SEM and found that the high electron scattering from the bright blank background in sparse neuron cultures made the image quality of synapses not sufficient to reveal synaptic ultrastructure. Therefore, I did not rely on FIB-SEM to visualize synapses.

Next in Chapter 6, I will perform detailed quantitative analysis of spine stiffness.

Chapter 6 Spines are substantially stiffer than shafts

Not all spines are created equal. Spines vary in their morphology, molecular organization, calcium compartmentalization, and strength, creating a broad spectrum of input-specific structural and functional plasticity. Does spine stiffness also display such heterogeneity? How is spine stiffness related to spine morphology? Would spine stiffness give us some insights into synaptic function?

In this Chapter, I will delve deeper into the data and analyze spine stiffness quantitatively.

6.1 Methods

6.1.1 Data analysis

For apparent spine size measurement, a median filter was applied to the AFM stiffness image. Substrate signal was measured by selecting a substrate region in the image and plotting a Gaussian distribution histogram showing mean μ and standard deviation σ. The threshold was then set as $\mu + 3\sigma$ to identify areas of interest for area measurement.

Error bars in all figures represented standard error of mean. Statistic comparisons were done using two-tailed t tests. Sample size (n), p value, and Pearson correlation coefficient (r) were given in figure legends when applicable. Each neuron culture represented an independent experiment. A significance level of 0.01 was used in hypothesis tests and $p < 0.01$ was considered significant.

To fit the transformed data to a normal distribution, the maximum likelihood estimation method was used. Goodness of fit tests of the transformed data in a normal distribution were performed using two-tailed Kolmogorov-Smirnov tests with the null hypothesis that the transformed data is normally distributed. I tested goodness of fit for different transformations including logarithm, square root, and cubic root, as well as for non-transformed data (Table 6-1). Given that for spine stiffness (kPa), shaft stiffness (kPa), spine size (μm^2), logarithm transformation has the highest p value (the probability of the null hypothesis being true), the data is likely to follow a lognormal-like distribution.

All data were analyzed using Python.

	spine stiffness (kPa)	**shaft stiffness (kPa)**	**spine size (μm^2)**
non-transformed	2.01E-05	2.45E-05	0.0001
logarithm	0.3192	0.2446	0.9486
square root	0.0231	0.0061	0.0941
cubic root	0.1609	0.0233	0.4158

Table 6-1 p values for two-tailed Kolmogorov-Smirnov tests of transformed data.

6.1.2 Contact mechanics model used in stiffness calculation

Elastic modulus was calculated by fitting the AFM force-distance curves using a Derjaguin-Muller-Toporov (DMT) model (Derjaguin et al., 1994) with a hemispherical indenter as previous described (Sahin & Erina, 2008) (Figure 6-1 A). The interaction force during AFM indentation is written as the following:

$$F = F_{adh} + \frac{4}{3}E^*\sqrt{R^*}d^{\frac{3}{2}} \quad (1)$$

F denotes the tip-sample interaction force. F_{adh} denotes a constant adhesion force measured by the peak negative force during AFM retraction. E^* denotes the effective elastic modulus. d denotes the indentation depth. R^* denotes the effective radius:

$$\frac{1}{R^*} = \frac{1}{R_{tip}} + \frac{1}{R_{sample}} \quad (2)$$

R_{tip} is the tip radius, and R_{sample} is the sample radius. Because R_{sample} (spine and shaft radius) is relatively large compared to R_{tip}, R_{sample} was neglected in the stiffness calculation in Figure 6-3 for 409 spines and shafts.

6.1.3 Sensitivity of spine stiffness/spine size correlation to contact mechanics models

The results in Figure 6-5 showed spine stiffness was correlated with spine size. It is important to consider whether such correlation is introduced because the calculation of E^* depends on spine radius R_{sample} (Equation (1), (2)). In order to analyze the correlation between spine stiffness $E^*$and spine size R_{sample}, I first took into consideration R_{sample} to calculate E^*in the DMT model (Equation (1), (2)). To estimate R_{sample}, I first measured the apparent spine size from AFM stiffness images by thresholding the stiffness signal to identify region of interest for area measurement. I used area, S, to represent the apparent spine size in Figure 6-4 and Figure 6-5. Assuming the measured area is a round flat surface, I estimated sample radius from $S = \pi {R_{sample}}^2$. I used the DMT model with

R_{sample} in the stiffness calculation in Figure 6-5. Inclusion of R_{sample} in the DMT model slightly increases measured spine stiffness, suggesting that the stiffness calculation in Figure 6-3 may be an underestimate of sample stiffness.

When the AFM tip exerts force onto the spine head, the forces are transmitted to the spine head – substrate interface. Deformations of the spine head at this interface during interactions with AFM tip could also affect stiffness measurements. Because spine diameters are large compared to the AFM tip, neglecting the spine-substrate interface in the DMT model is a plausible assumption. Furthermore, presence of adhesive forces between the substrate and the spine head would increase the apparent stiffness of this interface. However, it is still possible to make a worst-case estimate of the contributions from the spine-substrate interface by assuming that there are no adhesive forces at this interface and the spine head is making a sphere-plane contact with the substrate.

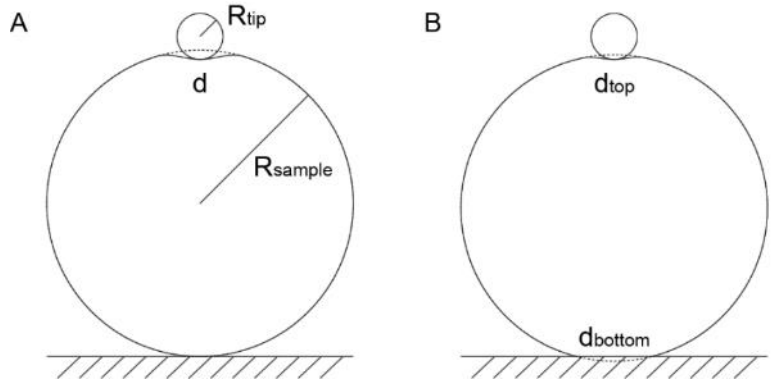

Figure 6-1 Contact mechanics models.
Schematic diagrams illustrate models when indentation (d) only occurs at the top surface between the AFM tip with radius R_{tip} and the sample with radius R_{sample} (A) or at both the top surface and the bottom surface between the sample and the substrate (B).

I carried out this worst-case analysis by considering indentations on both surfaces: $d = d_{top} + d_{bottom}$. d_{top} is the indentation depth on the top surface of the sample, and d_{bottom} is the indentation depth on the bottom of the sample close to the substrate (Figure 6-1 B). In the DMT model used in Figure 6-3, I assumed the indentation between the bottom of the sample (spine head) and the substrate is trivial and thus used $d = d_{top}$. Here, to account for both d_{top} and d_{bottom} to

make an worst-case estimate of elastic modulus considering sample geometry, I adapted the "sphere between two parallel planes" model (Puttock & Thwaite, 1969). Given F is the same on both surfaces, we could write $F = \frac{4}{3}E^*\sqrt{R^*_{top}}{d_{top}}^{\frac{3}{2}}$, and $F = \frac{4}{3}E^*\sqrt{R^*_{bottom}}\,{d_{bottom}}^{\frac{3}{2}}$, thus

$$\frac{d_{bottom}}{d_{top}} = \sqrt[3]{\frac{R^*_{top}}{R^*_{bottom}}} \tag{3}$$

From Equation (2), we could get $R^*_{bottom} = R_{sample}$, and $R^*_{top} = \frac{R_{tip} \times R_{sample}}{R_{tip} + R_{sample}}$. Thus Equation (3) can be written as:

$$\frac{d_{bottom}}{d_{top}} = \frac{1}{\sqrt[3]{1+\frac{R_{sample}}{R_{tip}}}} \tag{4}$$

From Equation (1), the worst-case elastic modulus E^*_2 can be written as $F = \frac{4}{3}E^*_2\sqrt{R^*_{top}}{d_{top}}^{\frac{3}{2}}$ while the DMT model $E^*$is written as $F = \frac{4}{3}E^*\sqrt{R^*_{top}}(d_{top} + d_{bottom})^{\frac{3}{2}}$. We could then derive E^*_2 as following:

$$E^*_2 = E^* \times \left(1 + \frac{1}{\sqrt[3]{1+\frac{R_{sample}}{R_{tip}}}}\right)^{\frac{3}{2}} \tag{5}$$

Using this worst-case E^*_2 which accounts for sample geometry R_{sample} and sample-substrate interaction, I performed correlation analysis, and revealed that the worst-case E^*_2 is still correlated with spine size with r = 0.2595 and p = 2.461E-03. In the DMT model with R_{sample} (spine radius) taken into account, E^* is correlated with spine size with r = 0.3837 and p = 4.719E-06 (model in Figure 6-4 and Figure 6-5). In the DMT model without R_{sample} (spine radius) taken into account (i.e. assuming $R_{sample} \gg R_{tip}$), E^* is correlated with spine size with r = 0.4384 and p = 1.174E-07 (model in Figure 6-3). In all three models, spine stiffness is correlated with spine size.

6.2 Results and Discussion

Spines form the postsynaptic components of most excitatory synapses (Boyer et al., 1998; Niesmann et al., 2011), and their structural and functional plasticity is critical for learning and memory (A. Holtmaat & Svoboda, 2009). A spine usually consists of an enlarged head (1-2 μm in diameter) and is connected to the dendritic shaft by a thin neck (200 nm in diameter, and 0.5 to several μm in length) (Figure 6-2). The unique morphology of spines is thought to play a role in synaptic function, allowing for the biochemical compartmentalization (Yasuda et al., 2006) and electrical compartmentalization (Tsay & Yuste, 2004). Spine morphological features including spine head size, neck width, and neck length, fall into a wide range (Peters & Kaiserman-Abramof, 1970), and can be largely stable over hours (Tonnesen et al., 2014). During synaptic plasticity, spine heads become larger (Honkura, Matsuzaki, Noguchi, Ellis-Davies, & Kasai, 2008; Matsuzaki, Honkura, Ellis-Davies, & Kasai, 2004; Okamoto, Nagai, Miyawaki, & Hayashi, 2004; Zhou, Homma, & Poo, 2004), and spine necks become wider and shorter revealed by super-resolution microscopy (Tonnesen et al., 2014). Such morphological heterogeneity provides functional diversity for synapses, enabling input-specific plasticity and maximizing neuron connectivity (Rafael Yuste, 2010).

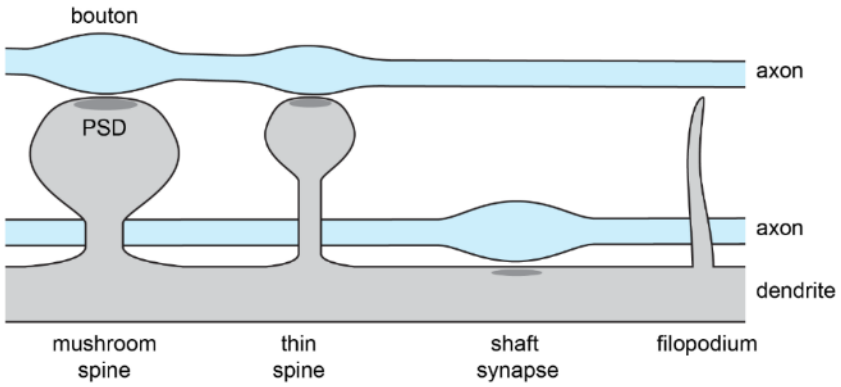

Figure 6-2 Spine morphological heterogeneity.
A schematic diagram of morphologies of spines and filopodia. Note that some synapses are formed directly on the shaft without spine structures.

In this work, I define postsynaptic protrusions with synaptic contacts as spines, and those without synaptic contacts as filopodia. The definition of spines I used is based on synaptic markers

and ultrastructure under electron microscopy, rather than spine morphology as used previously (Peters & Kaiserman-Abramof, 1970). This is because morphological features can be ambiguous and do not allow for clear distinction between filopodia and so-called immature spines.

6.2.1 Spines are on average 10 times stiffer than shafts

Intriguingly, the stiffness of spines fell within a wide range. The stiffness of shafts, on the contrary, was constantly low (Figure 6-3 A). Spines were on average 10 times stiffer than nearby shafts. The minimum, maximum, median, and mean elastic modulus values of spines are 23.2 kPa, 671.9 kPa, 166.9 kPa and 201.3 kPa, whereas the minimum, maximum, median, and mean elastic modulus values of shafts are 7.1 kPa, 67.4 kPa, 20.7 kPa and 23.6 kPa (see 3.1.4 for quantitative stiffness measurement of areas of interest).

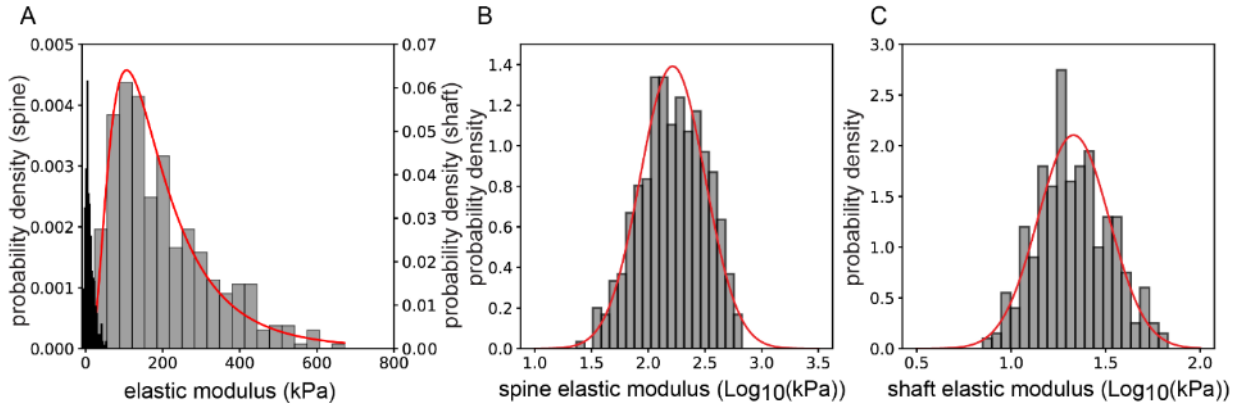

Figure 6-3 Distribution of spine stiffness and shaft stiffness.
(A) Histogram of elastic modulus of spines (grey) and nearby shafts (black) with bins = 20. n = 409 spines / 30 neuron cultures. I fitted the logarithm data with a normal distribution in (B)(C). Spine stiffness fitted curve (lognormal) is shown in red in (A). The mean elastic modulus values of spines and shafts from the fitting are 164.3 kPa and 21.4 kPa, respectively. I tested the goodness of fit using Kolmogorov-Smirnov tests (p_{spine} = 0.3192, p_{shaft} = 0.2446).

The distributions of spine and shaft stiffness were strongly skewed with heavy tails and exhibited the characteristics of a lognormal distribution (Figure 6-3). The fitted mean elastic modulus values of log-scaled spines and shafts are 164.3 kPa and 21.4 kPa, respectively. It has been reported that many physiological features of the brain, such as neuronal firing rate and synaptic strength, have lognormal-like distributions, which may help establish reliable and unique information encoding

(Buzsaki & Mizuseki, 2014).

Among the 409 spines/shafts measurements in Figure 6-3, 263 spines were confirmed with immunocytochemistry as described in Chapter 4. In my experiment, I first confirmed that all 263 stiff spines revealed by TH-AFM were co-labeled with both synaptic markers. Then in the subsequent AFM experiment, I did not stain neurons anymore because the conclusion that stiff synapse-like structures are spines is already validated. See for the comparison in Table 6-2 and Table 6-3 between 263 spines that have been confirmed with immunocytochemistry and the remaining 146 spines without immunocytochemistry. The stiffness of spines without immunocytochemistry is on the similar range and scale as spines with immunocytochemistry.

	all spines	**with immunocytochemistry**	**without immunocytochemistry**
count	409	263	146
mean (kPa)	201.35	176.65	245.84
std (kPa)	127.01	113.85	137.38
min (kPa)	23.21	23.21	34.96
25% (kPa)	105.70	94.88	141.35
50% (kPa)	166.90	141.80	202.62
75% (kPa)	273.97	243.04	355.93
max (kPa)	671.95	574.72	671.95
lognormal mean (kPa)	164.28	144.42	207.20

Table 6-2 Spine stiffness comparison

	all spines	**with immunocytochemistry**	**without immunocytochemistry**
count	409	263	146
mean (kPa)	23.57	24.95	21.08
std (kPa)	10.99	10.95	10.65
min (kPa)	7.08	10.11	7.08
25% (kPa)	15.67	17.15	12.29
50% (kPa)	20.67	22.05	18.39
75% (kPa)	28.65	30.75	27.07
max (kPa)	67.44	67.44	59.13
lognormal mean (kPa)	21.38	22.98	18.78

Table 6-3 Shaft stiffness comparison

I measured the apparent spine size from AFM stiffness images by thresholding the stiffness signal to identify regions of interest for area measurement (see 6.1.1 for quantitative area

measurement). I found that the distribution of apparent spine size was also skewed with a heavy tail with a mean size of 0.23 μm^2 (Figure 6-4).

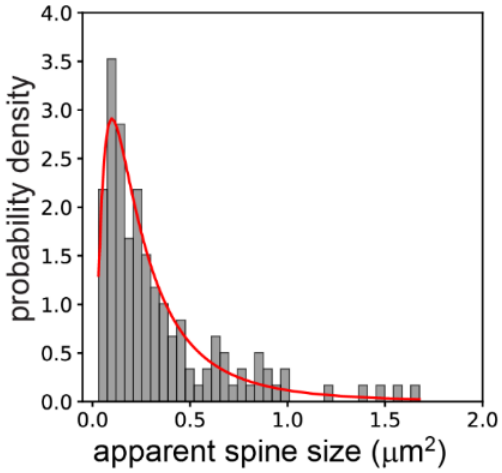

Figure 6-4 Distribution of apparent spine size.
Histogram of the apparent spine size measured from AFM stiffness images with bins = 37. n = 134 spines / 20 neuron cultures. I fitted the logarithm data with a normal distribution (red fitted curve with a mean spine size of 0.23 μm^2.) and tested the goodness of fit using a Kolmogorov-Smirnov test (p = 0.9486).

More interestingly, I found that spine stiffness measurements were positively correlated with the apparent spine size (Figure 6-5) (see 6.1.3 for additional discussion about correlation analysis), suggesting that larger spines may have underlying changes in intracellular cytoskeleton architecture (M. Bosch et al., 2014).

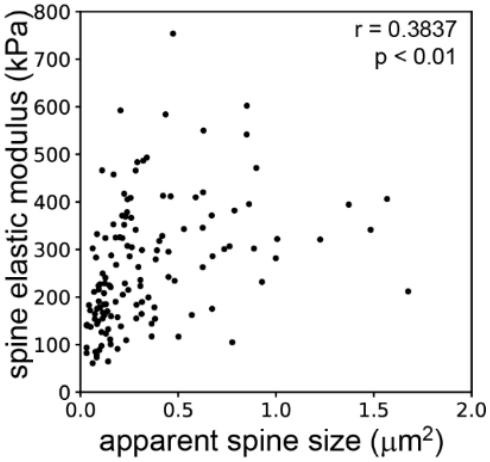

Figure 6-5 Spine stiffness is correlated with spine size.
Correlation of spine elastic modulus with apparent spine size from Figure 6-4. n = 134 spines / 20 neuron cultures. r: Pearson correlation coefficient. p: significance of correlation with a two-tailed t test. p = 4.719E-06.

The criteria used for synapse-like structures under TH-AFM discussed in 3.2 might exclude spiny synapses with a stiffness below 20 kPa or without distinct height features in topographical images (for example, spines buried underneath neurites), and shaft synapses that are formed directly on the shaft without protrusive spine structures. Nevertheless, given that the measured spine stiffness had a lognormal-like distribution with a peak around 164 kPa, very few spines would be excluded by these criteria.

In this work, I did not track the dynamic changes of spine stiffness and spine size, and did not investigate how a single spine changes over time. Instead, the current results were a snapshot of spines at the population level. It has been reported that at the population level, spine size is correlated with synaptic strength (Matsuzaki et al., 2001). The relationship between spine stiffness and spine size could be interpreted both at the population level and at the individual spine level. At the population level, spines are largely heterogeneous with different morphological features, sizes, functional strength, and dynamic motility (R. Yuste & Bonhoeffer, 2004), as well as internal actin architecture. Thus, there could be innate stiffness heterogeneity among different spines irrelevant to spine size, which could explain why only 40% of spine stiffness changes can be explained by spine size ($r = 0.3837$). At the individual spine level, spines can increase their sizes after long-term potentiation, also referred to as structural plasticity, and get functionally potentiated (Hering & Sheng, 2001). During such spine enlargement, actin undergoes remodeling and increased cross-linking (Honkura et al., 2008; Matsuzaki et al., 2004; Okamoto et al., 2004; Zhou et al., 2004), which would enhance spine stiffness, resulting in a positive correlation between spine size and spine stiffness. Therefore, the current observation is likely a mixture of both individual spine changes and population heterogeneity. To distinguish between these two, it is worth investigating how a single spine changes its size and stiffness after stimulation in the future.

6.2.2 Shaft synapses do not display high stiffness

I have shown that high stiffness originated from spines. It is then interesting to study whether excitatory synapses without spines are also stiff. Previous research showed that 50% of excitatory synapses in hippocampal neurons are formed on the shaft without protrusive spine structures both in *in vitro* neuron cultures and in brain slices (Boyer et al., 1998; Niesmann et al., 2011). The ratio of shaft synapses to spiny synapses decreases in older cultures and adult animals (Fiala, Feinberg, Popov, & Harris, 1998). It remains unclear whether new spines grow from previously existing shaft synapses (R. Yuste & Bonhoeffer, 2004) or from filopodia which initiate synaptic contacts with nearby axons (Ziv & Smith, 1996), and it is also unclear whether shaft synapses are converted from pruned spiny synapses (Ovtscharoff et al., 2008) or originate with a different mechanism. In addition, it is not clear whether shaft synapses are functionally different from spiny synapses. Recently, Xu et al. used super-resolution microscopy stochastic optical reconstruction microscopy (STORM) to image receptor organization in cultured hippocampal neurons and showed that shaft synapses and spiny synapses consist of different combinations of glutamate receptors and that shaft synapses are apparently silent (C. Xu, Liu, H., Qi, L., Hao, G., Shen, Z., Wang, Y., Babcock, H., Lau, P., Zhuang, X, Bi, G., 2017). Given their morphological and potentially functional differences, shaft synapses may be mechanically distinct from spiny synapses.

I first used correlative TH-AFM/fluorescence imaging to visualize potential shaft synapses. Colocalization of PSD-95 and Synapsin-1 puncta from immunofluorescence imaging revealed more mature synapses than TH-AFM. As shown in Figure 6-6 B, synapse 1 and 2 did not display high stiffness or distinct topographical features, nor were they recognizable in the brightfield images. These two synapses were very close to the dendritic shafts, and were likely to be shaft synapses.

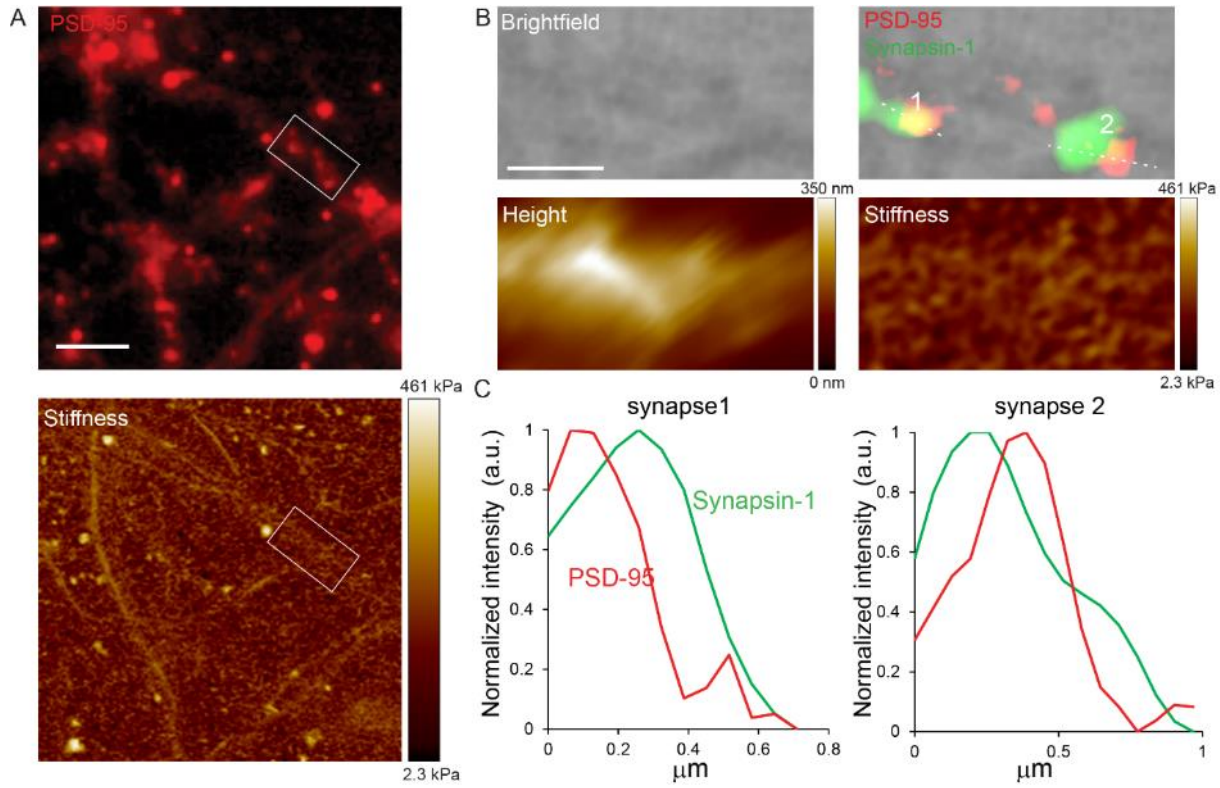

Figure 6-6 A subgroup of synapses identified by immunofluorescence microscopy do not show high stiffness.

(A) PSD-95 and stiffness image of the same area in cultured neurons. Scale bar: 3 μm. (B) Aligned brightfield, immunofluorescence, AFM height, and AFM stiffness images of the boxed area in (A). Synapses identified by the colocalization of PSD-95 and Synapsin-1 (marked as 1 and 2 in the overlaid brightfield/PSD-95/Synapsin-1 image) did not show recognizable height and stiffness features under TH-AFM and were very close to the shaft. Scale bar: 1 μm. (C) Fluorescence intensity profiles along the dashed lines over two synapses in B showed overlapping of PSD-95 (red) and Synapsin-1 (green).

To quantify the number of colocalized puncta, I used Caltracer (Figure 6-7 A) and set parameters such as fluorescence intensity, puncta size, and the threshold of overlapping percentage. I found that 32% of synapses identified by immunofluorescence displayed high stiffness under TH-AFM (Figure 6-7 B) and all synapse-like structures detected by TH-AFM using the criteria described in Chapter 3 displayed higher stiffness than nearby dendrites and axons.

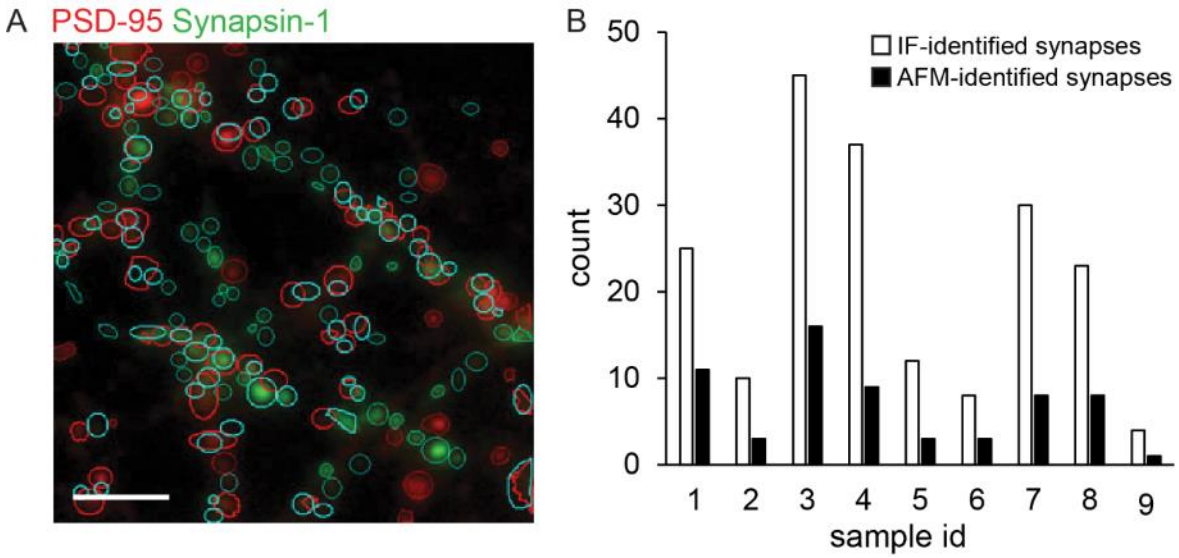

Figure 6-7 Colocalization detection with Caltracer.
(A) Caltracer was used to identify colocalized puncta (see 4.1.4 for methods used to quantify colocalized puncta). Only those within 2 μm of neurites and with a diameter 0.2 - 2 μm were considered as synapses. I used these criteria to quantify total number of immunofluorescence (IF)-identified synapses. Scale bar: A: 3 μm. (B) In 9 neuron cultures, IF identified 194 synapses of which 62 were also identified under TH-AFM.

Such inconsistence in synapse detection between AFM and immunofluorescence may be explained by the following reasons. First, optical immunofluorescence microscopy has a resolution limit of 200 nm. Although the analysis was done in a consistent manner, the fluorescence puncta in the optical images are likely to be larger than the actual synaptic structures, causing false positive results in colocalization detection. Second, AFM imaging requires a physical contact between the cantilever tip and the sample. Due to the very small force (300 pN) applied, it is possible that the cantilever loses contact with the sample during scanning. Such small forces plus low indentation distances limit the reach to synapses that are embedded underneath neurites of which I did not observe any topographical features nor mechanical ones. With such limitation in AFM measurements, not observing high stiffness under AFM does not necessarily mean those synapses identified by immunofluorescence were not stiff. Third, a subgroup of mature excitatory synapses are indeed not stiff, as the AFM images revealed. The imaging results showed that those synapses without high stiffness were usually undistinguishable in optical images and topographical images, and their immunostaining puncta were very close to the shafts, likely to be shaft synapses.

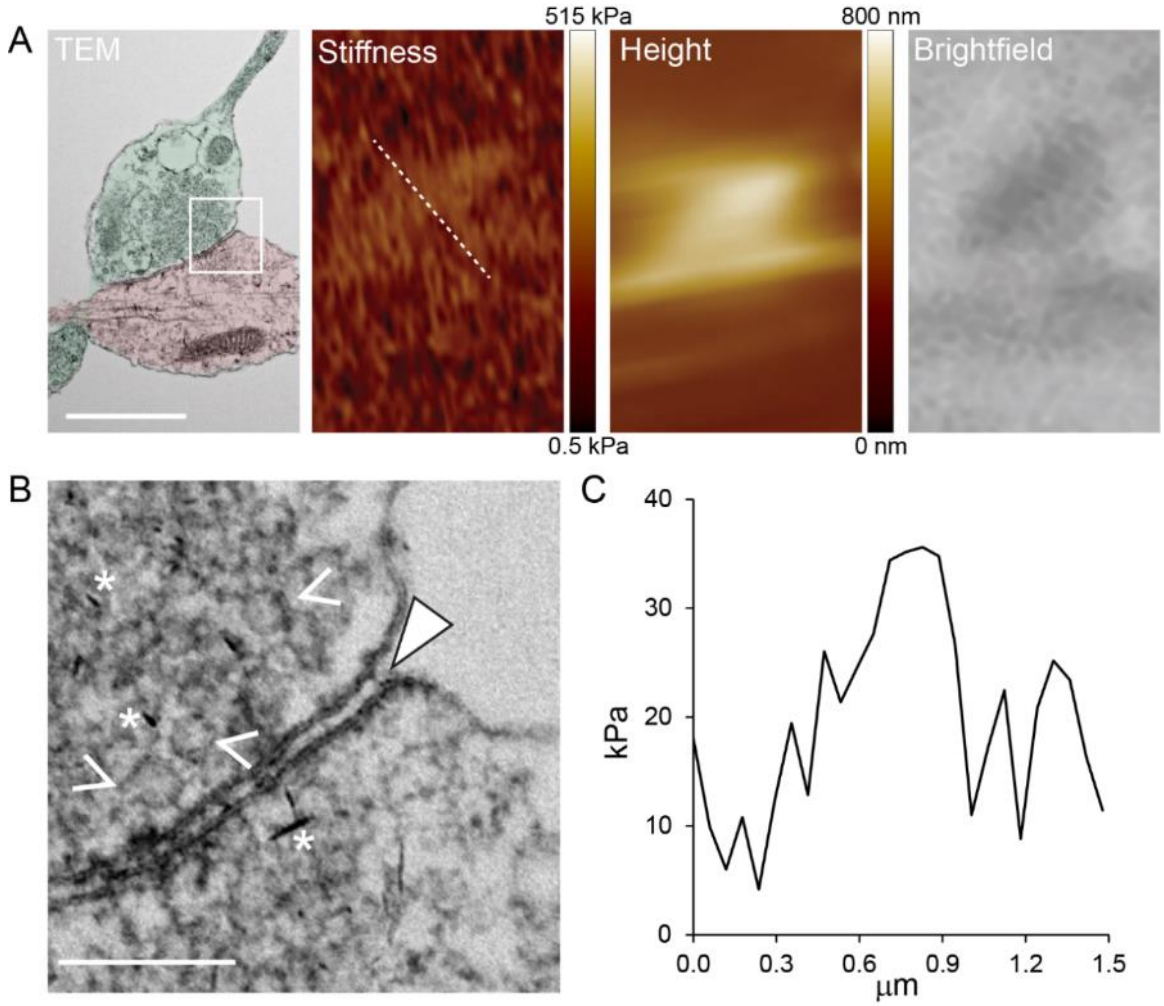

Figure 6-8 A shaft synapse does not display high stiffness.
(A) Aligned TEM, AFM stiffness, AFM height, and optical images of a shaft synapse. The bouton is shaded in green and the postsynapse is shaded in red. Scale bar: 1 µm. (B) Zoomed-in TEM image from the boxed area in the TEM image in (A) illustrates the synaptic cleft. White arrowheads point to the postsynaptic density. White carets point to presynaptic vesicles. Note there were some needle-like precipitations (white asterisks) from TEM sample preparation. Scale bar: 200 nm. (C) Elastic modulus profile along the dashed lines in the AFM stiffness image in (A) over the synapse. Note although this synapse had a low stiffness of 35.6 kPa, it was still distinguishable from the substrate.

In order to acquire the high resolution ultrastructure of shaft synapses and to distinguish shaft synapses from spiny synapses more accurately, I used TEM to visualize the ultrastructure of a synapse that was not stiff under TH-AFM as I did in Chapter 5. I found that the synapse that did not show high stiffness under TH-AFM was formed on the shaft (Figure 6-8), suggesting that shaft synapses could be mechanically different from protrusive synapses with spines.

6.2.3 Filopodia are not stiff

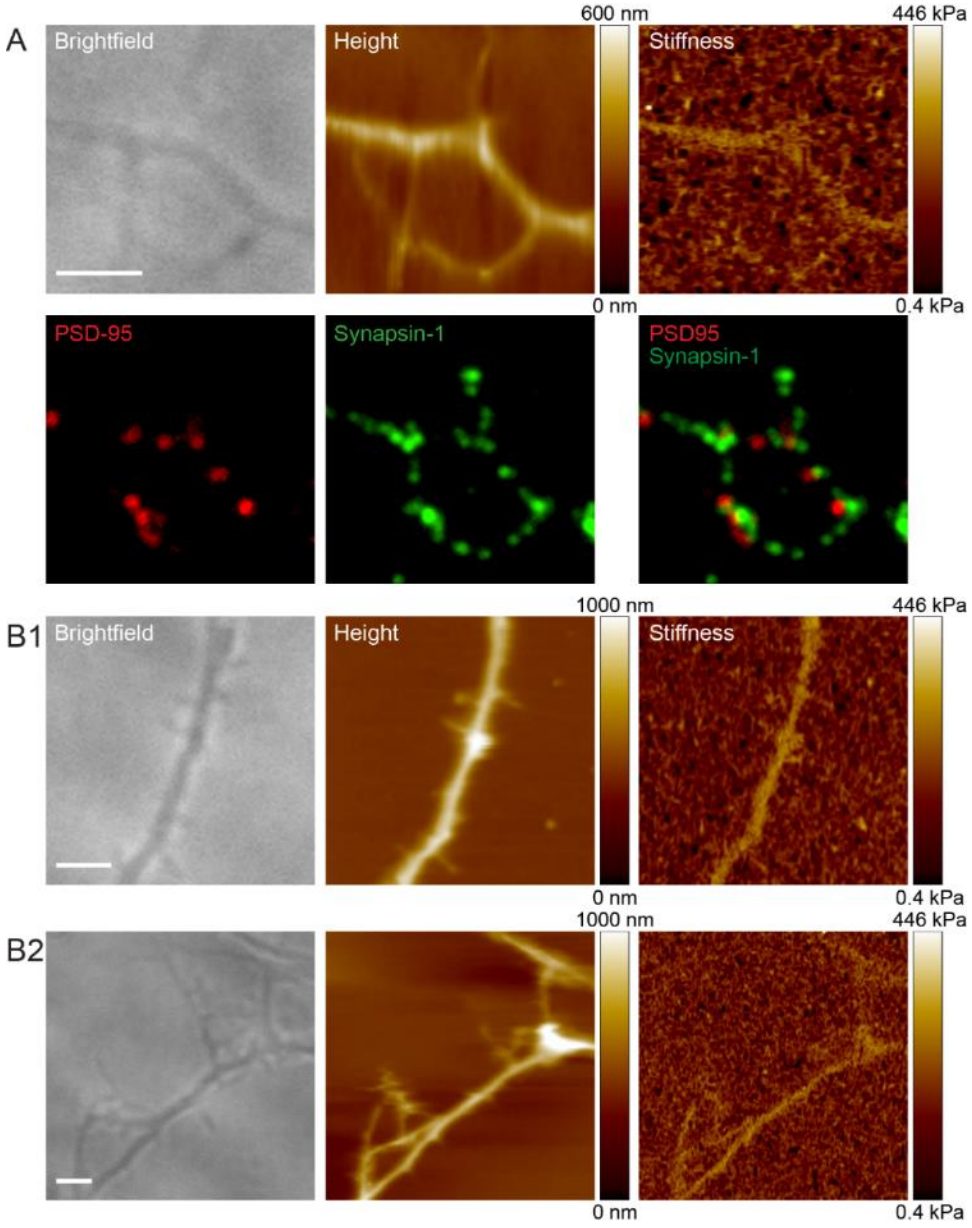

Figure 6-9 Immature protrusions are not stiff.
(A) Aligned brightfield, AFM height, AFM stiffness, and immunofluorescence images of neurons on DIV7. Note the thin protrusions were not highly stiff (14 kPa). (B1)(B2) Aligned brightfield, AFM height, and AFM stiffness images of neurons on DIV6. Elastic modulus values of these non-stiff protrusions are 18 kPa, 14 kPa respectively. Scale bar: 2 μm. See 3.1.4 for quantitative stiffness measurement of areas of interest.

In addition, I found that immature protrusions, likely filopodia, were not stiff under TH-AFM (Figure 6-9). Filopodia are likely to be the precursors of spines (R. Yuste & Bonhoeffer, 2004). As a spine matures, its morphology changes from a filopodium-like protrusion to a mushroom-shaped

structure with a knobby head and a thin neck, accompanied with actin remodeling (Korobova & Svitkina, 2010; Mattila & Lappalainen, 2008). These observations that mature spines were stiff and filopodia were not stiff suggest that spine stiffness may increase as spines mature. It is thus worth investigating in the future how a single spine changes its stiffness as it matures and how stiffness change is related to synaptic function and activity.

Next in Chapter 7, I will examine the potential source for spine stiffness.

Chapter 7 Spine stiffness and actin networks

Diamond is one of the stiffest materials on earth, and has high wear and chemical resistivity, which makes the slogan "A Diamond Is Forever" somewhat valid from a physical perspective. Valuable though a diamond can be, it is made of exactly the same material as soft graphite in a pencil at the atomic level: carbon. What crowns a diamond on an expensive engagement ring and what wraps graphite in an inexpensive pencil is the different arrangements of carbon atoms.

Similarly, cytoskeleton in stiff spines and soft shafts exhibits different arrangements. One particular type of cytoskeleton, F-actin, is enriched in spine heads and forms densely cross-linked networks. This special arrangement of F-actin may contribute to high spine stiffness.

In this Chapter, I will study how spine stiffness is related to actin networks.

7.1 Materials and Methods

7.1.1 Pharmacological treatments

Drugs used in this work were Latrunculin A (Sigma-Aldrich L5163) and (-)-Blebbistatin (EMD Millipore 203391). Drugs were first dissolved in DMSO (Sigma-Aldrich D2650) and used at different working concentrations: Latrunculin A (Lat A) 10 μM and Blebbistatin 100 μM. In time-lapse TH-AFM imaging, drugs were added to Tyrode's buffer at room temperature and AFM images were taken before and after the treatment. To compare the before and after long-term effect of Lat A, neurons were cultured in the same type of glass bottom dishes with gridded coverslips used in correlative TH-AFM/TEM imaging. Neurons were first imaged in Tyrode's buffer under TH-AFM for up to 2 hours. Neurons were then rinsed with sterile Tyrode's buffer and incubated with sterile culture medium containing Lat A in the incubator for 12-24 hours. TH-AFM imaging was performed again on the same spines after treatment in Tyrode's buffer containing Lat A. DMSO (less than 0.1 %) was used in randomly assigned control experiments. Neurons were fixed at the end of the experiment for immunocytochemistry.

7.1.2 Immunocytochemistry

To label F-actin, Alexa Fluor® 546 Phalloidin (1:500, Thermo Fisher Scientific A22283) was added to the secondary antibody solution in the standard immunocytochemistry as described in 4.1.1.

7.1.3 Statistical analysis

Error bars in all figures represented standard error of mean. Statistic comparisons were done using two-tailed t tests. Sample size (n), p value, and Pearson correlation coefficient (r) were given in figure legends when applicable. Each neuron culture represented an independent experiment.

7.2 Results and Discussion

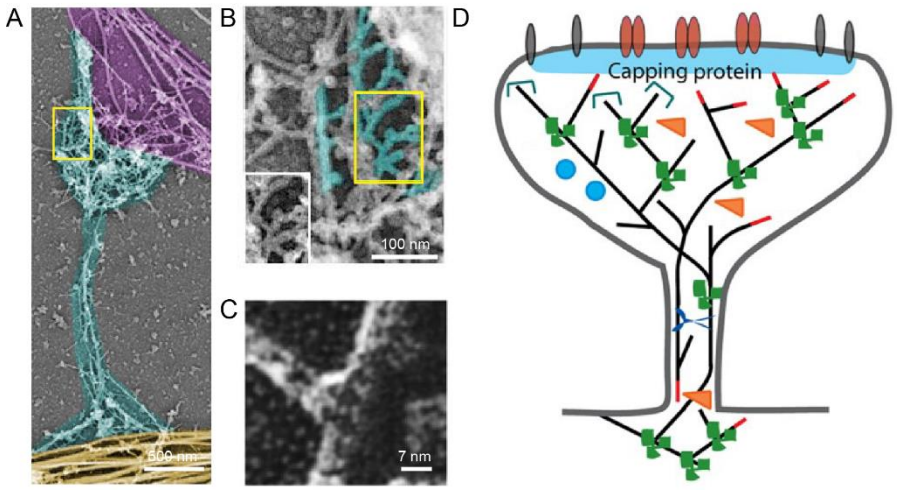

Figure 7-1 Spines contain dense actin networks regulated by actin binding proteins.
(A) Cytoskeletal organization of a synapse. Platinum replica electron microscopy of DIV 14 cultured neurons. A mushroom-shaped spine (cyan) is associated with a dendritic shaft (yellow) at the bottom and an axon (purple) at the top. Thick fibers in the axon and dendritic shaft represent microtubules. (B) Zoomed-in image of the yellow box in (A) shows branched actin networks (cyan) in the spine head. The inset shows the nonpseudocolored region outlined by yellow box. (C) Electron micrograph of quick-frozen, deep-etched, rotary-shadowed actin filament branches mediated by Arp2/3 complex. (D) A schematic diagram illustrating actin networks and actin biding proteins in a spine. G-actin (blue) polymerizes into F-actin (black lines). F-actin forms branched networks mediated by Arp2/3 (green). Cofilin (orange) depolymerizes pointed ends of F-actin. Actin barbed ends (red lines) are capped by capping proteins, the function of which is not yet clear. Images are reprinted and adapted with permission from: A, B, (Korobova & Svitkina, 2010), © 2010 Korobova et al; C, (Volkmann et al., 2001), © 2001 American Association for the Advancement of Science; D, (Hotulainen & Hoogenraad, 2010), © 2010 Hotulainen and Hoogenraad.

Cytoskeleton provides spatial organization, supports intracellular contents, and connects cells to the environment (extracellular matrix or other cells) both physically and biochemically, generating and sustaining forces in cell dynamics (D. A. Fletcher & Mullins, 2010). Neurons with their highly specialized morphology have a unique cytoskeleton organization. Axons and dendrites contain microtubules that serve as highways for intracellular traffic. Actin filaments (F-actin) form periodic ringlike structures in axons of hippocampal neurons (K. Xu, Zhong, & Zhuang, 2013), providing both flexibility and rigidity. Spines with their small and peculiar shapes have densely cross-linked F-actin as their main cytoskeleton (Figure 7-1 A, B). F-actin plays an important role in synaptic structure and function (Cingolani & Goda, 2008; Korobova & Svitkina, 2010), and actin dynamics is involved in synaptic plasticity (Okamoto et al., 2004; Peng et al., 2004; Zhou et al., 2004)

F-actin, the polymer form of globular actin monomer (G-actin), is polar. The barbed end grows faster than the pointed end. F-actin is quite rigid with a persistence length of 17 μm (Gittes, Mickey, Nettleton, & Howard, 1993), forming semiflexible polymer networks. The nucleation, polymerization, and organization of actin in cells is regulated and controlled by actin concentration and various actin binding proteins such as Arp2/3, Myosin II, and cofilin (Hotulainen & Hoogenraad, 2010) (Figure 7-1 C, D).

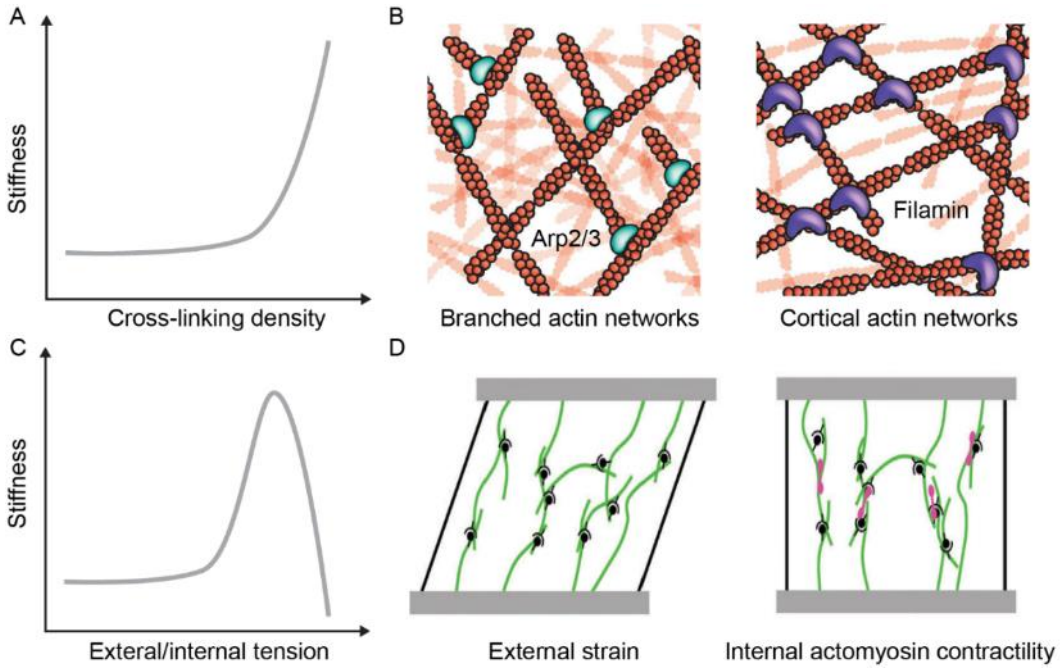

Figure 7-2 Elasticity of actin networks comes from cross-linking density or tension.
(A) A schematic diagram illustrating the elasticity of actin networks (stiffness) and cross-linking density. At low cross-linking density, the elasticity of actin networks exhibits no dependence on cross-linking density. At high cross-linking density, elasticity increases dramatically with cross-linking density. (B) Different F-actin (red) cross-linking architectures. Arp2/3(green)-mediated branched actin networks and filamin(purple)-mediated cortical actin networks are shown here. (C) A schematic diagram illustrating the elasticity of cross-linked actin networks and tension. Actin networks stiffen under an intermediate level of tension. (D) Tension applied on cross-linked (cross-linker shown in black) actin networks can be external strain or internal Myosin II (magenta)-mediated contractility. Diagrams are reprinted and adapted with permission from: A, (Gardel et al., 2004), © 2004 American Association for the Advancement of Science; B, (D. A. Fletcher & Mullins, 2010), © 2010 Macmillan Publishers Limited; C, D, (Mak, Kim, Zaman, & Kamm, 2015), © 2015 The Royal Society of Chemistry.

As the main cytoskeleton in spine heads, F-actin could be the primary source of spine stiffness. Elasticity of actin networks could come from actin cross-linking or tension applied to actin networks (Gardel et al., 2004). In the first case, in the presence of high concentration of cross-linkers, F-actin

could form complex architecture such as branched networks mediated by Arp2/3 (Mullins, Heuser, & Pollard, 1998) and cortical networks involving filamin (Stossel et al., 2001)(Figure 7-2 A, B). It is known that F-actin forms densely branched networks in spine heads (Korobova & Svitkina, 2010), which could be a source of high stiffness. In the second case, actin networks stiffen as they are strained to resist large deformation as a result of filament entanglement (Gardel et al., 2004; Storm, Pastore, MacKintosh, Lubensky, & Janmey, 2005). Tension could either come from external stress (Storm et al., 2005) or internal actomyosin contractility (Mizuno, Tardin, Schmidt, & MacKintosh, 2007)(Figure 7-2 C, D). Due to the presence of synaptic adhesion molecules and their catch bond features (Manibog et al., 2014; Rakshit et al., 2012), synapses and the intracellular actin networks could be under external stress, causing tension-dependent actin networks stiffening. In addition, given that Myosin II is present in spines (Korobova & Svitkina, 2010), internal actomyosin contractility may also contribute to actin networks stiffening.

In order to test how spine stiffness responds to drugs that are known to affect actin networks and spine morphology, neurons were treated with Latrunculin A (Lat A) and Blebbistatin (Blebb). I first confirmed the high level of F-actin at stiff spines with correlative TH-AFM/fluorescence imaging (Figure 7-3). After TH-AFM imaging, F-actin was stained with phalloidin which binds to all variants of actin filaments. Overlay of PSD-95, F-actin, and stiffness revealed concentrated F-actin in the spine head.

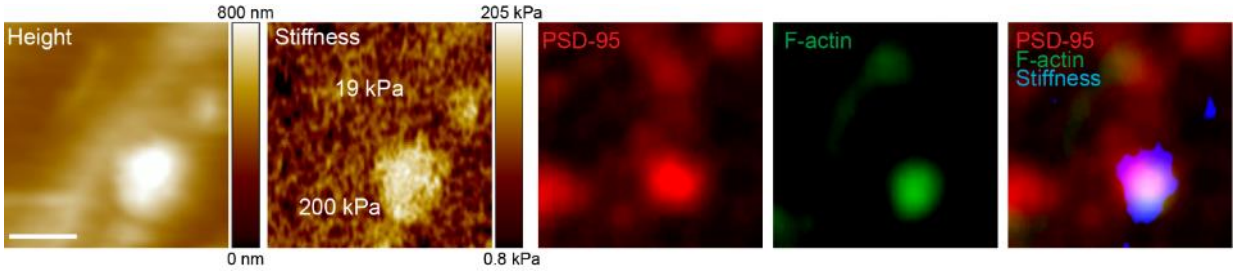

Figure 7-3 F-actin is enriched in a stiff spine head.
Aligned AFM height, AFM stiffness, and immunofluorescence images of the same area. Threshold was applied to the stiffness image colored in blue. F-actin (green) was enriched in the stiff spine (200 kPa), not in the dendritic shaft (19 kPa). Scale bar: 500 nm.

Lat A binds to actin monomers, preventing them from repolymerizing into filaments (Coue, Brenner, Spector, & Korn, 1987). It has been shown that Lat A disrupts F-actin in neurons and decreases spine density (Allison, Gelfand, Spector, & Craig, 1998). 12-24 hours of Lat A treatment significantly reduced global F-actin level in neurons (Figure 7-4).

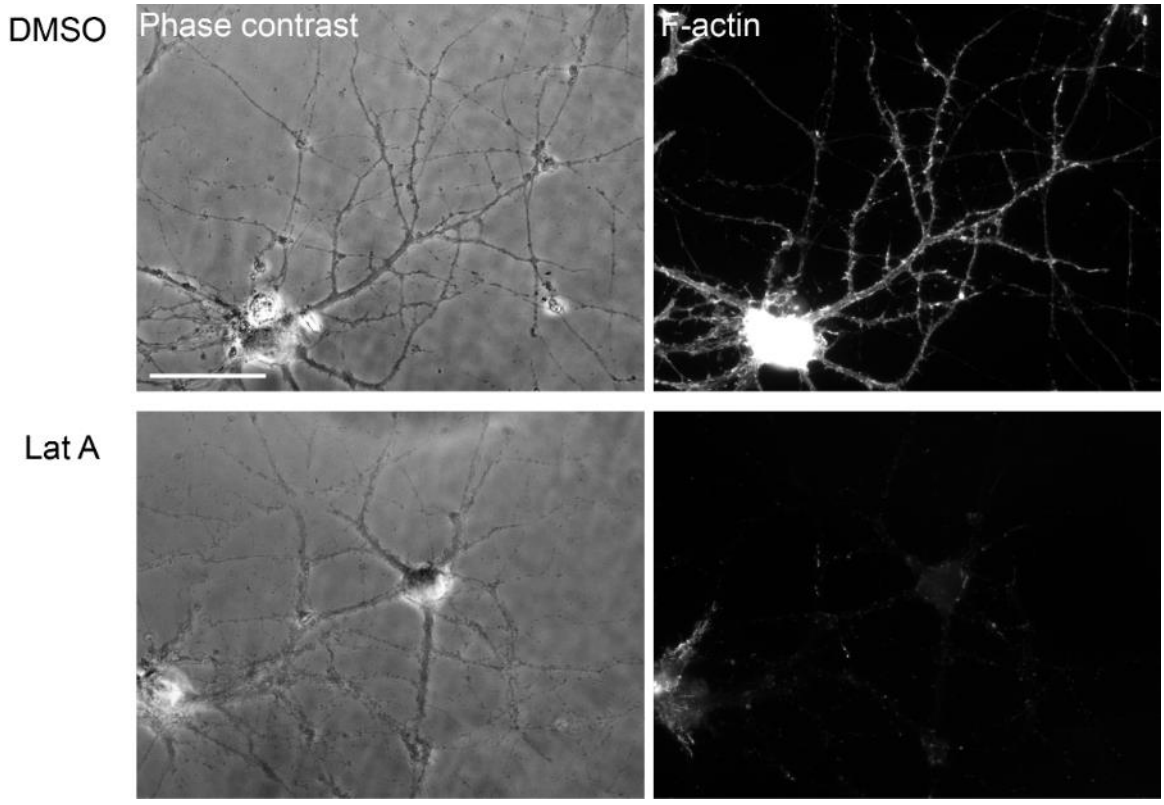

Figure 7-4 Latrunculin A reduces F-actin level in neurons.
Phase contrast and fluorescence images of F-actin in neuron cultures after 12-24 hour DMSO or 10 μM Lat A treatment. Lat A largely reduced F-actin level in neurons. Note there were still some puncta of F-actin after Lat A treatment, suggesting that some F-actin may be resistant of Lat A disruption. At least 3 randomly selected areas in each culture were imaged. 3 neuron cultures were treated with DMSO or Lat A, respectively. Scale bar: 100 μm.

Interestingly, I found that Lat A did not affect the stiffness of spines. 12-24 hours of Lat A treatment did not change the stiffness of spines and shafts (Figure 7-5 A, B). A representative spine in Figure 7-5 A still contained F-actin puncta after Lat A treatment, suggesting that F-actin in stiff spines could be resistant to Lat A. Time-lapse TH-AFM imaging in Figure 7-5 C and D showed that the stiffness of spines did not change substantially with Lat A during 4 hours.

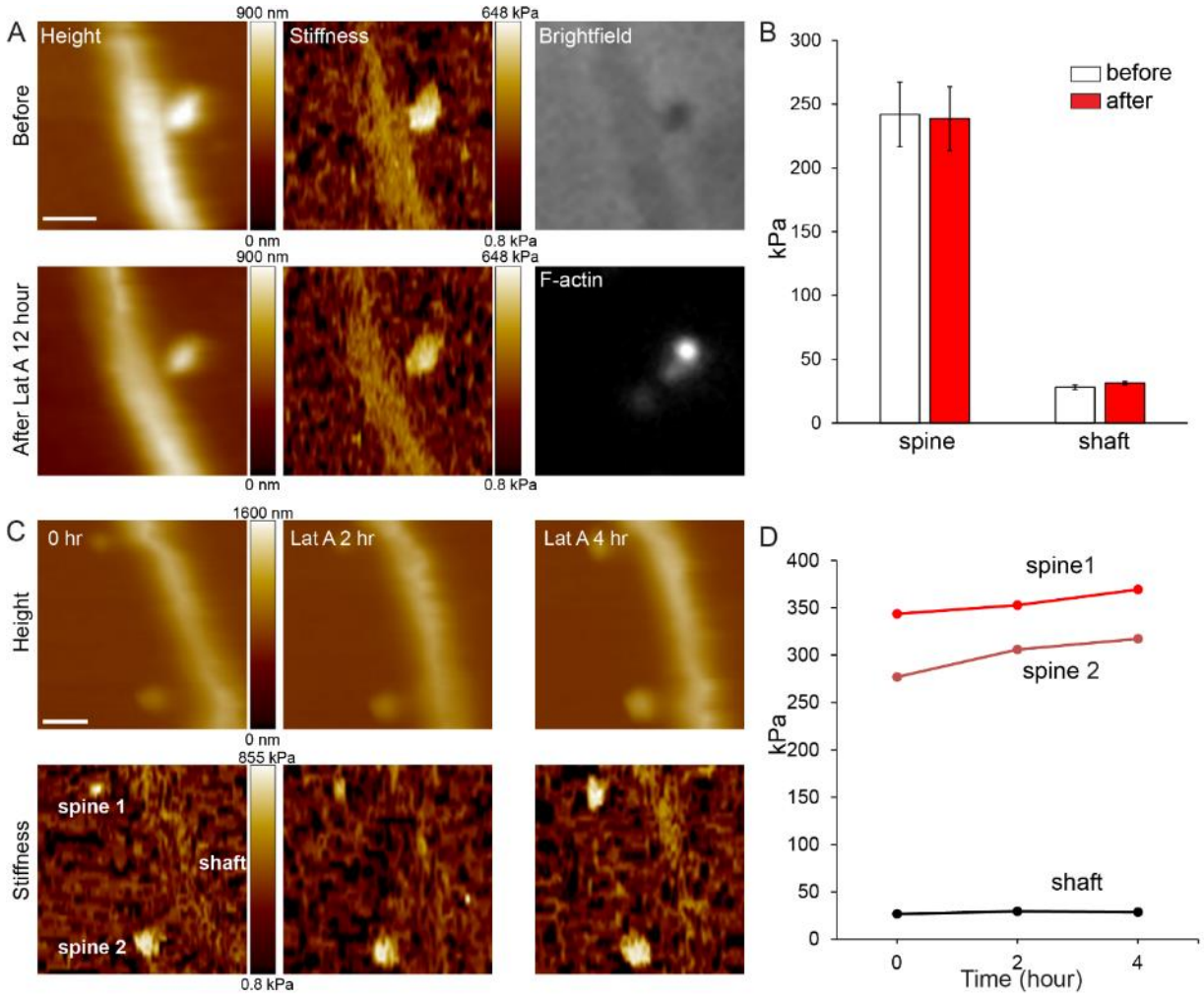

Figure 7-5 Spine stiffness is not affected by acute Latrunculin A treatment.
(A) AFM height, AFM stiffness, and brightfield images of the same spine before and after 12-hour Lat A treatment. Note the stiff spine still contained F-actin puncta in the fluorescence image after Lat A treatment. Scale bar: 1 μm. (B) Quantification of stiffness of 14 spines from 3 neuron cultures before and after Lat A treatment showed no significant difference (two-tailed paired t tests, $p_{spine} = 0.7289$, $p_{shaft} = 0.1009$). Data are shown as mean ± SEM. (C) Time-lapse TH-AFM height and stiffness images of the same area during 4-hour Lat A treatment. Scale bar: 1 μm. (D) Stiffness of two spines and a dendritic shaft (marked in the 0 hr stiffness image in (C)) did not decrease by Lat A. The change of their stiffness after 4 hours is 7%, 15% and 6%, respectively. These variations were small and could probably be due to measurement uncertainty.

The observation that spine stiffness was not affected by Lat A agrees with previous reports that mature neurons are more resistant to Lat A than young neurons and that in mature neurons a very small number of F-actin puncta remain resistant to Lat A, suggesting that a small population of F-actin is extremely stable (W. D. Zhang & Benson, 2001). Since Lat A only inhibits actin repolymerization without affecting preexisting F-actin directly, its effect on actin networks with a slow turnover rate may be limited. The balance between actin branching and elongation determines the

persistence and protrusion speed of actin networks (Figure 7-6). When branching exceeds elongation, which occurs in the presence of high Arp2/3 activity as in the case of spines, actin networks stiffen. Increased actin branching and decreased actin elongation could help maintain persistent and stable cellular structures (Krause & Gautreau, 2014). In addition to Arp2/3, capping proteins (shown in Figure 7-1 D) may also help maintain stable actin networks by protecting the barbed ends of F-actin and inhibiting elongation (Fan, Tang, Vitriol, Chen, & Zheng, 2011; Korobova & Svitkina, 2010).

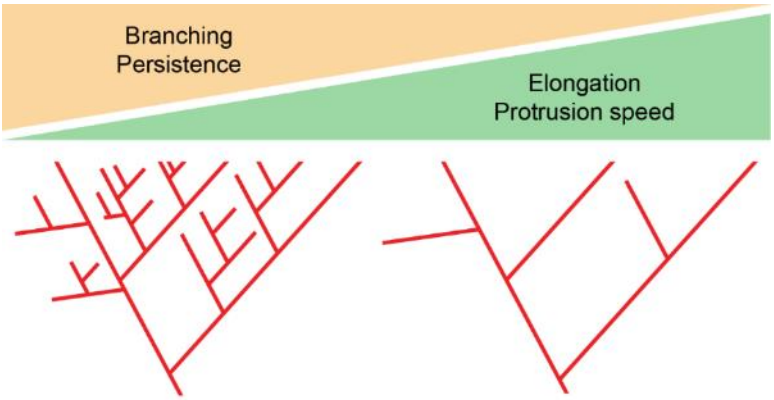

Figure 7-6 Actin branching and elongation in structural persistence.
Increased actin branching and decreased actin elongation leads to slow but persistent cellular structures. Conversely, increased actin elongation and decreased actin branching leads to faster but less persistent protrusion. The branching of actin networks is induced by Arp2/3 while the elongation of actin networks is supported by formins and reduced by capping proteins. Diagrams are adapted with permission from (Krause & Gautreau, 2014), © 2014 Macmillan Publishers Limited.

Since actomyosin contractility could cause stiffening of actin networks *in vitro* (Mizuno et al., 2007), I then studied whether spine stiffness is dependent on Myosin II-mediated tension. I used Blebb to inhibit the ATPase activity of Myosin II and actomyosin contractility (Kovacs, Toth, Hetenyi, Malnasi-Csizmadia, & Sellers, 2004). Blebb reduces the number of mushroom spines while promoting the growth of filopodia, and impairs excitatory synaptic transmission in neuron cultures (Ryu et al., 2006). In brain slices, Blebb does not change basic synaptic transmission or spine morphology, but reduces actin polymerization during synaptic plasticity, suggesting that Myosin II-mediated contractility may help organize actin structures through the tension applied to actin networks during learning and memory (Rex et al., 2010).

I reported that Blebb treatment did not affect spine stiffness in cultured neurons (Figure 7-7). I verified the Blebb protocol in fibroblasts and observed ruffles at cell edges and cell retraction as previously reported (Shutova, Yang, Vasiliev, & Svitkina, 2012). These results suggest that the elasticity of actin networks does not come from Myosin II-mediated tension applied to the actin networks.

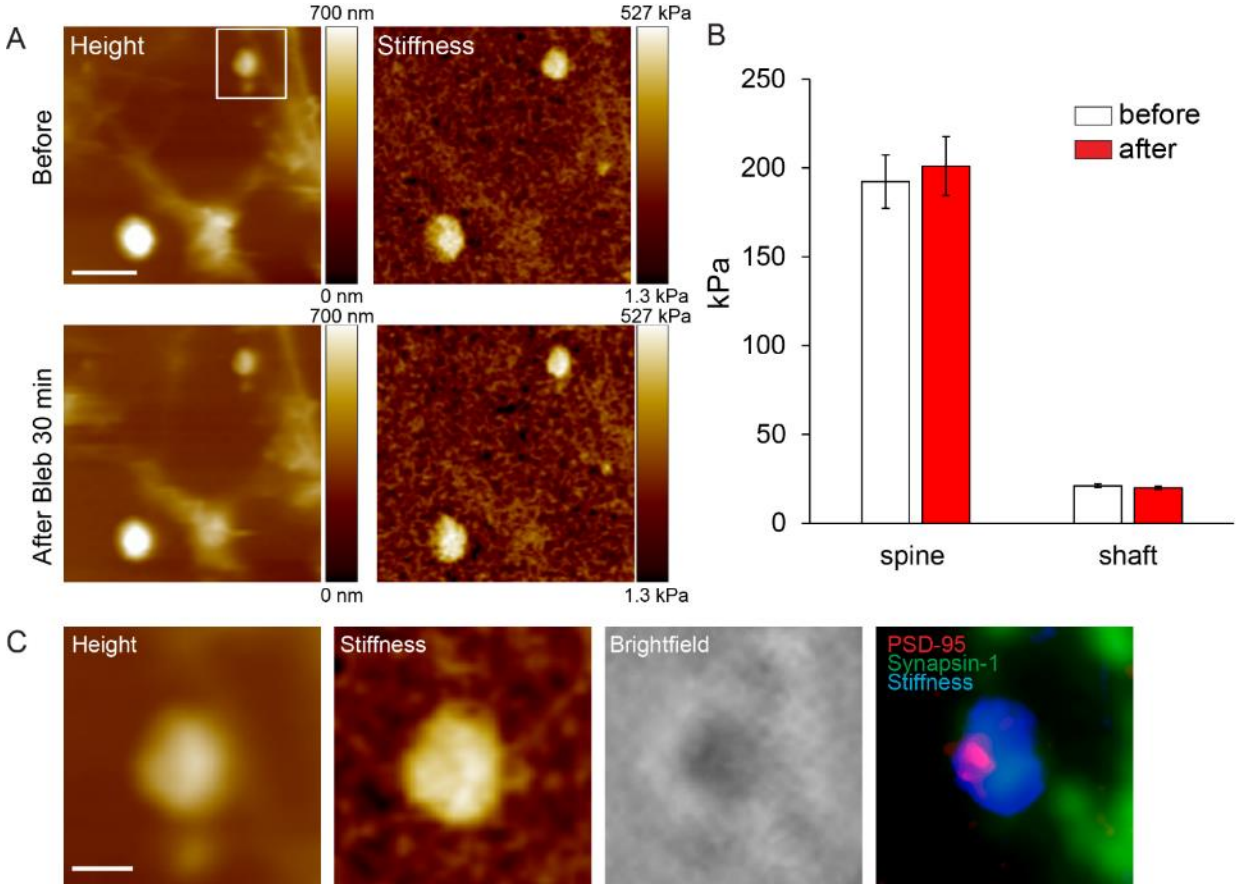

Figure 7-7 Spine stiffness is not affected by acute Blebbistatin treatment.
(A) AFM height and stiffness images of the same spine before and after 30-minute Blebbistatin treatment. Scale bar: 2 μm. (B) Quantification of stiffness of 36 spines from 6 neuron cultures before and after Blebbistatin treatment showed no significant difference (two-tailed paired t tests, $p_{spine} = 0.3126$, $p_{shaft} = 0.1330$). Data are shown as ± SEM. (C) Aligned AFM height, AFM stiffness, brightfield, and immunofluorescence images of the stiff spine from the boxed area shown in the AFM height image before treatment in (A). Threshold was applied to the stiffness image colored in blue. Scale bar: 500 nm.

Synapses as cell-cell junctions mimic focal adhesion in the sense that both require adhesion molecules and cytoskeleton networks to maintain a tight connection. It has been reported that inhibition of Myosin II activity does not prevent the formation of focal adhesion (Choi et al., 2008; Stricker, Beckham, Davidson, & Gardel, 2013), suggesting that the assembly and maturation of focal

adhesion is Myosin II independent or is mediated by a minimal level of Myosin II. While Blebb decreases the stiffness of stress fibers, focal adhesion remains stiff (Mandriota, 2016), suggesting that the stiffness of mature cell adhesion does not rely on Myosin II activity. In addition, Myosin II exists mainly in spine necks (Korobova & Svitkina, 2010), while the high stiffness observed here represents the spine head. Therefore, although Myosin II could be critical for synaptic function, its activity is not involved in the high stiffness of mature spines.

While I observed the same results consistently from several independent experiments, not observing a significant change in stiffness may suggest potential caveats. First, I used the conventional drug treatment protocols as used previously. A different drug concentration or incubation time may produce different results. Second, I verified drug activity at the cellular level. For Lat A, I observed a global reduced level of F-actin in cultured neurons. For Blebb, I observed ruffles at cell edges and cell retraction in fibroblasts. But I did not verify whether both drugs decrease spine density, as previously reported. It is possible that while these drugs are functional, they may not function well at the single spine level in the cultures and thus not affect spine stiffness. Third, there is a great heterogeneity in spines. In this work, I did not distinguish spines of different ages, motility, and functional strength. It may be worth investigating how different spines respond differently to drugs.

Given the presence of highly branched actin networks in spine heads (Korobova & Svitkina, 2010), spine stiffness is likely to originate from the cross-linked actin architecture mediated by Arp2/3. Arp 2/3, namely actin-related protein-2/3, is a complex of a stable assembly of seven proteins. Although Arp2/3 has little biochemical activity on its own, it cross-links F-actin at a y-branch junction in actin branching (Figure 7-1 C), referred to as dendritic nucleation (Mullins et al., 1998). Arp2/3 is localized to spine heads and is required for spine development and synaptic function (Wegner et al., 2008). It is interesting to investigate how Arp2/3 density and activity is correlated with spine stiffness in the future.

Next in Chapter 8, I will discuss how high spine stiffness may be involved in synaptic function and plasticity.

Chapter 8 Mechanical synaptic plasticity model

During learning, synapses become larger and stronger, allowing us to learn new skills and develop new memories. While larger synapses tend to be stronger, it remains unclear how becoming larger is mechanistically linked to becoming stronger.

In this Chapter, I will discuss how spine stiffness may play a role in synaptic strength and plasticity and propose a mechanical plasticity model that may causally link structural plasticity to functional plasticity of synapses.

The observations of the substantially high stiffness contrast between spines and shafts suggest potential physiological roles. First, stiffness might help maintain spine morphology in the presence of synaptic adhesion (8.1). Second, stiffness might help stabilize synaptic adhesion (8.2). Both mechanisms provide an approximate estimate of spine stiffness, which agrees with the measured spine elastic modulus values in Figure 6-3.

8.1 Stiffness helps maintain spine morphology in the presence of adhesion

The unique spine morphology with an enlarged head and a thin neck enables compartmentalization of chemical and electrical signals, which is critical for synaptic function and plasticity (Yuste and Bonhoeffer, 2001, Tonnesen et al., 2014). From a mechanical perspective, because adhesive forces can deform contacting bodies to increase contact area (Figure 8-1), high stiffness could help maintain morphology in the presence of strong adhesion. Indeed, a simple mechanical model of synaptic adhesion suggests that spine stiffness has to be on the order of 100 kPa to maintain its shape, which agrees with the measured values of spine stiffness in Figure 6-3.

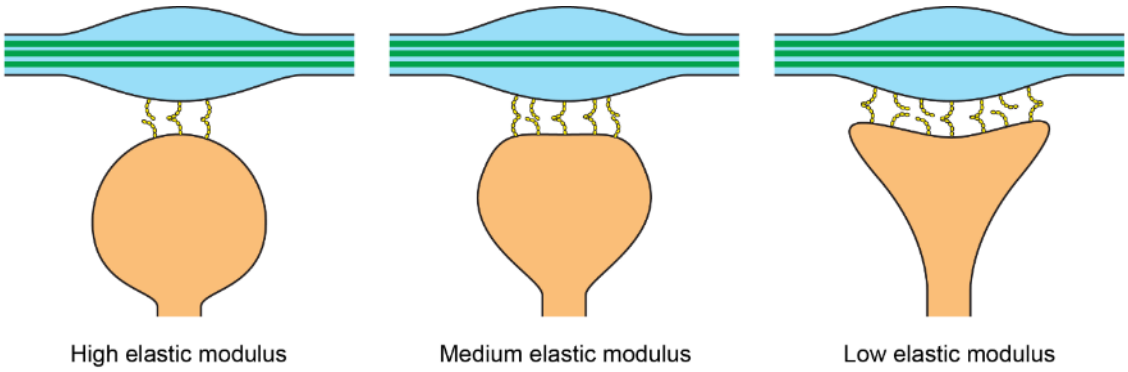

Figure 8-1 Stiffness helps maintain spine morphology.
The postsynaptic spine (orange) and the presynaptic axonal bouton (blue) are physically connected by synaptic adhesion molecules such as N-cadherin (yellow). Axon contains microtubules (green) and is under internal tension, which helps provide high stiffness. Based on a contact mechanics model, the contact area between the spine and the bouton is dictated by the interplay between adhesion and elastic modulus of the spine. Under the same adhesive energy, different spine elastic modulus values result in different shapes: while high elastic modulus (left) maintains the spherical morphology of the spine, low elastic modulus (right) results in an increased contact area and a distorted spine shape. Medium elastic modulus deforms the spine head into a mushroom-like shape.

To make an order of magnitude estimate of the minimal elastic modulus of a spine required

to maintain morphology in the presence of adhesive force, I used a contact mechanics model to relate deformation of contacting structures to adhesive force and elastic modulus. The spine-bouton system was treated as a pliable ball (spine head) pressing against a relatively flat and hard surface (bouton). Assuming that the spine head is deformed by the adhesive force at synapse and that no significant adhesive interaction occurs outside of the active zone, I used the Johnson-Kendall-Roberts (JKR) model (Johnson, Kendall, & Roberts, 1971) to estimate the minimal elastic modulus required. I assumed that the shape of the spine is deformed significantly when the diameter of the contact zone becomes comparable to the spine radius. Therefore, I determined the required elastic modulus to prevent the contact diameter from becoming larger than spine radius. According to the JKR model, contact radius (half the diameter) a could be written as the following:

$$a^3 = \frac{3R}{4E^*}\left(P + 3\gamma\pi R + \sqrt{6\gamma\pi RP + (3\gamma\pi R)^2}\right) \quad (6)$$

Here, R denotes the radius of curvature of a typical spine head, E^* denotes the effective elastic modulus, P denotes the applied load, and γ denotes the work of adhesion. Note that there could be pulling force across a synapse (Siechen et al., 2009), thus P is likely to be negative. However, the adhesive force must be significantly larger than the applied load P to hold the pre- and postsynapses together. Therefore, P was neglected in this model. I further assumed that the effective elastic modulus E^* primarily comes from the stiffness of the spine. This is because axon is under tension (Siechen et al., 2009), which could help maintain bouton's shape. Furthermore, the adhesion molecules on the presynaptic side could be ultimately connected to microtubules, which are resistant to deformation. I thus neglected bouton's elastic modulus, and derived the elastic modulus of the spine E^*:

$$E^* = \frac{9\pi R^2}{2a^3}\gamma \quad (7)$$

I assumed that the maximal contact radius at synapse interface to maintain the structural

integrity of the spine is half of the spine radius, i.e. $a = \frac{R}{2}$, and obtained the relationship between the minimal elastic modulus of the spine head E^* and the surface energy γ:

$$E^* = \frac{36\pi}{R}\gamma \tag{8}$$

To determine the minimal elastic modulus, we now needed to calculate the work of adhesion γ, which in the current model corresponds to the adhesion energy between pre- and postsynapses. For this, I considered the adhesion mediated by synaptic adhesion molecules. I modified the model developed by Chen et al. (C. P. Chen, Posy, Ben-Shaul, Shapiro, & Honig, 2005), which characterizes the adhesion mediated by pairs of adhesion molecules. According to Chen et al., the adhesive energy ΔG depends on the number of adhesion molecule dimers formed between two cells and the free energy of the monomer-dimer reaction:

$$\Delta G(I,J) = -N_{dimer}(I,J) \times \Delta g(i,j) \tag{9}$$

Here i and j indicate individual adhesion molecules in pre- and postsynapses, I and J, respectively. The adhesive energy between two pre- and postsynapses is defined as $\Delta G(I,J)$. $N_{dimer}(I,J)$ denotes the number of trans-dimers at the interface. $\Delta g(i,j)$ denotes the corresponding free energy (J/mole).

Assuming a local chemical equilibrium at cell-cell interface, the free energy can be calculated from dissociation constant K_d:

$$\Delta g(i,j) = -RTln(K_d) \tag{10}$$

I additionally assumed that adhesion molecules are enriched at synapse interface, i.e. active zone, and are freely diffusible at synapse surface, with surface density ρ. N denotes total number of one type of adhesion molecules on the membrane and A denotes total surface area where the molecules reside, i.e. active zone.

$$\rho = \frac{N}{A} \tag{11}$$

The 3D concentration of adhesion molecules could be converted from the 2D surface density using the "interfacial shell" model purposed by Chen et al.. Interfacial shell represents volume V containing interacting domains of adhesion molecules. For N-cadherin, this represents the EC1 domains. A_c denotes the surface area of a single adhesion molecule, therefore $A_c = \frac{A}{N}$. h denotes the shell thickness, which reflects the interactive structure of molecules. I used the thickness calculated by Chen et al., 12 nm. For simplicity, I applied the same thickness to all types of adhesion molecules.

$$V = A_c \times h \tag{12}$$

I then converted 2D density ρ to 3D effective concentration C, which represents the total 3D concentration of dimers C_{ij} and monomers C_i, $C = C_{ij} + C_i$. N_A is the Avogadro number.

$$C = \frac{\rho}{N_A \times h} \tag{13}$$

I assumed only trans-homodimers are formed at synapse, i.e. $i = j$. The equilibrium constant K_d is thus written as the following:

$$K_d = \frac{C_i \times C_j}{C_{ij}} = \frac{{C_i}^2}{C_{ij}} \tag{14}$$

Therefore, we could obtain a quadratic function of C_i:

$$\frac{{C_i}^2}{K_d} + C_i = \frac{N}{AhN_A} \tag{15}$$

Solving the above function, we could obtain C_i. The number of dimers N_{dimer} is written as:

$$N_{dimer} = C_{ij} \times V \times N \times N_A = \frac{{C_i}^2}{K_d} AhN_A \tag{16}$$

Taken together, adhesive energy ΔG at synapse can be written as the following:

$$\Delta G = AhN_A \frac{C^2}{K_d} RTln(K_d) \tag{17}$$

A denotes total surface area where the adhesion molecules reside, i.e. active zone. h denotes the shell thickness in the "interfacial shell" model. N_A is the Avogadro number. C represents the

concentration of monomers at synapse. ΔG has a unit of J/mole. ΔG was converted to surface energy γ in the unit J/m^2 by considering the number of molecules and the surface area at the active zone of the synapse:

$$\gamma = \frac{N}{N_A} \times \frac{\Delta G}{A} \tag{18}$$

N denotes total number of one type of adhesion molecules on the membrane. In this model, I considered the following 2 types of adhesion molecules: N-cadherin and NCAM-140, because they are widely-studied synaptic adhesion molecules and their dissociation constants have been measured. I estimated the number of each molecule at synapse based on mass spectrometry data (Peng et al., 2004) and used the morphological characteristics of an average synapse from electron microscopy 3D reconstruction data (Holderith et al., 2012; Wilhelm et al., 2014).

I calculated the surface energy to be 3.43E-04 J/m^2. From Equation (8), the minimal elastic modulus of the spine head could be obtained: 183 kPa. See Table 8-1, Table 8-2, Table 8-3, and Table 8-4 for values used in this model.

Characteristic	Symbol	Value
Active zone area	A	0.07 μm^2 (Wilhelm et al., 2014)
Spine volume	$V' = \frac{4}{3}\pi R^3$	0.04 μm^3 (Holderith et al., 2012)
Spine radius	R	0.212 μm

Table 8-1 Morphological characteristics of an average synapse.

Molecules at PSD	Abundance index by mass spectrometry of PSD (Peng et al., 2004)	Number of molecules per PSD
PSD-95	24.2	300
N-cadherin	2.5	31
NCAM-140	1.1	14

Table 8-2 Number of adhesion molecules at synapse.

	N-cadherin	NCAM-140
dissociation constant K_d (M)	2.58E-05 (Katsamba et al., 2009)	5.5E-05 (Kiselyov et al., 1997)
species	mouse	mouse
method	analytical ultracentrifugation	surface plasmon resonance

Table 8-3 Dissociation constant of synaptic adhesion molecules.

Parameter	Symbol	N-cadherin	NCAM-140
number per synapse	N	31	14
dissociation constant	K_d (M)	2.58E-05	5.5E-05
free energy	$\Delta g(i,j)$ (J/mole)	-2.62E+04	-2.43E+04
2D density on PSD	ρ (/μm^2)	442.74	194.81
interfacial shell thickness	h (nm)	12	12
surface area of a single pair of adhesion molecules	A_c (μm^2)	2.26E-03	5.13E-03
interfacial shell	V (L)	2.71E-20	6.16E-20
3D effective concentration	C (μM)	61.27	26.96
monomer concentration	C_i (μM)	28.90	19.82
dimer concentration	C_{ij} (μM)	32.37	7.14
number of monomers	N_i	14.62	10.03
number of dimers	N_{ij}	16.37	3.61
free energy on surface	$\Delta G(I,J)$ (J/mole)	4.29E+05	8.78E+04
total free energy on surface	W (J)	2.21E-17	1.99E-18
surface energy at interface	γ (J/m^2)	3.15E-04	2.84E-05

Table 8-4 Adhesive energy at synapse.

Total surface energy at synapse interface from these 2 types of adhesion molecules is 3.43E-04 J/m^2. Given there are many other types of adhesion molecules at synapse, this theoretical value is likely to be an underestimate of the actual surface energy at synapse.

8.2 Stiffness helps stabilize adhesion interaction

Theoretical modeling of cellular adhesion structures has shown that the lifetime of adhesion clusters depends on the stiffness of adhering surfaces (Qian & Gao, 2010). Due to the stochastic nature of molecular interactions, adhesion bonds rupture and rebind continuously. When bonds are ruptured, the surfaces can deform due to a small but non-zero force that pulls the surfaces apart. As illustrated in Figure 8-2 A and B, softer surfaces would be displaced more, thus increasing the distance between ruptured adhesion bonds, preventing their future rebinding, and decreasing the lifetime of the adhesion cluster. Gao et al. showed that a typical adhesion cluster is substantially stabilized as the sample stiffness increases beyond 50 to 100 kPa (Figure 8-2 C). The stiffness-adhesion relationship found in Gao et al's modeling could also be applicable to synaptic adhesion, because pre- and

postsynapses are connected together by transmembrane synaptic adhesion molecules (Missler, Sudhof, & Biederer, 2012). Indeed, one of these molecules, N-cadherin, has been shown to be strengthened on stiffer substrates in C2 mouse myogenic cells (Ladoux et al., 2010). Importantly, the measured spine elastic modulus values in Figure 6-3 (23.2 - 671.9 kPa with a median of 166.9 kPa, and 77.8% of measured spines have a stiffness over 100 kPa) correspond to the regime where the lifetime of adhesion would be greatly enhanced.

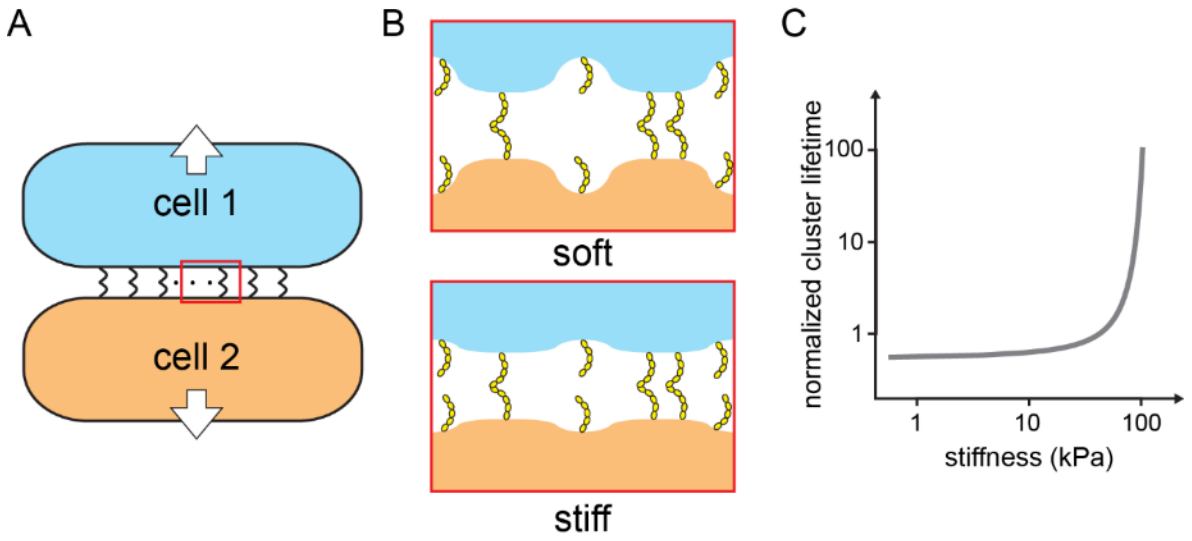

Figure 8-2 High stiffness stabilizes adhesion clusters.
(A) Two elastic bodies (blue and orange) are connected by a cluster of adhesion molecules (black springs) and are being pulled apart with a small but non-zero force (white arrows). (B) Zoomed-in diagrams from the red box in (A) highlight bound and ruptured adhesion molecules. N-cadherin is depicted here in yellow as an example. After adhesion bonds are ruptured, stiff sample results in a smaller surface separation compared with soft sample, substantially increasing the probability of rebinding, and thereby stabilizing the adhesion cluster at the interface. (C) A schematic stiffness-lifetime curve. Cluster lifetime is normalized to the spontaneous dissociation rate of the adhesion bond. Lifetime of the adhesion cluster increases drastically as the sample stiffens. Diagrams are adapted with permission from (Qian & Gao, 2010), © 2010 Qian and Gao.

8.3 Mechanical synaptic plasticity

Strengthening of adhesion via stiffness offers a potential role of mechanics in synaptic function. Synaptic adhesion molecules are essential for the formation, maturation, function, and plasticity of synapses. It is well known that synaptic adhesion molecules can recruit specific pre- and postsynaptic proteins and interact with various intracellular signaling molecules (Dalva, McClelland,

& Kayser, 2007). For example, N-cadherin could recruit and interact with PSD-95 (Togashi et al., 2002) and α-amino-3-hydroxy-5-methyl-4-isoxazolepropionic acid receptors (AMPAR) (Nuriya & Huganir, 2006; Saglietti et al., 2007), neuroligin could recruit N-methyl-D-aspartate receptors (NMDAR) (Chih, Engelman, & Scheiffele, 2005; Graf, Zhang, Jin, Linhoff, & Craig, 2004), and EphB receptors could bind and modulate NMDAR (Dalva et al., 2000) and interact with AMPAR (Kayser, McClelland, Hughes, & Dalva, 2006). In return, the location and interaction of synaptic adhesion molecules are regulated by synaptic activity. For example, N-cadherin localization and dimerization are regulated by NMDAR activation (Tanaka et al., 2000), and late-phase long-term potentiation (LTP) could lead to an increase in N-cadherin at synapses (Bozdagi, Shan, Tanaka, Benson, & Huntley, 2000). Given the stiffness-adhesion and adhesion-function relationships, stiffness could possibly play a role in regulating synaptic function via adhesion.

Spines contain highly branched actin networks cross-linked by Arp2/3 (Korobova & Svitkina, 2010), which serves as the branching block for actin networks and drives maturation from filopodia to mature spines (Spence, Kanak, Carlson, & Soderling, 2016). As spines mature, actin networks in spine heads undergo reorganization with increased level of branching mediated by Arp2/3 (Korobova & Svitkina, 2010). Because stiffness of polymer networks depends strongly on cross-linking density (Gardel et al., 2004), enhanced Arp2/3 activity and actin networks branching could cause spine stiffening. Arp2/3 activity is regulated by nucleation promoting factors such as N-WASP (neural Wiskott–Aldrich syndrome protein) (Wegner et al., 2008), which are activated by Rho GTPases such as Rac and Cac42 (Hotulainen & Hoogenraad, 2010). Rho GTPases are regulated by Ca^{2+}/calmodulin-dependent protein kinase II (CaMKII), which is activated by the elevated Ca^{2+} influx through NMDAR during LTP (Okamoto, Bosch, & Hayashi, 2009). Consequently, synaptic activity and plasticity could affect spine stiffness via Ca^{2+}-dependent signaling cascades and Arp2/3-based actin remodeling.

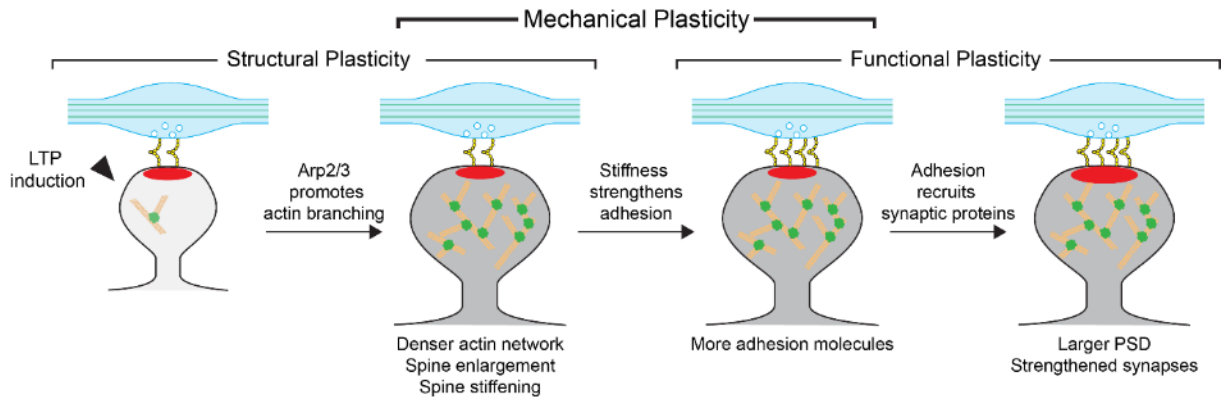

Figure 8-3 Mechanical synaptic plasticity model.
The postsynaptic spine (grey) and the presynaptic axonal bouton (blue) are physically connected by synaptic adhesion molecules such as N-cadherin (yellow). Spine with postsynaptic density (PSD; red) has enriched actin networks (orange) cross-linked by Arp2/3 (green), while axon contains microtubules (green line). During LTP, spine exhibits both structural plasticity and functional plasticity with spine enlargement, actin reorganization, PSD enlargement, and increase of synaptic transmission. I propose that mechanical plasticity may causally connect structural plasticity with functional plasticity. As shown by the dashed arrow, stiffness (indicated by the darkening grey color of the spine) strengthens synaptic adhesion, resulting in higher local surface density of adhesion molecules. Adhesion molecules then help recruit synaptic proteins including PSD-95, AMPAR, and NMDAR, resulting in PSD enlargement and functional potentiation. Upon subsequent stimulations, a strengthened spine with more adhesion molecules, NMDAR, and AMPAR would have more Ca^{2+} influx, causing further spine stiffening.

The proposed role of spine stiffness fits into the previously established LTP timeline: During LTP, NMDAR-dependent Ca^{2+} signaling cascade leads to structural plasticity involving spine enlargement and actin remodeling (Honkura et al., 2008; Matsuzaki et al., 2004; Okamoto et al., 2004; Zhou et al., 2004), followed by an increase in adhesion molecules such as N-cadherin (Bozdagi et al., 2000), followed by enlargement of the postsynaptic density (PSD) (M. Bosch et al., 2014; Meyer, Bonhoeffer, & Scheuss, 2014) potentially via Cortactin-Shank interaction (Cosen-Binker & Kapus, 2006; Hering & Sheng, 2001), and later an increase in synaptic receptors and enhanced synaptic strength. It remains unclear how structural plasticity is mechanistically linked to functional plasticity (Straub & Sabatini, 2014). I have suggested that during spine enlargement, enhanced actin cross-linking causes spine stiffening, which then facilitates the increase in synaptic adhesion molecules. Indeed, the data showed that spine stiffness was positively correlated with spine size, and it is well established that spine size is correlated with synaptic strength (Matsuzaki et al., 2001). Figure 8-2 showed that stiffness could reinforce the interaction of adhesion molecules at synapses, increasing

their local surface density. These mechanical aspects could causally link the observed structural synaptic plasticity and functional synaptic plasticity, via stiffness-dependent synaptic adhesion enhancement and adhesion-dependent recruitment of synaptic proteins (Figure 8-3). We term the resulting model "mechanical plasticity". This model suggests a positive feedback loop between spine stiffness and synaptic strength: spine stiffening causes spine strengthening, and a strengthened spine with more adhesion molecules, NMDAR, and AMPAR would have more Ca^{2+} influx upon subsequent stimulations, causing further stiffening of spines. The interdependence between stiffness and synaptic strength suggests that the increase of spine stiffness induced by stimulation is proportional to current spine stiffness and synaptic strength, thus spine stiffness grows exponentially, resulting in a lognormal distribution of spine stiffness at the population level.

Beyond its potential role in synaptic plasticity, stiffness might also be important in the long-term maintenance of synapses and memory storage. Previous studies have reported that a subpopulation of spines and axonal boutons are remarkably stable in the brain (Grutzendler, Kasthuri, & Gan, 2002; A. Holtmaat & Svoboda, 2009; A. J. Holtmaat et al., 2005). The highly stable stiffness of spines in the current observations may represent a stable structural component in the long-term maintenance of synapses. When spine stiffness is markedly high, synapses can be stable for a long time because the lifetime of synaptic adhesion is substantially enhanced. Enhanced lifetime of synaptic adhesion stabilizes the physical connection between pre- and postsynapses, and helps maintain synaptic function through recruitment and stabilization of synaptic scaffolding proteins and glutamate receptors. In this view, the stiffness-function feedback not only increases signal transmission at synapses, but also largely enhances the lifetime of synapses by activity-dependent spine stiffening and stiffness-dependent adhesion stabilization.

Chapter 9 Conclusion

The notion of synaptic mechanics and the characterization of synaptic elasticity paves the way for understanding synaptic function from a mechanical perspective and suggests that mechanical strength leads to functional strength.

In this Chapter, I will summarize my results and discuss future research directions.

This dissertation aims to characterize the nanomechanical properties of synapses and understand the potential role of synaptic mechanics in synaptic function. I found that, in cultured rat hippocampal neurons, postsynaptic spines at functional mature excitatory synapses were on average 10 times stiffer than dendritic shafts and axons. This intriguing result suggests a role for mechanical properties of spines in synapse formation and function. As I looked further into this possibility, I found in the data that spine stiffness was positively correlated with spine size. Since it is well established that spine size is correlated with synaptic strength, I developed a mechanical model that can explain how synaptic elasticity plays a role in enhancing synaptic strength during synaptic plasticity. Importantly, this model fills a gap in the timeline of the biochemical processes during LTP induction, specifically by offering a mechanistic link between structural plasticity and functional plasticity. Overall, these findings offer new insights into synapse formation, function, and long-term maintenance.

Mechanical behavior of cells has been studied for decades, mostly in fibroblasts and in connection with cell adhesion (Diz-Munoz et al., 2013; Vogel & Sheetz, 2006). However, the mechanical properties of synapses, the basic elements of neuronal activity in learning and memory, have not been studied in detail. Smith et al. have used force-volume atomic force microscopy (AFM) to map elasticity of spine-like structures in live neurons, and reported that the stiffness of visually-identified spherical spine-like structures observed in close proximity to axon-like structures was on average 2 times that of the dendritic shafts (Smith et al., 2007). However, the data acquisition using force-volume AFM could take tens of minutes, making it technically challenging to acquire high-throughput quantitative mechanical mapping in live cells at high speed, and limiting its application in biological studies.

In order to characterize synaptic elasticity, I have used torsional harmonic atomic force microscopy (TH-AFM). TH-AFM uses a specially designed T-shaped cantilever which allows a large number of synapses to be imaged and quantified in a short amount of time with small indentation as

discussed in Chapter 2. Compared with the conventional force-volume AFM, TH-AFM is capable of measuring time-resolved tip-sample interaction forces at microsecond scale with high signal-to-noise ratio, high force sensitivity, and high spatiotemporal resolution. Using TH-AFM, I have performed nanomechanical imaging in live cultured hippocampal neurons in Chapter 3, and observed stiff synapse-like structures. While AFM can provide high resolution topography and mechanical property images, AFM alone does not fully confirm cellular and subcellular identity, nor can it reveal cell activity and intracellular ultrastructure.

In order to reveal complex cellular structures of interest, I have successfully combined TH-AFM with fluorescence microscopy in Chapter 4 and with serial section transmission electron microscopy (TEM) in Chapter 5. Correlative TH-AFM/immunostaining of synaptic markers and functional labeling of boutons confirms that stiff structures were indeed functional mature excitatory synapses. Correlative TH-AFM/TEM imaging revealed that high stiffness originated from postsynaptic spines, but not presynaptic boutons. To my knowledge, this is the first work that presents AFM-based mechanical analysis together with the TEM study of the same cellular structure. This is especially important for applications in neuroscience research because TEM can verify the biological identity of cellular substructures. Without such information, it is very difficult to interpret mechanical measurements.

The present work thus addresses an important methodological necessity for mechanical characterization of synapses. Conventional optical (fluorescence) microscopy is capable of visualizing cell morphology and identifying target proteins with immunostaining in live or fixed cells, but the resolution limit of 200 nm hinders its capacity to provide accurate protein localization and high resolution cell imaging. TEM provides ultra-high resolution of intracellular structures in fixed cells, but sample preparation and imaging can be technically challenging and time-consuming. AFM is capable of acquiring high resolution topographical and mechanical imaging in live cells, thus providing

critical information about cell behavior and characteristics from a mechanical perspective complementary to optical microscopy and TEM. Combination and correlation of different independent imaging methods allows us to assess cell mechanics in detail and correlate them with biochemical processes, cellular activity and function, and intracellular structure, providing a more comprehensive picture of synaptic structure and mechanics.

Not all spines are created equal. Spines vary in their morphology, molecular organization, and strength, creating a broad spectrum of input-specific structural and functional plasticity. I have performed detailed statistical analysis and showed spine stiffness also exhibited a huge heterogeneity in Chapter 6. I have reported a more substantial difference (10 times on average) in stiffness between spines and shafts than previously reported (Smith et al., 2007), which could be due to the differences between the two methods. Force-volume method requires larger forces and indentation depths than TH-AFM. With thin compliant structures like synapses and dendritic shafts, large indentation depths lead to probing of the underlying rigid substrate and thereby reduce stiffness contrast. Due to lower forces required to make stiffness measurements, TH-AFM is more sensitive to the mechanical properties of the compliant cellular structures. I have also shown that unlike spines, shaft synapses and immature filopodia did not display high stiffness, suggesting that shaft synapses could be mechanically distinct from spiny synapses and that spines might stiffen during maturation. The surprisingly high stiffness of spines may represent a unique parameter complementary to the traditional biochemical and electrophysiological ones, and it may be related to synaptic activity and function.

Spines are essentially actin bags and have densely cross-linked actin networks. Thus actin networks could be the primary source of spine stiffness. In order to understand the how spine stiffness is related to actin networks, I have treated neurons with drugs that affect actin networks in Chapter 7 and reported that neither Latrunculin A nor Blebbistatin affected spine stiffness. While both drugs are

shown to affect spine morphology and reduce spine density in general, their effect on existing mature and stable spines may be limited. Given that the elasticity of actin networks could come from cross-linking density or tension applied on the actin networks and that spine heads contain highly branched actin networks mediated by Arp2/3, I suggest that spine stiffness is likely to originate from actin cross-linking.

Based on the stiffness measurements and theoretical modeling of cell adhesion, I have proposed the mechanical plasticity model in Chapter 8. The proposed role of synaptic elasticity fits into the current LTP timeline. Mechanical plasticity not only causally links the observed structural synaptic plasticity and functional synaptic plasticity, via stiffness-dependent synaptic adhesion enhancement and adhesion-dependent recruitment of synaptic proteins, but also offers a mechanism that can facilitate the long-term maintenance of synaptic structure and function. Therefore, this work could be an important addition to the current literature in both synaptic adhesion and plasticity. Studies in both fields primarily focus on the biochemical changes in synapses. The mechanical plasticity model could then provide new research directions in both fields.

There are a few limitations in the present work. First, I have used *in vitro* hippocampal neuron cultures, which consist of a highly homogeneous cell population of pyramidal neurons. *In vitro* cell cultures may not fully represent *in vivo* cells, and it is always ideal if the *in vitro* results could be reproduced *in vivo*. Due to the limitation of AFM technique, it is incapable of imaging *in vivo* synapses. Nevertheless, the substantially high stiffness contrast (on average 10 times) between spines and shafts is unlikely due to artifacts of the *in vitro* culture condition considering that it requires a great amount of energy and regulation to establish highly localized and densely cross-linked actin networks in cells. Second, since I have used certain criteria to identify synapse-like structures under TH-AFM (stiffness larger than 20 kPa), I may rule out spines that are softer than 20 kPa. Nevertheless, given that the measured spine stiffness has a lognormal-like distribution with a peak around 164 kPa, very few spines

would be excluded by these criteria. Third, I have not observed a substantial stiffness change during the imaging, even in the presence of actin drugs, which seems inconsistent with previous reports of high spine dynamics and motility (Dunaevsky, Tashiro, Majewska, Mason, & Yuste, 1999). However, in this study, I have only looked at mature synapses, but not immature filopodia. It is likely that while spines (in a broader sense) may or may not form a synapse with a presynaptic terminal, the spines in the analysis only represent those with a presynaptic terminal, and are thus more stable and less susceptible to drugs. Fourth, not observing any change suggests the extremely high stability of these stiff spines. At the same time, it also raises a question: if these spines are so stable, how do they get eliminated when needed? Considering the similarity between synaptic adhesion and focal adhesion, I suggest that the removal of mature spines requires clathrin-mediated endocytosis of adhesion molecules as in focal adhesion (Ezratty, Bertaux, Marcantonio, & Gundersen, 2009), a signal that is actively regulated and strictly controlled. Therefore, it is interesting to see whether removal or inhibition of adhesion interactions would reduce spine stiffness. Fifth, in this work, I only investigated excitatory synapses labeled with PSD-95 and did not study inhibitory synapses which are usually formed on dendritic shafts and do not have spines (van Spronsen & Hoogenraad, 2010). My results that shaft excitatory synapses were not stiff and that dendritic shafts displayed a relatively uniform stiffness suggest that inhibitory synapses without spines may not be stiff. Without high stiffness, how is the adhesion structure at inhibitory synapses stabilized as discussed in the model in 8.2? I hypothesize that stiffness at inhibitory synapses may be provided by the underlying microtubules which can be connected to adhesion molecules through actin and gephyrin (van Spronsen & Hoogenraad, 2010). Microtubules have a long persistence length (Gittes et al., 1993) and thus can be highly stiff, but they may not be accessible by the AFM tip during indentation because the indentation depth used was around 30 nm, which is not deep enough to probe microtubules. As a result, AFM images in my experiment did not show high stiffness along dendritic shafts which contain

microtubules.

Future work can begin to investigate how spine stiffness changes with synaptic strength. The present work focuses on the baseline characterization of synaptic elasticity at the population level. The correlation analysis has shown that spine stiffness was correlated with spine size, which is known to be correlated with synaptic strength. But I have not proved that spine stiffness is correlated with synaptic strength because I did not measure synaptic strength directly. Functional labeling with FM dyes provides a qualitative assessment of synaptic activity, but not a quantitative one. In order to study quantitatively how spine stiffness is correlated with synaptic strength, one possible approach is to combine AFM imaging with functional imaging using glutamate uncaging. Single-spine LTP could be induced by glutamate uncaging, causing an enlargement of the spine and an increase of synaptic transmission (M. Bosch et al., 2014; Matsuzaki et al., 2004). It is interesting to study how spine stiffness would change during this process.

Future work can also study the correlation between spine stiffness and Arp2/3 level in cells. I have suggested that spine stiffness originates from Arp2/3-mediated actin cross-linking. Although it is well studied that the elasticity of actin networks increases drastically with cross-linking density in test tubes (Gardel et al., 2004), it is technically difficult to study the causal link between Arp2/3 and the stiffness of spines in cells. Because there are no Arp2/3 inhibitor drugs, one way to downregulate Arp2/3 is to use RNAi, which has been shown to reduce spine density and synaptic function (Wegner et al., 2008). However, RNAi only interferes new protein synthesis, but does not affect existing proteins. Some Arp2/3 proteins may be stably integrated in actin networks, and thus not affected by RNAi. RNAi also has low efficiency in mature neurons. As a result, there will always be a substantial amount of Arp2/3 being translated. Since the elasticity of actin networks increases greatly with Arp2/3 level, a small amount of Arp2/3 might be sufficient to maintain high spine stiffness. Even if RNAi works perfectly and eliminates all Arp2/3 proteins in spines, there will not be any spines left to

measure given that the existence of spines requires stable and cross-linked actin networks. Another approach to reduce Arp2/3 level is to use neurons with Arp2/3 mutations. However, since Arp2/3 is essential for spine development, Arp2/3 mutants may not develop into mature synapses properly, thus affecting the basic structure and function of spines. Instead of studying a causal link, a correlation analysis between Arp2/3 level and spine stiffness in normal neurons would also provide insights into the role of Arp2/3 in spine stiffness. In order to study how Arp2/3 is correlated with spine stiffness, one possible approach is to combine AFM with immuno-gold TEM or super-resolution optical microscopy such as stochastic optical reconstruction microscopy (STORM) (C. Xu, Liu, H., Qi, L., Hao, G., Shen, Z., Wang, Y., Babcock, H., Lau, P., Zhuang, X, Bi, G., 2017) which allows accurate quantification of the number of proteins at synapses. Correlative TH-AFM/immuno-gold TEM or correlative TH-AFM/STORM could offer insights into the relationship between spine stiffness and cross-linking density in spines. Using this approach, it is also interesting to study how spine stiffness is correlated with other proteins of interest, such as N-cadherin and NMDAR.

Furthermore, the notion of synaptic mechanics and the characterization of synaptic elasticity with TH-AFM in my current work paves the way for understanding brain functions from a mechanical perspective. Previous brain research has focused extensively on the biochemical and electrophysiological properties of the brains and synapses, while synaptic mechanics has not received much attention. This is partly due to a lack of interdisciplinary collaboration between the neuroscience community and the physics community, and a lack of proper tools and techniques to probe synaptic mechanics. However, the brain is indeed a mechanically sensitive organ and synapses are mechanically interesting cellular structures. The influence of mechanical energy on the brains and synapses of living organisms is omnipresent (Tyler, 2012), not only in normal functions such as neuronal development (Lamoureux et al., 2002), action potential propagation (El Hady & Machta, 2015), synaptic transmission (Siechen et al., 2009), but also in concussion and traumatic brain injury (Meaney & Smith,

2011; L. Zhang, Rzigalinski, Ellis, & Satin, 1996), and neurodegenerative diseases such as Alzheimer's disease (Murphy et al., 2011). Understanding how synaptic mechanics is involved in synaptic function and how synaptic elasticity is related to synaptic plasticity will provide novel insights into brain functions and disease states, and offer unique mechanical diagnostic markers complementary to the traditional biochemical ones (Plodinec et al., 2013; Stolz et al., 2009)

In summary, I characterized synaptic elasticity and observed that spines at functional mature excitatory synapses were on average 10 times stiffer than dendritic shafts. I propose a mechanical synaptic plasticity model and suggest that mechanical strength leads to functional strength. The mechanical synaptic plasticity model provides a potential causal link between structural plasticity and functional plasticity of synapses during learning, and offers a mechanism that can facilitate the long-term maintenance of synaptic structure and function during memory.

References

Ahmed, W. W., Li, T. C., Rubakhin, S. S., Chiba, A., Sweedler, J. V., & Saif, T. A. (2012). Mechanical Tension Modulates Local and Global Vesicle Dynamics in Neurons. *Cellular and Molecular Bioengineering, 5*(2), 155-164. doi:10.1007/s12195-012-0223-1

Allison, D. W., Gelfand, V. I., Spector, I., & Craig, A. M. (1998). Role of actin in anchoring postsynaptic receptors in cultured hippocampal neurons: differential attachment of NMDA versus AMPA receptors. *Journal of Neuroscience, 18*(7), 2423-2436.

Ando, T., Kodera, N., Takai, E., Maruyama, D., Saito, K., & Toda, A. (2001). A high-speed atomic force microscope for studying biological macromolecules. *Proc Natl Acad Sci U S A, 98*(22), 12468-12472. doi:10.1073/pnas.211400898

Arnadottir, J., & Chalfie, M. (2010). Eukaryotic Mechanosensitive Channels. *Annual Review of Biophysics, Vol 39, 39*, 111-137. doi:10.1146/annurev.biophys.37.032807.125836

Bahler, M., & Greengard, P. (1987). Synapsin I bundles F-actin in a phosphorylation-dependent manner. *Nature, 326*(6114), 704-707. doi:10.1038/326704a0

Baines, A. J., & Bennett, V. (1986). Synapsin-I Is a Microtubule-Bundling Protein. *Nature, 319*(6049), 145-147. doi:DOI 10.1038/319145a0

Banker, G. A. (1980). Trophic Interactions between Astroglial Cells and Hippocampal-Neurons in Culture. *Science, 209*(4458), 809-810. doi:DOI 10.1126/science.7403847

Barlow, S. M. (1991). Modulation of mechanically evoked perioral reflexes during active force. *Brain Res, 565*(2), 330-336.

Bartlett, W. P., & Banker, G. A. (1984). An Electron-Microscopic Study of the Development of Axons and Dendrites by Hippocampal-Neurons in Culture .2. Synaptic Relationships. *Journal of Neuroscience, 4*(8), 1954-1965.

Begemann, I., & Galic, M. (2016). Correlative Light Electron Microscopy: Connecting Synaptic Structure and Function. *Front Synaptic Neurosci, 8*, 28. doi:10.3389/fnsyn.2016.00028

Benoit, M., Gabriel, D., Gerisch, G., & Gaub, H. E. (2000). Discrete interactions in cell adhesion measured by single-molecule force spectroscopy. *Nature Cell Biology, 2*(6), 313-317. doi:Doi 10.1038/35014000

Betz, W. J., Mao, F., & Bewick, G. S. (1992). Activity-Dependent Fluorescent Staining and Destaining of Living Vertebrate Motor-Nerve Terminals. *Journal of Neuroscience, 12*(2), 363-375.

Bhushan, B. (2008). Nanotribology and nanomechanics in nano/biotechnology. *Philos Trans A Math Phys Eng Sci, 366*(1870), 1499-1537. doi:10.1098/rsta.2007.2170

Biffi, E., Regalia, G., Menegon, A., Ferrigno, G., & Pedrocchi, A. (2013). The Influence of Neuronal Density and Maturation on Network Activity of Hippocampal Cell Cultures: A Methodological Study. *PLoS One, 8*(12). doi:ARTN e83899
10.1371/journal.pone.0083899

Binnig, G., Quate, C. F., & Gerber, C. (1986). Atomic force microscope. *Phys Rev Lett, 56*(9), 930-933. doi:10.1103/PhysRevLett.56.930

Binnig, G., Rohrer, H., Gerber, C., & Weibel, E. (1982). Tunneling through a Controllable Vacuum Gap. *Applied Physics Letters, 40*(2), 178-180. doi:Doi 10.1063/1.92999

Bock, D. D., Lee, W. C. A., Kerlin, A. M., Andermann, M. L., Hood, G., Wetzel, A. W., . . . Reid, R. C. (2011). Network anatomy and in vivo physiology of visual cortical neurons. *Nature, 471*(7337), 177-U159. doi:10.1038/nature09802

Bosch, C., Martinez, A., Masachs, N., Teixeira, C. M., Fernaud, I., Ulloa, F., . . . Soriano, E. (2015).

FIB/SEM technology and high-throughput 3D reconstruction of dendritic spines and synapses in GFP-labeled adult-generated neurons. *Frontiers in Neuroanatomy, 9*, 60. doi:10.3389/fnana.2015.00060

Bosch, M., Castro, J., Saneyoshi, T., Matsuno, H., Sur, M., & Hayashi, Y. (2014). Structural and molecular remodeling of dendritic spine substructures during long-term potentiation. *Neuron, 82*(2), 444-459. doi:10.1016/j.neuron.2014.03.021

Boyer, C., Schikorski, T., & Stevens, C. F. (1998). Comparison of hippocampal dendritic spines in culture and in brain. *Journal of Neuroscience, 18*(14), 5294-5300.

Bozdagi, O., Shan, W., Tanaka, H., Benson, D. L., & Huntley, G. W. (2000). Increasing numbers of synaptic puncta during late-phase LTP: N-cadherin is synthesized, recruited to synaptic sites, and required for potentiation. *Neuron, 28*(1), 245-259.

Brewer, G. J., Torricelli, J. R., Evege, E. K., & Price, P. J. (1993). Optimized Survival of Hippocampal-Neurons in B27-Supplemented Neurobasal(Tm), a New Serum-Free Medium Combination. *Journal of Neuroscience Research, 35*(5), 567-576. doi:DOI 10.1002/jnr.490350513

Buckley, C. D., Tan, J. Y., Anderson, K. L., Hanein, D., Volkmann, N., Weis, W. I., . . . Dunn, A. R. (2014). The minimal cadherin-catenin complex binds to actin filaments under force. *Science, 346*(6209), 600-+. doi:ARTN 1254211

10.1126/science.1254211

Burette, A., Collman, F., Micheva, K. D., Smith, S. J., & Weinberg, R. J. (2015). Knowing a synapse when you see one. *Frontiers in Neuroanatomy, 9*. doi:ARTN 100

10.3389/fnana.2015.00100

Burette, A. C., Lesperance, T., Crum, J., Martone, M., Volkmann, N., Ellisman, M. H., & Weinberg, R. J. (2012). Electron Tomographic Analysis of Synaptic Ultrastructure. *Journal of Comparative Neurology, 520*(12), 2697-2711. doi:10.1002/cne.23067

Butt, H. J., Cappella, B., & Kappl, M. (2005). Force measurements with the atomic force microscope: Technique, interpretation and applications. *Surface Science Reports, 59*(1-6), 1-152. doi:10.1016/j.surfrep.2005.08.003

Buzsaki, G., & Mizuseki, K. (2014). The log-dynamic brain: how skewed distributions affect network operations. *Nature Reviews Neuroscience, 15*(4), 264-278. doi:10.1038/nrn3687

Chacko, J. V., Zanacchi, F. C., & Diaspro, A. (2013). Probing Cytoskeletal Structures by Coupling Optical Superresolution and AFM Techniques for a Correlative Approach. *Cytoskeleton, 70*(11), 729-740. doi:10.1002/cm.21139

Chavis, P., & Westbrook, G. (2001). Integrins mediate functional pre- and postsynaptic maturation at a hippocampal synapse. *Nature, 411*(6835), 317-321. doi:Doi 10.1038/35077101

Chen, C. P., Posy, S., Ben-Shaul, A., Shapiro, L., & Honig, B. H. (2005). Specificity of cell-cell adhesion by classical cadherins: Critical role for low-affinity dimerization through beta-strand swapping. *Proceedings of the National Academy of Sciences of the United States of America, 102*(24), 8531-8536. doi:10.1073/pnas.0503319102

Chen, X. B., Nelson, C. D., Li, X., Winters, C. A., Azzam, R., Sousa, A. A., . . . Reese, T. S. (2011). PSD-95 Is Required to Sustain the Molecular Organization of the Postsynaptic Density. *Journal of Neuroscience, 31*(17), 6329-6338. doi:10.1523/Jneurosci.5968-10.2011

Cheng, D., Hoogenraad, C. C., Rush, J., Ramm, E., Schlager, M. A., Duong, D. M., . . . Peng, J. (2006). Relative and absolute quantification of postsynaptic density proteome isolated from rat forebrain and cerebellum. *Mol Cell Proteomics, 5*(6), 1158-1170. doi:10.1074/mcp.D500009-MCP200

Chereau, R., Saraceno, G. E., Angibaud, J., Cattaert, D., & Nagerl, U. V. (2017). Superresolution imaging reveals activity-dependent plasticity of axon morphology linked to changes in action potential conduction velocity. *Proceedings of the National Academy of Sciences of the United States of*

America, 114(6), 1401-1406. doi:10.1073/pnas.1607541114
Chih, B., Engelman, H., & Scheiffele, P. (2005). Control of excitatory and inhibitory synapse formation by neuroligins. *Science, 307*(5713), 1324-1328. doi:10.1126/science.1107470
Cho, K. O., Hunt, C. A., & Kennedy, M. B. (1992). The rat brain postsynaptic density fraction contains a homolog of the Drosophila discs-large tumor suppressor protein. *Neuron, 9*(5), 929-942.
Choi, C. K., Vicente-Manzanares, M., Zareno, J., Whitmore, L. A., Mogilner, A., & Horwitz, A. R. (2008). Actin and alpha-actinin orchestrate the assembly and maturation of nascent adhesions in a myosin II motor-independent manner. *Nature Cell Biology, 10*(9), 1039-1050. doi:10.1038/ncb1763
Christ, A. F., Franze, K., Gautier, H., Moshayedi, P., Fawcett, J., Franklin, R. J. M., . . . Guck, J. (2010). Mechanical difference between white and gray matter in the rat cerebellum measured by scanning force microscopy. *Journal of Biomechanics, 43*(15), 2986-2992. doi:10.1016/j.jbiomech.2010.07.002
Cingolani, L. A., & Goda, Y. (2008). Actin in action: the interplay between the actin cytoskeleton and synaptic efficacy (vol 9, pg 344, 2008). *Nature Reviews Neuroscience, 9*(6), 494-494. doi:10.1038/nrn2410
Cole, K. S. (1932). Surface forces of the Arbacia egg. *Journal of Cellular and Comparative Physiology, 1*(1), 1-9. doi:DOI 10.1002/jcp.1030010102
Cosen-Binker, L. I., & Kapus, A. (2006). Cortactin: the gray eminence of the cytoskeleton. *Physiology (Bethesda), 21*, 352-361. doi:10.1152/physiol.00012.2006
Coue, M., Brenner, S. L., Spector, I., & Korn, E. D. (1987). Inhibition of actin polymerization by latrunculin A. *FEBS Lett, 213*(2), 316-318.
Crick, F. (1982). Do Dendritic Spines Twitch. *Trends in Neurosciences, 5*(2), 44-46. doi:Doi 10.1016/0166-2236(82)90020-0
Cross, S. E., Jin, Y. S., Rao, J., & Gimzewski, J. K. (2007). Nanomechanical analysis of cells from cancer patients. *Nature Nanotechnology, 2*(12), 780-783. doi:10.1038/nnano.2007.388
Cullen, D. K., Gilroy, M. E., Irons, H. R., & LaPlaca, M. C. (2010). Synapse-to-neuron ratio is inversely related to neuronal density in mature neuronal cultures. *Brain Research, 1359*, 44-55. doi:10.1016/j.brainres.2010.08.058
Curry, N., Ghezali, G., Kaminski Schierle, G. S., Rouach, N., & Kaminski, C. F. (2017). Correlative STED and Atomic Force Microscopy on Live Astrocytes Reveals Plasticity of Cytoskeletal Structure and Membrane Physical Properties during Polarized Migration. *Front Cell Neurosci, 11*, 104. doi:10.3389/fncel.2017.00104
Dalva, M. B., McClelland, A. C., & Kayser, M. S. (2007). Cell adhesion molecules: signalling functions at the synapse. *Nature Reviews Neuroscience, 8*(3), 206-220. doi:10.1038/nrn2075
Dalva, M. B., Takasu, M. A., Lin, M. Z., Shamah, S. M., Hu, L., Gale, N. W., & Greenberg, M. E. (2000). EphB receptors interact with NMDA receptors and regulate excitatory synapse formation. *Cell, 103*(6), 945-956.
Dani, A., Huang, B., Bergan, J., Dulac, C., & Zhuang, X. (2010). Superresolution imaging of chemical synapses in the brain. *Neuron, 68*(5), 843-856. doi:10.1016/j.neuron.2010.11.021
Darcy, K. J., Staras, K., Collinson, L. M., & Goda, Y. (2006). An ultrastructural readout of fluorescence recovery after photobleaching using correlative light and electron microscopy. *Nature Protocols, 1*(2), 988-994. doi:10.1038/nprot.2006.146
De Camilli, P., Harris, S. M., Jr., Huttner, W. B., & Greengard, P. (1983). Synapsin I (Protein I), a nerve terminal-specific phosphoprotein. II. Its specific association with synaptic vesicles demonstrated by immunocytochemistry in agarose-embedded synaptosomes. *Journal of Cell Biology, 96*(5), 1355-1373.
Derjaguin, B. V., Muller, V. M., & Toporov, Y. P. (1994). Effect of Contact Deformations on the

Adhesion of Particles. *Progress in Surface Science, 45*(1-4), 131-143. doi:Doi 10.1016/0079-6816(94)90044-2

Diz-Munoz, A., Fletcher, D. A., & Weiner, O. D. (2013). Use the force: membrane tension as an organizer of cell shape and motility. *Trends in Cell Biology, 23*(2), 47-53. doi:10.1016/j.tcb.2012.09.006

Dong, M. D., Husale, S., & Sahin, O. (2009). Determination of protein structural flexibility by microsecond force spectroscopy. *Nature Nanotechnology, 4*(8), 514-517. doi:10.1038/Nnano.2009.156

Dong, M. D., & Sahin, O. (2011). A nanomechanical interface to rapid single-molecule interactions. *Nature Communications, 2*. doi:ARTN 247

10.1038/ncomms1246

Dufrene, Y. F., Martinez-Martin, D., Medalsy, I., Alsteens, D., & Muller, D. J. (2013). Multiparametric imaging of biological systems by force-distance curve-based AFM. *Nature Methods, 10*(9), 847-854. doi:10.1038/Nmeth.2602

Dunaevsky, A., Tashiro, A., Majewska, A., Mason, C., & Yuste, R. (1999). Developmental regulation of spine motility in the mammalian central nervous system. *Proceedings of the National Academy of Sciences of the United States of America, 96*(23), 13438-13443. doi:DOI 10.1073/pnas.96.23.13438

El-Husseini, A. E., Schnell, E., Chetkovich, D. M., Nicoll, R. A., & Bredt, D. S. (2000). PSD-95 involvement in maturation of excitatory synapses. *Science, 290*(5495), 1364-1368.

El Hady, A., & Machta, B. B. (2015). Mechanical surface waves accompany action potential propagation. *Nature Communications, 6*. doi:ARTN 6697

10.1038/ncomms7697

Ezratty, E. J., Bertaux, C., Marcantonio, E. E., & Gundersen, G. G. (2009). Clathrin mediates integrin endocytosis for focal adhesion disassembly in migrating cells. *Journal of Cell Biology, 187*(5), 733-747. doi:10.1083/jcb.200904054

Fan, Y. J., Tang, X., Vitriol, E., Chen, G., & Zheng, J. Q. (2011). Actin Capping Protein Is Required for Dendritic Spine Development and Synapse Formation. *Journal of Neuroscience, 31*(28), 10228-10233. doi:10.1523/Jneurosci.0115-11.2011

Feng, W., & Zhang, M. (2009). Organization and dynamics of PDZ-domain-related supramodules in the postsynaptic density. *Nature Reviews Neuroscience, 10*(2), 87-99. doi:10.1038/nrn2540

Fiala, J. C., Feinberg, M., Popov, V., & Harris, K. M. (1998). Synaptogenesis via dendritic filopodia in developing hippocampal area CA1. *Journal of Neuroscience, 18*(21), 8900-8911.

Finger, S. (2000). *Minds behind the brain : a history of the pioneers and their discoveries*. Oxford ; New York: Oxford University Press.

Fletcher, D. A., & Mullins, R. D. (2010). Cell mechanics and the cytoskeleton. *Nature, 463*(7280), 485-492. doi:10.1038/nature08908

Fletcher, T. L., Cameron, P., De Camilli, P., & Banker, G. (1991). The distribution of synapsin I and synaptophysin in hippocampal neurons developing in culture. *Journal of Neuroscience, 11*(6), 1617-1626.

Florin, E. L., Moy, V. T., & Gaub, H. E. (1994). Adhesion Forces between Individual Ligand-Receptor Pairs. *Science, 264*(5157), 415-417. doi:DOI 10.1126/science.8153628

Gad, M., Itoh, A., & Ikai, A. (1997). Mapping cell wall polysaccharides of living microbial cells using atomic force microscopy. *Cell Biology International, 21*(11), 697-706. doi:DOI 10.1006/cbir.1997.0214

Gaffield, M. A., & Betz, W. J. (2006). Imaging synaptic vesicle exocytosis and endocytosis with FM dyes. *Nature Protocols, 1*(6), 2916-2921. doi:10.1038/nprot.2006.476

Garcia, R., & Herruzo, E. T. (2012). The emergence of multifrequency force microscopy. *Nature*

Nanotechnology, 7(4), 217-226. doi:10.1038/Nnano.2012.38
Gardel, M. L., Shin, J. H., MacKintosh, F. C., Mahadevan, L., Matsudaira, P., & Weitz, D. A. (2004). Elastic Behavior of cross-linked and bundled actin networks. *Science, 304*(5675), 1301-1305. doi:DOI 10.1126/science.1095087
Gauthier, N. C., Masters, T. A., & Sheetz, M. P. (2012). Mechanical feedback between membrane tension and dynamics. *Trends in Cell Biology, 22*(10), 527-535. doi:10.1016/j.tcb.2012.07.005
Geiger, B., Bershadsky, A., Pankov, R., & Yamada, K. M. (2001). Transmembrane crosstalk between the extracellular matrix--cytoskeleton crosstalk. *Nat Rev Mol Cell Biol, 2*(11), 793-805. doi:10.1038/35099066
Geiger, B., Spatz, J. P., & Bershadsky, A. D. (2009). Environmental sensing through focal adhesions. *Nat Rev Mol Cell Biol, 10*(1), 21-33. doi:10.1038/nrm2593
Gerber, C., & Lang, H. P. (2006). How the doors to the nanoworld were opened. *Nature Nanotechnology, 1*(1), 3-5. doi:10.1038/nnano.2006.70
Gittes, F., Mickey, B., Nettleton, J., & Howard, J. (1993). Flexural rigidity of microtubules and actin filaments measured from thermal fluctuations in shape. *Journal of Cell Biology, 120*(4), 923-934.
Graf, E. R., Zhang, X., Jin, S. X., Linhoff, M. W., & Craig, A. M. (2004). Neurexins induce differentiation of GABA and glutamate postsynaptic specializations via neuroligins. *Cell, 119*(7), 1013-1026. doi:10.1016/j.cell.2004.11.035
Greengard, P., Valtorta, F., Czernik, A. J., & Benfenati, F. (1993). Synaptic vesicle phosphoproteins and regulation of synaptic function. *Science, 259*(5096), 780-785.
Grienberger, C., & Konnerth, A. (2012). Imaging Calcium in Neurons. *Neuron, 73*(5), 862-885. doi:10.1016/j.neuron.2012.02.011
Griffiths, G., Parton, R. G., Lucocq, J., van Deurs, B., Brown, D., Slot, J. W., & Geuze, H. J. (1993). The immunofluorescent era of membrane traffic. *Trends in Cell Biology, 3*(7), 214-219.
Grutzendler, J., Kasthuri, N., & Gan, W. B. (2002). Long-term dendritic spine stability in the adult cortex. *Nature, 420*(6917), 812-816. doi:10.1038/nature01276
Gumbiner, B. M. (2005). Regulation of cadherin-mediated adhesion in morphogenesis. *Nat Rev Mol Cell Biol, 6*(8), 622-634. doi:10.1038/nrm1699
Han, M. K. L., & de Rooij, J. (2017). Resolving the cadherin-F-actin connection. *Nature Cell Biology, 19*(1), 14-16. doi:10.1038/ncb3457
Hansma, H. G., Vesenka, J., Siegerist, C., Kelderman, G., Morrett, H., Sinsheimer, R. L., . . . Hansma, P. K. (1992). Reproducible Imaging and Dissection of Plasmid DNA under Liquid with the Atomic Force Microscope. *Science, 256*(5060), 1180-1184. doi:DOI 10.1126/science.256.5060.1180
Hebb, D. O. (1949). The organization of behavior. *Annee Psychologique, 51*, 493-494.
Heinz, W. F., & Hoh, J. H. (1999). Spatially resolved force spectroscopy of biological surfaces using the atomic force microscope. *Trends in Biotechnology, 17*(4), 143-150. doi:Doi 10.1016/S0167-7799(99)01304-9
Helenius, J., Heisenberg, C. P., Gaub, H. E., & Muller, D. J. (2008). Single-cell force spectroscopy. *Journal of Cell Science, 121*(11), 1785-1791. doi:10.1242/jcs.030999
Henderson, E., Haydon, P. G., & Sakaguchi, D. S. (1992). Actin Filament Dynamics in Living Glial-Cells Imaged by Atomic Force Microscopy. *Science, 257*(5078), 1944-1946. doi:DOI 10.1126/science.1411511
Hering, H., & Sheng, M. (2001). Dendritic spines: structure, dynamics and regulation. *Nature Reviews Neuroscience, 2*(12), 880-888. doi:10.1038/35104061
Heuser, J. E., & Reese, T. S. (1973). Evidence for recycling of synaptic vesicle membrane during transmitter release at the frog neuromuscular junction. *Journal of Cell Biology, 57*(2), 315-344.
Hill, B. C., Schubert, E. D., Nokes, M. A., & Michelson, R. P. (1977). Laser Interferometer

Measurement of Changes in Crayfish Axon Diameter Concurrent with Action Potential. *Science, 196*(4288), 426-428. doi:DOI 10.1126/science.850785

Hill, D. K. (1950). The Volume Change Resulting from Stimulation of a Giant Nerve Fibre. *Journal of Physiology-London, 111*(3-4), 304-327. doi:DOI 10.1113/jphysiol.1950.sp004481

Hinterdorfer, P., & Dufrene, Y. F. (2006). Detection and localization of single molecular recognition events using atomic force microscopy. *Nature Methods, 3*(5), 347-355. doi:10.1038/Nmeth871

Hochmuth, R. M., Mohandas, N., & Blackshear, P. L., Jr. (1973). Measurement of the elastic modulus for red cell membrane using a fluid mechanical technique. *Biophys J, 13*(8), 747-762. doi:10.1016/S0006-3495(73)86021-7

Hoh, J. H., Lal, R., John, S. A., Revel, J. P., & Arnsdorf, M. F. (1991). Atomic Force Microscopy and Dissection of Gap-Junctions. *Science, 253*(5026), 1405-1408. doi:DOI 10.1126/science.1910206

Hoh, J. H., & Schoenenberger, C. A. (1994). Surface-Morphology and Mechanical-Properties of Mdck Monolayers by Atomic-Force Microscopy. *Journal of Cell Science, 107*, 1105-1114.

Holderith, N., Lorincz, A., Katona, G., Rozsa, B., Kulik, A., Watanabe, M., & Nusser, Z. (2012). Release probability of hippocampal glutamatergic terminals scales with the size of the active zone. *Nature Neuroscience, 15*(7), 988-997. doi:10.1038/nn.3137

Holtmaat, A., & Svoboda, K. (2009). Experience-dependent structural synaptic plasticity in the mammalian brain. *Nature Reviews Neuroscience, 10*(9), 647-658. doi:10.1038/nrn2699

Holtmaat, A. J., Trachtenberg, J. T., Wilbrecht, L., Shepherd, G. M., Zhang, X., Knott, G. W., & Svoboda, K. (2005). Transient and persistent dendritic spines in the neocortex in vivo. *Neuron, 45*(2), 279-291.

Honkura, N., Matsuzaki, M., Noguchi, J., Ellis-Davies, G. C., & Kasai, H. (2008). The subspine organization of actin fibers regulates the structure and plasticity of dendritic spines. *Neuron, 57*(5), 719-729. doi:10.1016/j.neuron.2008.01.013

Hotulainen, P., & Hoogenraad, C. C. (2010). Actin in dendritic spines: connecting dynamics to function. *Journal of Cell Biology, 189*(4), 619-629. doi:DOI 10.1083/jcb.201003008

Humpel, C. (2015). Organotypic brain slice cultures: A review. *Neuroscience, 305*, 86-98. doi:10.1016/j.neuroscience.2015.07.086

Husale, S., Persson, H. H. J., & Sahin, O. (2009). DNA nanomechanics allows direct digital detection of complementary DNA and microRNA targets. *Nature, 462*(7276), 1075-U1138. doi:10.1038/nature08626

Ido, S., Kimura, K., Oyabu, N., Kobayashi, K., Tsukada, M., Matsushige, K., & Yamada, H. (2013). Beyond the Helix Pitch: Direct Visualization of Native DNA in Aqueous Solution. *Acs Nano, 7*(2), 1817-1822. doi:10.1021/nn400071n

Irie, M., Hata, Y., Takeuchi, M., Ichtchenko, K., Toyoda, A., Hirao, K., . . . Sudhof, T. C. (1997). Binding of neuroligins to PSD-95. *Science, 277*(5331), 1511-1515. doi:DOI 10.1126/science.277.5331.1511

Ivenshitz, M., & Segal, M. (2010). Neuronal Density Determines Network Connectivity and Spontaneous Activity in Cultured Hippocampus. *Journal of Neurophysiology, 104*(2), 1052-1060. doi:10.1152/jn.00914.2009

Jiang, G. Y., Giannone, G., Critchley, D. R., Fukumoto, E., & Sheetz, M. P. (2003). Two-piconewton slip bond between fibronectin and the cytoskeleton depends on talin. *Nature, 424*(6946), 334-337. doi:10.1038/nature01805

Johnson, K. L., Kendall, K., & Roberts, A. D. (1971). Surface Energy and Contact of Elastic Solids. *Proceedings of the Royal Society of London Series a-Mathematical and Physical Sciences, 324*(1558), 301-&. doi:DOI 10.1098/rspa.1971.0141

Karra, D., & Dahm, R. (2010). Transfection Techniques for Neuronal Cells. *Journal of Neuroscience,*

30(18), 6171-6177. doi:10.1523/Jneurosci.0183-10.2010

Katsamba, P., Carroll, K., Ahlsena, G., Bahna, F., Vendome, J., Posy, S., . . . Honig, B. H. (2009). Linking molecular affinity and cellular specificity in cadherin-mediated adhesion. *Proceedings of the National Academy of Sciences of the United States of America, 106*(28), 11594-11599. doi:10.1073/pnas.0905349106

Kay, L., Humphreys, L., Eickholt, B. J., & Burrone, J. (2011). Neuronal activity drives matching of pre- and postsynaptic function during synapse maturation. *Nature Neuroscience, 14*(6), 688-690. doi:10.1038/nn.2826

Kayser, M. S., McClelland, A. C., Hughes, E. G., & Dalva, M. B. (2006). Intracellular and trans-synaptic regulation of glutamatergic synaptogenesis by EphB receptors. *Journal of Neuroscience, 26*(47), 12152-12164. doi:10.1523/JNEUROSCI.3072-06.2006

Keith, D., & El-Husseini, A. (2008). Excitation Control: Balancing PSD-95 Function at the Synapse. *Front Mol Neurosci, 1*, 4. doi:10.3389/neuro.02.004.2008

Kiselyov, V. V., Berezin, V., Maar, T. E., Soroka, V., Edvardsen, K., Schousboe, A., & Bock, E. (1997). The first immunoglobulin-like neural cell adhesion molecule (NCAM) domain is involved in double-reciprocal interaction with the second immunoglobulin-like NCAM domain and in heparin binding. *Journal of Biological Chemistry, 272*(15), 10125-10134.

Kodera, N., Yamamoto, D., Ishikawa, R., & Ando, T. (2010). Video imaging of walking myosin V by high-speed atomic force microscopy. *Nature, 468*(7320), 72-76. doi:10.1038/nature09450

Korkotian, E., & Segal, M. (2001). Regulation of dendritic spine motility in cultured hippocampal neurons. *Journal of Neuroscience, 21*(16), 6115-6124.

Kornau, H. C., Schenker, L. T., Kennedy, M. B., & Seeburg, P. H. (1995). Domain Interaction between Nmda Receptor Subunits and the Postsynaptic Density Protein Psd-95. *Science, 269*(5231), 1737-1740. doi:DOI 10.1126/science.7569905

Korobova, F., & Svitkina, T. (2010). Molecular architecture of synaptic actin cytoskeleton in hippocampal neurons reveals a mechanism of dendritic spine morphogenesis. *Mol Biol Cell, 21*(1), 165-176. doi:10.1091/mbc.E09-07-0596

Kovacs, M., Toth, J., Hetenyi, C., Malnasi-Csizmadia, A., & Sellers, J. R. (2004). Mechanism of blebbistatin inhibition of myosin II. *J Biol Chem, 279*(34), 35557-35563. doi:10.1074/jbc.M405319200

Kralj, J. M., Douglass, A. D., Hochbaum, D. R., Maclaurin, D., & Cohen, A. E. (2012). Optical recording of action potentials in mammalian neurons using a microbial rhodopsin. *Nature Methods, 9*(1), 90-U130. doi:10.1038/Nmeth.1782

Krause, M., & Gautreau, A. (2014). Steering cell migration: lamellipodium dynamics and the regulation of directional persistence. *Nature Reviews Molecular Cell Biology, 15*(9), 577-590. doi:10.1038/nrm3861

Ladoux, B., Anon, E., Lambert, M., Rabodzey, A., Hersen, P., Buguin, A., . . . Mege, R. M. (2010). Strength Dependence of Cadherin-Mediated Adhesions. *Biophysical Journal, 98*(4), 534-542. doi:10.1016/j.bpj.2009.10.044

Lamoureux, P., Ruthel, G., Buxbaum, R. E., & Heidemann, S. R. (2002). Mechanical tension can specify axonal fate in hippocampal neurons. *Journal of Cell Biology, 159*(3), 499-508. doi:DOI 10.1083/jcb.200207174

Lee, S. E., Kamm, R. D., & Mofrad, M. R. (2007). Force-induced activation of talin and its possible role in focal adhesion mechanotransduction. *J Biomech, 40*(9), 2096-2106. doi:10.1016/j.jbiomech.2007.04.006

Livet, J., Weissman, T. A., Kang, H. N., Draft, R. W., Lu, J., Bennis, R. A., . . . Lichtman, J. W. (2007). Transgenic strategies for combinatorial expression of fluorescent proteins in the nervous system. *Nature, 450*(7166), 56-+. doi:10.1038/nature06293

Lulevich, V., Zink, T., Chen, H. Y., Liu, F. T., & Liu, G. Y. (2006). Cell mechanics using atomic force microscopy-based single-cell compression. *Langmuir, 22*(19), 8151-8155. doi:DOI 10.1021/la060561p

Maitre, J. L., & Heisenberg, C. P. (2013). Three functions of cadherins in cell adhesion. *Curr Biol, 23*(14), R626-633. doi:10.1016/j.cub.2013.06.019

Mak, M., Kim, T., Zaman, M. H., & Kamm, R. D. (2015). Multiscale mechanobiology: computational models for integrating molecules to multicellular systems. *Integrative Biology, 7*(10), 1093-1108. doi:10.1039/c5ib00043b

Mandriota, N. (2016). *The relationship between intracellular forces and cellular stiffness investigated by atomic force microscopy*. (Ph.D.), Columbia University Academic Commons. Retrieved from https://doi.org/10.7916/D8MC9052

Manibog, K., Li, H., Rakshit, S., & Sivasankar, S. (2014). Resolving the molecular mechanism of cadherin catch bond formation. *Nature Communications, 5*, 3941. doi:10.1038/ncomms4941

Matsuzaki, M., Ellis-Davies, G. C. R., Nemoto, T., Miyashita, Y., Iino, M., & Kasai, H. (2001). Dendritic spine geometry is critical for AMPA receptor expression in hippocampal CA1 pyramidal neurons. *Nature Neuroscience, 4*(11), 1086-1092. doi:DOI 10.1038/nn736

Matsuzaki, M., Honkura, N., Ellis-Davies, G. C., & Kasai, H. (2004). Structural basis of long-term potentiation in single dendritic spines. *Nature, 429*(6993), 761-766. doi:10.1038/nature02617

Mattila, P. K., & Lappalainen, P. (2008). Filopodia: molecular architecture and cellular functions. *Nat Rev Mol Cell Biol, 9*(6), 446-454. doi:10.1038/nrm2406

Matzke, R., Jacobson, K., & Radmacher, M. (2001). Direct, high-resolution measurement of furrow stiffening during division of adherent cells. *Nature Cell Biology, 3*(6), 607-610. doi:Doi 10.1038/35078583

Meaney, D. F., & Smith, D. H. (2011). Biomechanics of Concussion. *Clinics in Sports Medicine, 30*(1), 19-+. doi:10.1016/j.csm.2010.08.009

Meyer, D., Bonhoeffer, T., & Scheuss, V. (2014). Balance and stability of synaptic structures during synaptic plasticity. *Neuron, 82*(2), 430-443. doi:10.1016/j.neuron.2014.02.031

Missler, M., Sudhof, T. C., & Biederer, T. (2012). Synaptic Cell Adhesion. *Cold Spring Harbor Perspectives in Biology, 4*(4). doi:ARTN a005694

10.1101/cshperspect.a005694

Mizuno, D., Tardin, C., Schmidt, C. F., & MacKintosh, F. C. (2007). Nonequilibrium mechanics of active cytoskeletal networks. *Science, 315*(5810), 370-373. doi:10.1126/science.1134404

Molnar, E. (2011). Long-term potentiation in cultured hippocampal neurons. *Semin Cell Dev Biol, 22*(5), 506-513. doi:10.1016/j.semcdb.2011.07.017

Muller, D. J., & Dufrene, Y. F. (2011). Atomic force microscopy: a nanoscopic window on the cell surface. *Trends in Cell Biology, 21*(8), 461-469. doi:10.1016/j.tcb.2011.04.008

Muller, D. J., & Engel, A. (2007). Atomic force microscopy and spectroscopy of native membrane proteins. *Nature Protocols, 2*(9), 2191-2197. doi:10.1038/nprot.2007.309

Mullins, R. D., Heuser, J. A., & Pollard, T. D. (1998). The interaction of Arp2/3 complex with actin: Nucleation, high affinity pointed end capping, and formation of branching networks of filaments. *Proceedings of the National Academy of Sciences of the United States of America, 95*(11), 6181-6186. doi:DOI 10.1073/pnas.95.11.6181

Murphy, M. C., Huston, J., Jack, C. R., Glaser, K. J., Manduca, A., Felmlee, J. P., & Ehman, R. L. (2011). Decreased Brain Stiffness in Alzheimer's Disease Determined by Magnetic Resonance Elastography. *Journal of Magnetic Resonance Imaging, 34*(3), 494-498. doi:10.1002/jmri.22707

Nagerl, U. V., Willig, K. I., Hein, B., Hell, S. W., & Bonhoeffer, T. (2008). Live-cell imaging of dendritic spines by STED microscopy. *Proc Natl Acad Sci U S A, 105*(48), 18982-18987. doi:10.1073/pnas.0810028105

Nicoll, R. A., Tomita, S., & Bredt, D. S. (2006). Auxiliary subunits assist AMPA-type glutamate receptors. *Science, 311*(5765), 1253-1256. doi:10.1126/science.1123339

Niesmann, K., Breuer, D., Brockhaus, J., Born, G., Wolff, I., Reissner, C., . . . Missler, M. (2011). Dendritic spine formation and synaptic function require neurobeachin. *Nature Communications, 2*, 557. doi:10.1038/ncomms1565

Nuriya, M., & Huganir, R. L. (2006). Regulation of AMPA receptor trafficking by N-cadherin. *Journal of Neurochemistry, 97*(3), 652-661. doi:10.1111/j.1471-4159.2006.03740.x

Okabe, S., Miwa, A., & Okado, H. (2001). Spine formation and correlated assembly of presynaptic and postsynaptic molecules. *Journal of Neuroscience, 21*(16), 6105-6114.

Okamoto, K., Bosch, M., & Hayashi, Y. (2009). The roles of CaMKII and F-actin in the structural plasticity of dendritic spines: a potential molecular identity of a synaptic tag? *Physiology (Bethesda), 24*, 357-366. doi:10.1152/physiol.00029.2009

Okamoto, K., Nagai, T., Miyawaki, A., & Hayashi, Y. (2004). Rapid and persistent modulation of actin dynamics regulates postsynaptic reorganization underlying bidirectional plasticity. *Nature Neuroscience, 7*(10), 1104-1112. doi:10.1038/nn1311

Ovtscharoff, W., Jr., Segal, M., Goldin, M., Helmeke, C., Kreher, U., Greenberger, V., . . . Braun, K. (2008). Electron microscopic 3D-reconstruction of dendritic spines in cultured hippocampal neurons undergoing synaptic plasticity. *Dev Neurobiol, 68*(7), 870-876. doi:10.1002/dneu.20627

Papa, M., Bundman, M. C., Greenberger, V., & Segal, M. (1995). Morphological analysis of dendritic spine development in primary cultures of hippocampal neurons. *Journal of Neuroscience, 15*(1 Pt 1), 1-11.

Peng, J., Kim, M. J., Cheng, D., Duong, D. M., Gygi, S. P., & Sheng, M. (2004). Semiquantitative proteomic analysis of rat forebrain postsynaptic density fractions by mass spectrometry. *J Biol Chem, 279*(20), 21003-21011. doi:10.1074/jbc.M400103200

Peters, A., & Kaiserman-Abramof, I. R. (1970). The small pyramidal neuron of the rat cerebral cortex. The perikaryon, dendrites and spines. *Am J Anat, 127*(4), 321-355. doi:10.1002/aja.1001270402

Plodinec, M., Loparic, M., Monnier, C. A., Obermann, E. C., Zanetti-Dallenbach, R., Oertle, P., . . . Lim, R. Y. H. (2013). The Nanomechanical Signature of Breast Cancer. *Biophysical Journal, 104*(2), 321a-321a. doi:DOI 10.1016/j.bpj.2012.11.1779

Pozueta, J., Lefort, R., & Shelanski, M. L. (2013). Synaptic Changes in Alzheimer's Disease and Its Models. *Neuroscience, 251*, 51-65. doi:10.1016/j.neuroscience.2012.05.050

Previtera, M. L., Langhammer, C. G., & Firestein, B. L. (2010). Effects of substrate stiffness and cell density on primary hippocampal cultures. *Journal of Bioscience and Bioengineering, 110*(4), 459-470. doi:10.1016/j.jbiosc.2010.04.004

Puttock, M. J., & Thwaite, E. G. (1969). *Elastic compression of spheres and cylinders at point and line contact*. Melbourne,: Commonwealth Scientific and Industrial Research Organization.

Qian, J., & Gao, H. (2010). Soft matrices suppress cooperative behaviors among receptor-ligand bonds in cell adhesion. *PLoS One, 5*(8), e12342. doi:10.1371/journal.pone.0012342

Radmacher, M., Tillamnn, R. W., Fritz, M., & Gaub, H. E. (1992). From molecules to cells: imaging soft samples with the atomic force microscope. *Science, 257*(5078), 1900-1905.

Rakshit, S., Zhang, Y., Manibog, K., Shafraz, O., & Sivasankar, S. (2012). Ideal, catch, and slip bonds in cadherin adhesion. *Proc Natl Acad Sci U S A, 109*(46), 18815-18820. doi:10.1073/pnas.1208349109

Raman, A., Trigueros, S., Cartagena, A., Stevenson, A. P. Z., Susilo, M., Nauman, E., & Contera, S. A. (2011). Mapping nanomechanical properties of live cells using multi-harmonic atomic force microscopy. *Nature Nanotechnology, 6*(12), 809-814. doi:10.1038/Nnano.2011.186

Ranade, S. S., Woo, S. H., Dubin, A. E., Moshourab, R. A., Wetzel, C., Petrus, M., . . . Patapoutian, A.

(2014). Piezo2 is the major transducer of mechanical forces for touch sensation in mice. *Nature, 516*(7529), 121-U330. doi:10.1038/nature13980

Rao, A., Kim, E., Sheng, M., & Craig, A. M. (1998). Heterogeneity in the molecular composition of excitatory postsynaptic sites during development of hippocampal neurons in culture. *Journal of Neuroscience, 18*(4), 1217-1229.

Reddick, L. E., & Alto, N. M. (2012). Correlative Light and Electron Microscopy (CLEM) as a Tool to Visualize Microinjected Molecules and their Eukaryotic Sub-cellular Targets. *Jove-Journal of Visualized Experiments*(63). doi:UNSP e3650

10.3791/3650

Rex, C. S., Gavin, C. F., Rubio, M. D., Kramar, E. A., Chen, L. Y., Jia, Y., . . . Rumbaugh, G. (2010). Myosin IIb regulates actin dynamics during synaptic plasticity and memory formation. *Neuron, 67*(4), 603-617. doi:10.1016/j.neuron.2010.07.016

Rodriguez, T. R., & Garcia, R. (2002). Tip motion in amplitude modulation (tapping-mode) atomic-force microscopy: Comparison between continuous and point-mass models. *Applied Physics Letters, 80*(9), 1646-1648. doi:10.1063/1.1456543

Rotsch, C., & Radmacher, M. (2000). Drug-induced changes of cytoskeletal structure and mechanics in fibroblasts: An atomic force microscopy study. *Biophysical Journal, 78*(1), 520-535.

Ruska, E. (1987). The Development of the Electron-Microscope and of Electron-Microscopy (Nobel Lecture). *Angewandte Chemie-International Edition, 26*(7), 595-605. doi:DOI 10.1002/anie.198705953

Ryan, T. A., Reuter, H., Wendland, B., Schweizer, F. E., Tsien, R. W., & Smith, S. J. (1993). The Kinetics of Synaptic Vesicle Recycling Measured at Single Presynaptic Boutons. *Neuron, 11*(4), 713-724. doi:Doi 10.1016/0896-6273(93)90081-2

Ryu, J., Liu, L., Wong, T. P., Wu, D. C., Burette, A., Weinberg, R., . . . Sheng, M. (2006). A critical role for myosin IIb in dendritic spine morphology and synaptic function. *Neuron, 49*(2), 175-182. doi:10.1016/j.neuron.2005.12.017

Saglietti, L., Dequidt, C., Kamieniarz, K., Rousset, M. C., Valnegri, P., Thoumine, O., . . . Passafaro, M. (2007). Extracellular interactions between GluR2 and N-cadherin in spine regulation. *Neuron, 54*(3), 461-477. doi:10.1016/j.neuron.2007.04.012

Sahin, O., & Erina, N. (2008). High-resolution and large dynamic range nanomechanical mapping in tapping-mode atomic force microscopy. *Nanotechnology, 19*(44), 445717. doi:10.1088/0957-4484/19/44/445717

Sahin, O., Magonov, S., Su, C., Quate, C. F., & Solgaard, O. (2007). An atomic force microscope tip designed to measure time-varying nanomechanical forces. *Nature Nanotechnology, 2*(8), 507-514. doi:10.1038/nnano.2007.226

Santos, N. C., & Castanho, M. A. R. B. (2004). An overview of the biophysical applications of atomic force microscopy. *Biophysical Chemistry, 107*(2), 133-149. doi:10.1016/j.bpc.2003.09.001

Schabert, F. A., Henn, C., & Engel, A. (1995). Native Escherichia-Coli Ompf Porin Surfaces Probed by Atomic-Force Microscopy. *Science, 268*(5207), 92-94. doi:DOI 10.1126/science.7701347

Shibata, M., Uchihashi, T., Ando, T., & Yasuda, R. (2015). Long-tip high-speed atomic force microscopy for nanometer-scale imaging in live cells. *Sci Rep, 5*, 8724. doi:10.1038/srep08724

Shutova, M., Yang, C. S., Vasiliev, J. M., & Svitkina, T. (2012). Functions of Nonmuscle Myosin II in Assembly of the Cellular Contractile System. *PLoS One, 7*(7). doi:ARTN e40814

10.1371/journal.pone.0040814

Siechen, S., Yang, S., Chiba, A., & Saif, T. (2009). Mechanical tension contributes to clustering of neurotransmitter vesicles at presynaptic terminals. *Proc Natl Acad Sci U S A, 106*(31), 12611-12616. doi:10.1073/pnas.0901867106

Smith, B. A., Roy, H., De Koninck, P., Grutter, P., & De Koninck, Y. (2007). Dendritic spine

viscoelasticity and soft-glassy nature: Balancing dynamic remodeling with structural stability. *Biophysical Journal, 92*(4), 1419-1430. doi:10.1529/biophysj.106.092361

Spedden, E., & Staii, C. (2013). Neuron Biomechanics Probed by Atomic Force Microscopy. *International Journal of Molecular Sciences, 14*(8), 16124-16140. doi:10.3390/ijms140816124

Spedden, E., White, J. D., Naumova, E. N., Kaplan, D. L., & Staii, C. (2012). Elasticity maps of living neurons measured by combined fluorescence and atomic force microscopy. *Biophys J, 103*(5), 868-877. doi:10.1016/j.bpj.2012.08.005

Spence, E. F., Kanak, D. J., Carlson, B. R., & Soderling, S. H. (2016). The Arp2/3 Complex Is Essential for Distinct Stages of Spine Synapse Maturation, Including Synapse Unsilencing. *Journal of Neuroscience, 36*(37), 9696-9709. doi:10.1523/JNEUROSCI.0876-16.2016

Stark, M., Stark, R. W., Heckl, W. M., & Guckenberger, R. (2002). Inverting dynamic force microscopy: From signals to time-resolved interaction forces. *Proceedings of the National Academy of Sciences of the United States of America, 99*(13), 8473-8478. doi:10.1073/pnas.122040599

Stark, R. W. (2004). Optical lever detection in higher eigenmode dynamic atomic force microscopy. *Review of Scientific Instruments, 75*(11), 5053-5055. doi:10.1063/1.1808058

Stolz, M., Gottardi, R., Raiteri, R., Miot, S., Martin, I., Imer, R., . . . Aebi, U. (2009). Early detection of aging cartilage and osteoarthritis in mice and patient samples using atomic force microscopy. *Nature Nanotechnology, 4*(3), 186-192. doi:10.1038/Nnano.2008.410

Storm, C., Pastore, J. J., MacKintosh, F. C., Lubensky, T. C., & Janmey, P. A. (2005). Nonlinear elasticity in biological gels. *Nature, 435*(7039), 191-194. doi:10.1038/nature03521

Stossel, T. P., Condeelis, J., Cooley, L., Hartwig, J. H., Noegel, A., Schleicher, M., & Shapiro, S. S. (2001). Filamins as integrators of cell mechanics and signalling. *Nature Reviews Molecular Cell Biology, 2*(2), 138-145. doi:Doi 10.1038/35052082

Straub, C., & Sabatini, B. L. (2014). How to Grow a Synapse. *Neuron, 82*(2), 256-257. doi:10.1016/j.neuron.2014.03.033

Stricker, J., Beckham, Y., Davidson, M. W., & Gardel, M. L. (2013). Myosin II-Mediated Focal Adhesion Maturation Is Tension Insensitive. *PLoS One, 8*(7). doi:ARTN e70652
10.1371/journal.pone.0070652

Stroka, K. M., & Aranda-Espinoza, H. (2011). Effects of Morphology vs. Cell-Cell Interactions on Endothelial Cell Stiffness. *Cellular and Molecular Bioengineering, 4*(1), 9-27. doi:10.1007/s12195-010-0142-y

Tanaka, H., Shan, W., Phillips, G. R., Arndt, K., Bozdagi, O., Shapiro, L., . . . Colman, D. R. (2000). Molecular modification of N-cadherin in response to synaptic activity. *Neuron, 25*(1), 93-107.

Tasaki, I., & Byrne, P. M. (1982). Tetanic Contraction of the Crab Nerve Evoked by Repetitive Stimulation. *Biochemical and Biophysical Research Communications, 106*(4), 1435-1440. doi:Doi 10.1016/0006-291x(82)91274-8

Togashi, H., Abe, K., Mizoguchi, A., Takaoka, K., Chisaka, O., & Takeichi, M. (2002). Cadherin regulates dendritic spine morphogenesis. *Neuron, 35*(1), 77-89. doi:Doi 10.1016/S0896-6273(02)00748-1

Tonnesen, J., Katona, G., Rozsa, B., & Nagerl, U. V. (2014). Spine neck plasticity regulates compartmentalization of synapses. *Nature Neuroscience, 17*(5), 678-685. doi:10.1038/nn.3682

Tsay, D., & Yuste, R. (2004). On the electrical function of dendritic spines. *Trends in Neurosciences, 27*(2), 77-83. doi:10.1016/j.tins.2003.11.008

Tseng, Y., Kole, T. P., Lee, J. S. H., Fedorov, E., Alino, S. C., Schafer, B. W., & Wirtz, D. (2005). How actin crosslinking and bundling proteins cooperate to generate an enhanced cell mechanical response. *Biochemical and Biophysical Research Communications, 334*(1), 183-192. doi:10.1016/j.bbrc.2005.05.205

Tyler, W. J. (2012). OPINION The mechanobiology of brain function. *Nature Reviews Neuroscience,*

13(12), 867-878. doi:10.1038/nrn3383

Umeda, T., Ebihara, T., & Okabe, S. (2005). Simultaneous observation of stably associated presynaptic varicosities and postsynaptic spines: morphological alterations of CA3-CA1 synapses in hippocampal slice cultures. *Molecular and Cellular Neuroscience, 28*(2), 264-274. doi:10.1016/j.mcn.2004.09.010

van Spronsen, M., & Hoogenraad, C. C. (2010). Synapse Pathology in Psychiatric and Neurologic Disease. *Current Neurology and Neuroscience Reports, 10*(3), 207-214. doi:10.1007/s11910-010-0104-8

Vogel, V., & Sheetz, M. (2006). Local force and geometry sensing regulate cell functions. *Nature Reviews Molecular Cell Biology, 7*(4), 265-275. doi:10.1038/nrm1890

Volkmann, N., Amann, K. J., Stoilova-McPhie, S., Egile, C., Winter, D. C., Hazelwood, L., . . . Hanein, D. (2001). Structure of Arp2/3 complex in its activated state and in actin filament branch junctions. *Science, 293*(5539), 2456-2459. doi:DOI 10.1126/science.1063025

Wegner, A. M., Nebhan, C. A., Hu, L., Majumdar, D., Meier, K. M., Weaver, A. M., & Webb, D. J. (2008). N-WASP and the Arp2/3 complex are critical regulators of actin in the development of dendritic spines and synapses. *Journal of Biological Chemistry, 283*(23), 15912-15920. doi:10.1074/jbc.M801555200

Wilhelm, B. G., Mandad, S., Truckenbrodt, S., Krohnert, K., Schafer, C., Rammner, B., . . . Rizzoli, S. O. (2014). Composition of isolated synaptic boutons reveals the amounts of vesicle trafficking proteins. *Science, 344*(6187), 1023-1028. doi:10.1126/science.1252884

Xiong, Y., Lee, A. C., Suter, D. M., & Lee, G. U. (2009). Topography and nanomechanics of live neuronal growth cones analyzed by atomic force microscopy. *Biophys J, 96*(12), 5060-5072. doi:10.1016/j.bpj.2009.03.032

Xu, C., Liu, H., Qi, L., Hao, G., Shen, Z., Wang, Y., Babcock, H., Lau, P., Zhuang, X, Bi, G. (2017). *Structure and plasticity of silent synapses in developing hippocampal neurons visualized quantitatively by super-resolution imaging*. Paper presented at the Society for Neuroscience, Washington, DC. Poster retrieved from http://www.abstractsonline.com/pp8/#!/4376/presentation/15082

Xu, K., Zhong, G., & Zhuang, X. (2013). Actin, spectrin, and associated proteins form a periodic cytoskeletal structure in axons. *Science, 339*(6118), 452-456. doi:10.1126/science.1232251

Yang, N., Wong, K. K. H., de Bruyn, J. R., & Hutter, J. L. (2009). Frequency-dependent viscoelasticity measurement by atomic force microscopy. *Measurement Science and Technology, 20*(2). doi:Artn 025703

10.1088/0957-0233/20/2/025703

Yasuda, R., Harvey, C. D., Zhong, H. N., Sobczyk, A., van Aelst, L., & Svoboda, K. (2006). Supersensitive Ras activation in dendrites and spines revealed by two-photon fluorescence lifetime imaging. *Nature Neuroscience, 9*(2), 283-291. doi:10.1038/nn1635

Yonemura, S., Wada, Y., Watanabe, T., Nagafuchi, A., & Shibata, M. (2010). alpha-Catenin as a tension transducer that induces adherens junction development. *Nature Cell Biology, 12*(6), 533-U535. doi:10.1038/ncb2055

Yuste, R. (2010). *Dendritic spines*. Cambridge, Mass: MIT Press.

Yuste, R., & Bonhoeffer, T. (2004). Genesis of dendritic spines: insights from ultrastructural and imaging studies. *Nature Reviews Neuroscience, 5*(1), 24-34. doi:10.1038/nrn1300

Zasadzinski, J. A., Viswanathan, R., Madsen, L., Garnaes, J., & Schwartz, D. K. (1994). Langmuir-Blodgett-Films. *Science, 263*(5154), 1726-1733. doi:DOI 10.1126/science.8134836

Zhang, H., & Liu, K. K. (2008). Optical tweezers for single cells. *Journal of the Royal Society Interface, 5*(24), 671-690. doi:10.1098/rsif.2008.0052

Zhang, L., Rzigalinski, B. A., Ellis, E. F., & Satin, L. S. (1996). Reduction of voltage-dependent Mg2+ blockade of NMDA current in mechanically injured neurons. *Science, 274*(5294), 1921-1923.

doi:DOI 10.1126/science.274.5294.1921
Zhang, Q. Y., Zhang, Y. Y., Xie, J., Li, C. X., Chen, W. Y., Liu, B. L., . . . Zhao, H. C. (2014). Stiff substrates enhance cultured neuronal network activity. *Scientific Reports, 4*. doi:ARTN 6215
10.1038/srep06215
Zhang, W. D., & Benson, D. L. (2001). Stages of synapse development defined by dependence on F-actin. *Journal of Neuroscience, 21*(14), 5169-5181.
Zhou, Q., Homma, K. J., & Poo, M. M. (2004). Shrinkage of dendritic spines associated with long-term depression of hippocampal synapses. *Neuron, 44*(5), 749-757. doi:10.1016/j.neuron.2004.11.011
Ziv, N. E., & Smith, S. J. (1996). Evidence for a role of dendritic filopodia in synaptogenesis and spine formation. *Neuron, 17*(1), 91-102.